

Rowan University

Rowan Digital Works

---

Theses and Dissertations

---

6-28-2024

# MANUFACTURING OF ALIGNED ELECTROSPUN NANOFIBER YARNS FOR THEIR ENHANCED MECHANICAL AND PIEZOELECTRIC PROPERTIES

Adaugo Mary-Frances Euka  
*Rowan University*

Follow this and additional works at: <https://rdw.rowan.edu/etd>



Part of the [Chemical Engineering Commons](#), and the [Nanotechnology Commons](#)

---

## Recommended Citation

Euka, Adaugo Mary-Frances, "MANUFACTURING OF ALIGNED ELECTROSPUN NANOFIBER YARNS FOR THEIR ENHANCED MECHANICAL AND PIEZOELECTRIC PROPERTIES" (2024). *Theses and Dissertations*. 3259.

<https://rdw.rowan.edu/etd/3259>

This Thesis is brought to you for free and open access by Rowan Digital Works. It has been accepted for inclusion in Theses and Dissertations by an authorized administrator of Rowan Digital Works. For more information, please contact [graduateresearch@rowan.edu](mailto:graduateresearch@rowan.edu).

**MANUFACTURING OF ALIGNED ELECTROSPUN NANOFIBER YARNS FOR  
THEIR ENHANCED MECHANICAL AND PIEZOELECTRIC PROPERTIES**

by

Adaugo M. Euka

A Thesis

Submitted to the  
Department of Chemical Engineering  
Henry M. Rowan College of Engineering  
In partial fulfillment of the requirements  
For the degree of  
Master of Science in Chemical Engineering  
at  
Rowan University  
May 1, 2024

Thesis Chair: Vince Z. Beachley, Ph.D., Associate Professor, Department of Biomedical  
Engineering

Committee Members:

James Newell, Ph.D., Professor, Department of Chemical Engineering  
Wei Xue, Ph.D., Associate Professor, Department of Mechanical Engineering

© 2024 Adaugo Mary-Frances Euka

## **Dedication**

This thesis is dedicated to my mom, Nkechi, dad, John, and siblings Amanda, Chinonyelum, Mary-Angel, and Chizitelum. Thank you for your moral, emotional, and spiritual support throughout this academic journey.

## **Acknowledgments**

I am deeply grateful to my research supervisor, Dr. Vince Beachley, for equipping me with the essential knowledge to navigate this research journey from inception to completion. His unwavering dedication, passion, foresight, and support have been a constant source of inspiration and motivation. Working under his mentorship has been a privilege, and I appreciate the numerous opportunities he provided to foster my professional growth and work ethic.

I sincerely appreciate my family's unwavering encouragement, prayers, and support. They are a constant source of strength and motivation, helping me overcome challenges to reach this milestone. I could not have achieved this without their steadfast care and comfort whenever I needed it.

I thank my committee members, Prof. James Newell and Dr. Wei Xue, for their invaluable guidance and assistance throughout my research. Their time and contributions have played a significant role in my success. Special appreciation goes to Prof. Kauser Jahan for offering me my graduate tutoring experience during Rowan University's Opportunity for Postsecondary Excellence and Success (R.O.P.E.S.) program. Her continuous encouragement has fueled my passion for research. Thanks to Dr. Kirti Yenkie's mentorship via the Woman Alliance Network Program at Rowan University.

Lastly, I appreciate Mohamad Keblawi, Emmet Sedar, Dominique Hassinger, and other lab members for their direct and indirect support during this research. To the wonderful friends and course mates I have met at Rowan University, your presence has enriched my experience, and I am genuinely thankful for our connection.

## **Abstract**

Adaugo Mary-Frances Euka

MANUFACTURING OF POST-DRAWN ELECTROSPUN NANOFIBER YARNS FOR  
THEIR ENHANCED MECHANICAL AND PIEZOELECTRIC PROPERTIES

2023 – 2024

Vince Z. Beachley, Ph.D.

Master of Science in Chemical Engineering

Electrospinning is a widely used technique for producing nanofibers with diverse applications. This method uses polymer solutions and strong electric fields to generate nano-sized fibers with unique properties. This study presents a novel manufacturing approach that enables the production of electrospun poly(vinylidene fluoride-co-hexafluoropropylene) (PVDF-HFP) nanofiber yarns using an automated parallel track system and an adjustable roll-to-roll collector. This research examines the impact of an automated post-drawing system on the polymer chain orientation, crystallinity, tensile strength, morphology, and piezoelectric properties of PVDF-HFP nanofiber yarn. The results reveal that the post-drawing process significantly improves molecular alignment, increases tensile strength, and enhances the piezoelectric outputs of the nanofiber yarn. The potential applications of these piezoelectric nanofiber yarns extend to the realm of smart textiles, where they can be integrated into various wearable devices and intelligent fabrics. It highlights a significant advancement in the field and emphasizes the importance of post-drawing processing in improving the tensile and piezoelectric properties of electrospun PVDF-HFP nanofiber yarn. Furthermore, it demonstrates the potential for manufacturing on a commercial scale, a feat not achieved by previous research efforts, increasing economic market opportunities in the smart textile industry.

## Table of Contents

Abstract.....	v
List of Figures.....	ix
List of Tables.....	xiv
Chapter 1: Introduction.....	1
1.1 Overview.....	1
1.2 Scope of Study.....	2
1.3 Aim and Objectives of Study.....	3
1.4 Motivation of Study.....	3
1.5 Thesis Summary.....	6
Chapter 2: Background.....	8
2.1 Nanofibers.....	8
2.2 Electrospinning Overview.....	9
2.3 Self-bundling Electrospinning for Nanoyarn Formation.....	12
2.4 Ferroelectricity.....	14
2.4.1 Mechanism of Piezoelectricity.....	15
2.4.2 Piezoelectric Effect.....	17
2.5 Triboelectricity.....	21
2.6 Piezoelectric Materials.....	24
2.6.1 Natural/Bio Piezoelectric.....	25
2.6.2 Inorganic Piezoelectric Ceramics.....	26
2.6.3 Piezoelectric Polymers.....	28
2.6.4 Composite Piezoelectric.....	36

## Table of Contents (Continued)

2.7 Energy Harvesting and Applications .....	37
Chapter 3: Characterization and Experimental Methods .....	42
3.1 Introduction.....	42
3.2 Materials and Solvents.....	43
3.2.1 Poly(vinylidene fluoride-co-hexafluoropropylene) (PVDF-HFP) Polymer .....	43
3.2.2 N, N-dimethylformamide (DMF) .....	44
3.2.3 Acetone .....	45
3.2.4 Electric Paint.....	45
3.3 Sample Preparation Method.....	46
3.3.1 Electrospinning of PVDF-HFP Nanofibers .....	47
3.3.2 Principle of the Post-Drawing Process .....	48
3.3.3 Automated Parallel Track System.....	49
3.3.4 Roll to Roll Collector.....	51
3.3.5 Yarn Spinning Process .....	52
3.4 Mechanical Testing .....	54
3.5 Scanning Electron Microscopy (SEM).....	57
3.6 Brightfield Microscope .....	58
3.7 Fourier Transform Infrared Spectroscopy (FTIR) .....	59
3.8 Mechanical-Electrical Experimental System Setup.....	61
3.8.1 Stretch Deformation.....	63
3.8.2 Flick Deformation .....	64
Chapter 4: Result and Discussion .....	67

## Table of Contents (Continued)

4.1 Introduction.....	67
4.2 Tensile Analysis .....	67
4.3 Morphology Analysis.....	74
4.4 Fourier Transform Infrared Spectroscopy (FTIR) Analysis .....	77
4.5 Mechanical-Electrical Testing Analysis.....	84
4.5.1 Flick Deformation Analysis .....	84
4.5.2 Stretch Deformation Analysis .....	86
4.6 Statistical Analysis .....	90
Chapter 5: Conclusion and Future Work.....	91
5.1 Conclusions.....	91
5.2 Future Work .....	92
References .....	94
Appendix: List of Abbreviations.....	106

## List of Figures

Figure	Page
Figure 1. Global Smart Textile Market .....	5
Figure 2. Aligned mesh SEM image of PVDF-HFP nanofibers .....	9
Figure 3. Schematics Illustration of Electrospinning Process .....	11
Figure 4. Self-bundling electrospinning system .....	13
Figure 5. Relationship between Ferroelectric, Pyroelectric, Piezoelectric, and Dielectric materials .....	15
Figure 6. The illustration shows a two-dimensional grid model of a piezoelectric substance. A unit cell is outlined by dotted lines. The left portion displays the material in its relaxed state, where the center points of positive and negative charges align, indicated by a black dot. The right section presents the material under compression. This compression causes the material to expand horizontally, leading to a separation of positive and negative charges, marked by asterisks (*). This charge separation results in the formation of an electric dipole. Blue and yellow dots represent the center points of the positive and negative charges, respectively, in this compressed state .....	17
Figure 7. The illustration depicts two key aspects of piezoelectricity: the direct effect, where mechanical stress produces an electric charge, and the converse effect, where an applied electric field results in physical deformation or strain. This schematic visualization demonstrates the bidirectional nature of the piezoelectric phenomenon .....	18
Figure 8. Notation of crystal axes with the polarization of light passing through the crystal.....	20
Figure 9. Overview of the major classes of Piezoelectric materials with some representative examples within each category. ....	24
Figure 10. Centrosymmetric and Non-centrosymmetric Crystal Structure .....	25
Figure 11. A chain conformation for PVDF's $\alpha$ , $\beta$ , and $\gamma$ crystalline phases .....	29
Figure 12. The structural formula of polyvinylidene fluoride PVDF .....	31
Figure 13. The structural formula for poly(vinylidene fluoride-co-hexafluoropropylene) PVDF-HFP .....	33
Figure 14. The structural Formula for Poly(vinylidene fluoride-co-trifluoro ethylene) (PVDF-TrFE) .....	35

## List of Figures (Continued)

Figure	Page
Figure 15. Various Applications of piezoelectric electrospun PVDF film .....	40
Figure 16. Visualizing the solubility of PVDF-HFP in DMF and acetone mixtures using teas diagrams.....	43
Figure 17. Schematics Flowchart Process of (A) DMF and Acetone solvents are poured into a beaker containing a yellow magnetic stirrer on a hot plate at 65°C. (B) measured PVDF-HFP pellets are poured into the solvent mixture, stirring at 250 rpm for 24 hrs. (C) Homogenous PVDF-HFP solution.....	47
Figure 18. illustrates the automated-track system for facilitating the continuous collection of polyvinylidene fluoride-co-hexafluoropropylene (PVDF-HFP) nanofibers. The top gap represents the undrawn nanofibers, while the bottom gap shows the post-drawn nanofibers. As the nanofibers are lengthened during the drawing process, their diameter decreases due to the alignment and extension of the polymer chains. This process is expected to result in a higher prevalence of organized polymer chains, leading to stronger and more aligned nanofibers.....	48
Figure 19. (A) Schematics of the variable draw ratio electrospinning system modified to collect controls of each sample (B) Electrospinning system setup with the roll-to-roll collector (C) Parchment paper containing a sample of electrospun PVDF-HFP nanofibers.....	50
Figure 20. (A) Schematics of the variable draw ratio electrospinning system modified to collect controls of each sample (B) Electrospinning system setup (C) Tray Collector containing electrospun PVDF-HFP nanofibers (D) 10mm by 10mm plastic window frame containing an electrospun PVDF-HFP sample .....	51
Figure 21. Modifiable roll-to-roll collector allowing collection of electrospun nanofibers as they travel down the automated tracks .....	52
Figure 22. (A) Schematics diagram of the yarn spinning method. (B) Pictorial representation of the yarn-spinning method .....	54
Figure 23. A typical stress-strain curve .....	56
Figure 24. Tensile test of an electrospun PVDF-HFP nanofiber yarn using the universal testing System .....	57

## List of Figures (Continued)

Figure	Page
Figure 25. (A) 10 cm measured PVDF-HFP yarn sample (B) A pair of jumper wires ends attached to a yarn sample (C) Complete view of a pair of jumper wires attached to a yarn sample at two points with a distance of 1 cm (D) Electric Paint (Bare Conductive) (E) Prepared PVDF-HFP yarn sample for electrical testing .....	61
Figure 26. National Instrument (NI) USB-6000 multifunction data acquisition (DAQ) device .....	62
Figure 27. Stretch deformation test on an electrospun PVDF-HFP nano yarn sample using a programmable motion controller .....	64
Figure 28. Flick deformation test on an electrospun PVDF-HFP nanoyarn sample using a rotating wheel powered by a 12 V DC motor .....	65
Figure 29. Specific strength of low density (LD) nanoyarn vs. component fiber draw ratio ( $n = 5$ ), ANOVA p-value $< 0.01$ , all group-to-group comparisons student t-test give a p-value $< 0.01$ for LDR1 vs LDR3 only .....	70
Figure 30. Specific strength of nanoyarns vs low (LD), medium (MD), and high (HD) density yarns, ANOVA p-value $> 0.01$ , All were comprised of component fibers drawn to a draw ratio of three (DR3) ( $n = 5$ ), and all group-to-group comparisons with student t-test give a p-value $> 0.01$ .....	70
Figure 31. Specific strength of nanofibers vs draw ratio ( $n=5$ ), ANOVA p-value = 0.01, group-to-group comparisons with student t-test have a p-value $< 0.01$ , except for groups LDR2 vs LDR3 .....	71
Figure 32. Mechanical behavior of component nanofibers (A) presents stress-strain curves from one nanofiber sample for LDR1, LDR2, and LDR3. The curves are truncated after the ultimate tensile strength peak for better presentation. (B) Notably, there is a clear upward trend in the nanofiber yield stress from the LDR1 to LDR3, indicating a significant increase in strength, ANOVA p-value $< 0.01$ , all group-to-group comparisons with student t-tests give a p-value $< 0.01$ , except for groups DR2 vs DR3. (C) The Young's Moduli shows a continuous increase from LDR1 to LDR3, ANOVA p-value $> 0.01$ , all group-to-group comparisons with student t-tests give a p-value $> 0.01$ . (D) Ultimate tensile strength also shows a continuous increase from LDR1 to LDR3, ANOVA p-value $> 0.01$ , and all group-to-group comparisons with student t-tests give a p-value $> 0.01$ .....	72

## List of Figures (Continued)

Figure	Page
<p>Figure 33. Mechanical behavior of nanoyarns (A) presents stress-strain curves from one nanoyarn sample for LDR1, LDR2, and LDR3. The curves are truncated after the ultimate tensile strength peak for better presentation. (B) There is a noticeable upward trend in the yield stress of the nanoyarns from LDR1 to LDR3, indicating an increase in strength, ANOVA p-value &lt; 0.01, all group-to-group comparisons with student t-tests give a p-value &lt; 0.01, except for groups LDR2 vs LDR3. (C) The Young's Modulus, a measure of stiffness, exhibits a continuous increase from LDR1 to LDR3, ANOVA p-value &lt; 0.01, all group-to-group comparisons with student t-test give a p-value &lt; 0.01, except for groups LDR1 vs LDR3. (D) Similarly, the ultimate tensile strength, which represents the maximum stress the material can withstand, also shows an increase from LDR1 to LDR3 (n = 5) for figures (B-D), ANOVA p-value &lt; 0.01, all group-to-group comparisons with student t-test have a p-value &lt; 0.01 for LDR1 vs LDR3 only .....</p>	73
<p>Figure 34. (A-C) shows representative SEM images of PVDF-HFP nanofiber with low linear density (fixed) and component fiber draw ratio varied from DR1-DR3. All scale bars = 5 <math>\mu\text{m}</math>.....</p>	75
<p>Figure 35. (A-E) shows representative SEM images of PVDF-HFP nanoyarns with low linear density (fixed), medium linear density, high linear density, and component fiber draw ratio varied from DR1-DR3 for LDR1, LDR2, LDR3, MDR3, and HDR3, respectively. Scale bars are 400 and 500 <math>\mu\text{m}</math> .....</p>	76
<p>Figure 36. Non-polarized FTIR representative spectra for the film and nanofiber at DR1, DR2, and DR3.....</p>	82
<p>Figure 37. Non-polarized FTIR representative spectra for film and nano yarn at DR1, DR2, and DR3 .....</p>	83
<p>Figure 38. Polarized 0° and 90° FTIR representative spectra for DR1, DR2, and DR3 nanofiber .....</p>	83
<p>Figure 39. Polarized 0° and 90° FTIR representative spectra for DR1, DR2, and DR3 nanoyarn.....</p>	84
<p>Figure 40. Flick deformation test (A-C) Peak-to-peak voltage outputs for LDR1, LDR2, and LDR3, respectively. (D) Voltage per draw ratio (V), ANOVA p-value &lt; 0.01, all group-to-group comparisons with student t-test give a p-value &lt; 0.01 for group LDR1 vs LDR3 only .....</p>	85
<p>Figure 41. Flick deformation test (A-C) Peak-to-peak voltage outputs for LDR3, MDR3, and HDR3, respectively. (D) Voltage per density (V), ANOVA p-value &gt; 0.01, and all group-to-group comparisons with student t-tests give a p-value &gt; 0.01 .....</p>	86

## List of Figures (Continued)

Figure	Page
Figure 42. Stretch deformation test (A-C) Peak-to-peak voltage outputs for LDR1, LDR2, and LDR3, respectively. (D) Voltage per draw ratio (V), ANOVA p-value < 0.01, and all group-to-group comparisons with student t-test give a p-value < 0.01 .....	87
Figure 43. Stretch deformation test (A-C) peak-to-peak voltage outputs for LDR3, MDR3, and HDR3, respectively. (D) Voltage per density (V), ANOVA p-value < 0.01, and all group-to-group comparisons with student t-test give a p-value < 0.01 except for groups MDR3 vs HDR3 .....	88

## List of Tables

Table	Page
Table 1. Comparing Significant Mechanical and Piezoelectric Properties of PVDF, PVDF-HFP, and PVDF-TrFE .....	35
Table 2. Comparing Significant Mechanical and Piezoelectric Parameters for PVDF, PZT, and BaTiO <sub>3</sub> .....	37
Table 3. Average Nanofiber Diameters and Standard Deviation for Each Group (n = 5).....	75
Table 4. Average Nanoyarn Diameters and Standard Deviation for Each Group (n = 5).....	75
Table 5. Average $\beta$ -phase Content for Nanofiber at Different Draw Ratios .....	80
Table 6. Average $\beta$ -phase Content for Nanofiber Yarn or Nano Yarns at Different Draw Ratios .....	80
Table 7. The Dichroic Ratio for Each Group Nanofiber (n = 1) for the Wavenumbers 1400 cm <sup>-1</sup> , 1278 cm <sup>-1</sup> , 1180 cm <sup>-1</sup> , 1070 cm <sup>-1</sup> , 881 cm <sup>-1</sup> , 840 cm <sup>-1</sup> and 474 cm <sup>-1</sup> .....	81
Table 8. The Dichroic Ratio for Each Group Nano Yarn (n = 1) for the Wavenumbers 1400 cm <sup>-1</sup> , 1278 cm <sup>-1</sup> , 1180 cm <sup>-1</sup> , 1070 cm <sup>-1</sup> , 881 cm <sup>-1</sup> , and 840 cm <sup>-1</sup> .....	82

# Chapter 1

## Introduction

### 1.1 Overview

Polyvinylidene fluoride (PVDF) is a well-known synthetic polymer with exceptional piezoelectric properties, first discovered in 1969. PVDF has been combined with other materials to enhance its piezoelectric performance and create composite materials (1). Electrospinning is one of the most extensively researched processes for producing PVDF nanofibers. This is because it does not necessitate a separate poling phase, typically required to induce piezoelectric properties in PVDF (2). Electrospinning is a simple, rapid, and efficient method for generating nanofibers. Precise regulation of operating parameters is essential for the electrospinning process to generate the desired fiber morphologies and diameters. The resulting nanofibers possess distinctive features, including an extremely small diameter, a high surface area to volume ratio, and the capacity to form highly porous mats or fleeces (3).

Electrospinning, as a versatile technology, provides a new avenue for developing smart fibers. Over the past few decades, it has garnered significant attention due to its simple method of producing micro- and even sub-nano-scale fibers with exceptional mechanical properties, particularly flexibility. These fibers exhibit a large specific surface area, high aspect ratio, surface functionality, low density, the ability to form fibers in one dimension (1D) to three dimensions (3D), and high porosity. Electrospun fibers have found widespread applications owing to these advantageous characteristics (4).

PVDF must be in the electroactive phase to exhibit promising piezoelectric properties. PVDF has five known crystalline phases:  $\alpha$ ,  $\beta$ ,  $\gamma$ ,  $\delta$ , and  $\epsilon$ . These phases determine the

electroactive properties, with the  $\beta$ -phase being the most crucial due to its excellent piezo-, pyro-, and ferroelectric characteristics. In the  $\beta$ -phase, all dipole moments are aligned in the same direction, resulting in a non-zero dipole moment and the highest piezoelectric responses (5). Due to its exceptional properties, Poly (vinylidene fluoride) (PVDF) has become the preferred polymer for many scientific researchers. These include its piezo-, pyro-, and ferroelectric characteristics, flexibility, thermal stability, high mechanical strength, chemical resistance, and the ability to be fabricated into various structures. As a result, PVDF has been increasingly utilized in diverse fields, such as energy harvesting and sensing applications (6)

## **1.2 Scope of Study**

This study focuses on manufacturing poly(vinylidene fluoride-co-hexafluoropropylene) PVDF-HFP nanofiber yarn using an electrospinning technique combined with an automated track system, an adjustable roll-to-roll collector, and a novel twist and roll (spinning) device. The goal is to enhance the nanofiber yarn's mechanical and piezoelectric properties by varying process parameters, such as fiber densities and draw ratios. Two forms of mechanical deformation, flick, and stretch tests, are used in the electrical testing of the nano yarns. Electrospinning is an innovative and efficient fabrication technique that produces fibrous polymer mats composed of fibers with diameters ranging from several microns to less than 100 nanometers. This process relies on the intricate interplay of surface properties, rheological characteristics, and electrical charge. Electrospinning has been employed to generate nanofibers from various materials, with the most commonly used being organic polymers in either solution or melt form (7–9).

The results from this study are further characterized by analysis methods such as scanning electron microscopy, Fourier transform infrared spectroscopy, and electrical tests from different modes of mechanical deformation. By developing high-performance PVDF-HFP nanofiber yarns with enhanced mechanical and piezoelectric properties, this work aims to advance energy harvesting technologies, particularly in the smart textile industry. The fabricated nano yarns can be integrated into various devices, such as self-powered sensors, wearable electronics, and smart textiles, to capture and convert ambient mechanical energy into electrical energy.

### **1.3 Aim and Objectives of Study**

The aim and objectives of this study are:

1. To manufacture electrospun PVDF-HFP nanofiber yarn using a novel twist and roll technique in conjunction with an automated parallel track system and an adjustable roll-to-roll collector
2. To enhance the mechanical and electrical properties of the nanofiber yarn by varying different process parameters
3. To characterize the manufactured nanofiber yarns using techniques such as scanning electron microscopy, Fourier transform infrared spectroscopy
4. To obtain electrical voltage outputs from applied mechanical input forces.

### **1.4 Motivation of Study**

Piezoelectric polymers like PVDF and its copolymers are well-suited for wearable sensors due to their flexibility, softness, stability, biocompatibility, piezoelectric properties, ease of

processing, and cost-effectiveness (10). The results from this study will characterize the manufactured material, evaluating not just its mechanical properties but also its piezoelectric capabilities. This investigation seeks to provide insights into the potential of this electrospun PVDF-HFP nanofiber yarn for use in smart textiles.

Smart textiles are advanced materials that can detect and react to their surroundings reliably and beneficially. These textiles may include components such as sensors, actuators, power sources, communication systems, data processing units, and interconnecting elements to create a complete intelligent system. However, a smart textile does not always need all these functional elements to be considered intelligent (11). One of the most important considerations for fibers is choosing materials that give them some intelligence. Stimuli-responsive polymers engineered into nanoscale or nano-fibrous fibers via electrospinning can result in a larger specific surface area and higher porosity, enhancing sensitivity. The higher porosity and larger specific surface area lead to shorter diffusion distances and more interactive sites, respectively. Smart properties can also come from special polymers with effects like piezoelectric and triboelectric, making them an excellent choice for flexible electronics fabrication (4).

The smart textile industry is poised for substantial growth in the next few years, with multiple market research reports forecasting strong economic prospects as shown in Figure 1. The global smart textiles market is anticipated to expand from \$2.9 billion in 2022 to \$14.8 billion by 2032 at an average annual growth rate of approximately 20%. Similarly, the e-textiles and smart clothing market is projected to grow at an average annual rate of 32.35% between 2022 and 2028, rising from \$1.73 billion in 2021 to \$15.02 billion by 2028. These high growth rates suggest the smart textile industry will encounter significant

economic opportunities in the coming years. The increasing incorporation of technology into textiles, rising demand for fitness and health tracking wearables, and expanding applications across various end-use industries such as sports, fitness, military, and healthcare drive this market expansion (12). Various factors influence the demand for smart textiles, from the rising demand for wearable technology to integration with the Internet of Things (IoT).

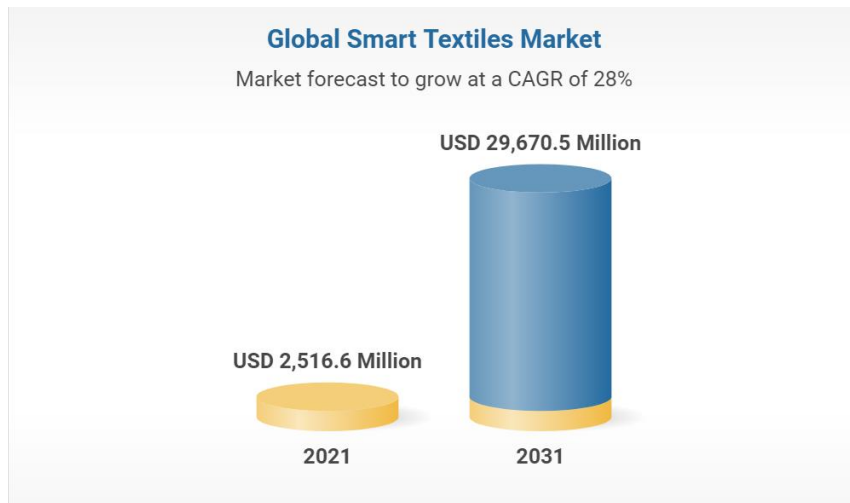


*Figure 1.* Global Smart Textile Market (12)

The unique properties of electrospun PVDF-HFP nanofibers make them promising materials for sustainable energy solutions. Their piezoelectric capabilities allow the generation of electrical charges from mechanical deformation, potentially powering various devices. It can contribute to achieving the 2030 Agenda's Sustainable Development Goal 7, which aims to ensure universal access to affordable, reliable, and modern energy. These PVDF-HFP nanofibers promise to advance affordable, reliable, and modern energy sources (13). Previous studies have shown that PVDF-HFP has better flexibility than

PVDF, but no method has been developed to produce continuous post-drawn electrospun PVDF nanofiber yarns commercially. This research technique can potentially revolutionize the manufacturing of continuous post-drawn electrospun PVDF nanofiber yarns on a commercial scale. The results of this study suggest that the technique could lead to significant advancements in producing these materials.

### **1.5 Thesis Summary**

The pursuit of high-performance piezoelectric materials has gained significant momentum, driven by their versatile applications in energy harvesting, sensing, and actuation. Nanofiber yarns, with their unique structure and high surface area, present an intriguing avenue for enhancing piezoelectric performance. This thesis delved into the manufacturing of poly(vinylidene fluoride-co-hexafluoropropylene) (PVDF-HFP) nanofiber yarn via an electrospinning process to improve the mechanical and piezoelectric properties of poly(vinylidene fluoride-co-hexafluoropropylene) (PVDF-HFP) nanofiber yarn.

This research was guided by three key hypotheses that shaped the experimental approach. Firstly, it was hypothesized that optimizing fiber density through controlled electrospinning parameters could enhance the mechanical strength and piezoelectric response of the nanofiber yarn. Secondly, varying the draw ratio during the electrospinning process was expected to influence the molecular orientation and crystallinity of the nanofibers, thereby affecting their piezoelectric performance. Thirdly, using a novel twist-and-roll (spinning) device during electrospinning was anticipated to enable the production of twisted nanofiber yarns with improved mechanical properties and enhanced piezoelectric response due to increased molecular alignment.

To investigate these hypotheses, a custom electrospinning setup was designed and constructed, featuring an automated track system, an adjustable roll-to-roll collector, and an innovative twist-and-roll device. The automated track system and adjustable roll-to-roll collector facilitated continuous fiber collection and the production of large surface area fiber sheets suitable for roll-to-roll processes. Concurrently, the twist-and-roll device enabled the twisting of nanofibers into yarns, allowing for the exploration of the twisting hypothesis.

Various electrospinning parameters, including fiber densities and draw ratios, were systematically varied to optimize the mechanical and piezoelectric properties of the PVDF-HFP nanofiber yarn. The mechanical properties were rigorously evaluated through flick and stretch tests. Additionally, the piezoelectric performance was assessed through comprehensive electrical testing. By investigating the effects of these process parameters on the yarn's mechanical and piezoelectric characteristics, this thesis aims to contribute to the understanding of the intricate relationship between electrospinning conditions and the resulting properties of PVDF-HFP nanofiber yarn.

Ultimately, this research endeavored to pave the way for developing high-performance piezoelectric materials, unlocking their potential in a wide range of applications and advancing piezoelectric nanofiber technology.

## **Chapter 2**

### **Background**

#### **2.1 Nanofibers**

The concept of nanofibers has a long-standing history, with early investigations into electrospinning techniques dating back centuries, and the formal terminology of "nanofiber" and extensive research in this field emerging in the late 20th century, culminating in the widespread adoption and popularization of the "electrospinning" technology (14). Nanofibers are ultrafine fibrous structures with diameters typically less than 100 nanometers. An example shown in Figure 2, which can be fabricated from a diverse range of natural polymers, including collagen, cellulose, silk fibroin, keratin, gelatin, chitosan, and alginate, among others, owing to their unique structural and functional properties (15,16) and synthetic polymers, which include poly(lactic acid) (PLA), polycaprolactone (PCL) (17), polyurethane (PU), poly(lactic-co-glycolic acid) (PLGA) (15,16), poly(vinylidene fluoride) (PVDF) (18).

A variety of fabrication techniques, including drawing, electrospinning, self-assembly, template synthesis, and thermal-induced phase separation, have been developed for the production of nanofibers, with electrospinning being the most widely utilized method due to its straightforward setup, ability to continuously mass-produce nanofibers from diverse polymers, and capability to create ultrathin fibers with precisely controllable diameters, compositions, and orientations (19). Also, nanofibers can be prepared through the following methods: blow/jet spinning (20,21), centrifugal spinning (22), touch spinning (23), and force-spinning (24).

The high surface area-to-volume ratio of nanofibers renders them particularly attractive for various applications, including energy, environmental remediation, and biomedical engineering. The exceptional properties and promising application potential of nanofibers have garnered significant interest from both academic researchers and industry. Extensive scientific investigations have been undertaken to explore the fundamental characteristics and optimize the performance of these nano-scale materials (14,25).

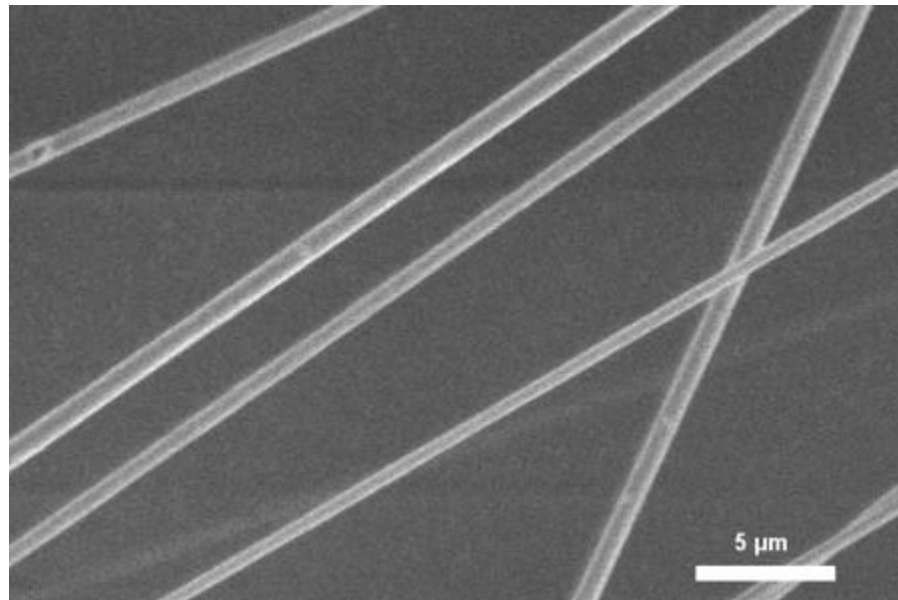


*Figure 2.* Aligned mesh SEM image of PVDF-HFP nanofibers

## **2.2 Electrospinning Overview**

Electrospinning despite its origins dating back to the early 1900s (26,27), has become a widely adopted and versatile technique in the 21st century, particularly in the biomedical sector, enabling the fabrication of fibers with specific properties that have been utilized in a large number of applications across more than 200 different polymers (27). In the electrospinning process, a powerful direct current electric field draws a dissolved

polymer mixture from a needle toward a grounded target. A mechanical pump pushes the solution to the needle's end, creating a distinctive conical shape known as a Taylor cone (28) due to the high surface tension. The high-voltage power supply charges the needle tip and droplet, causing the droplet to burst and emit a jet stream of fiber that stretches and travels to the collector, with the solvent evaporating during this process, resulting in the random deposition of polymeric fibers on the collector surface (29). Predicting and quantifying the electric charge that droplets accumulate is crucial for precisely controlling their movement. James Maxwell derived a limiting prediction for the charge a droplet should gain upon touching an electrode. He demonstrated that the amount of charge  $Q$  a perfectly conductive sphere would acquire from a perfectly conductive flat electrode is given by

$$Q = \frac{2}{3} \pi^3 \epsilon \epsilon_0 a^2 E \quad (1)$$

Here,  $a$  represents the sphere's radius,  $\epsilon \epsilon_0$  is the permittivity of the surrounding liquid, and  $E$  is the applied electric field. Several parameters, such as fiber diameter, surface morphology, and crystalline phases, influence the mechanical, physicochemical, and piezoelectric properties of fibers produced via electrospinning, an illustration shown in Figure 3. These parameters include relative humidity (RH), temperature, polymer concentration, elasticity, molecular weight, polarity, solvent, polydispersity, solution additives, electrical potential, and the distance between the tip and the collector. This work generated PVDF-HFP nanofibers using the electrospinning technique for the experiments (29–35).

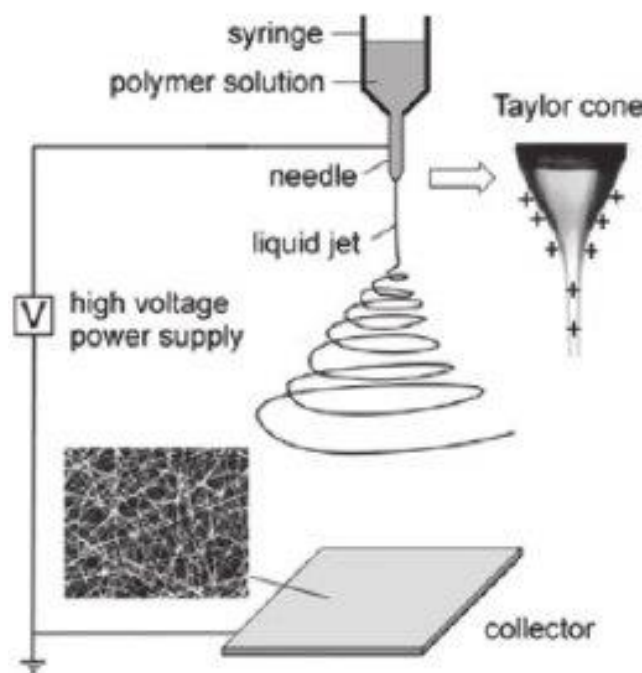


*Figure 3. Schematics Illustration of Electrospinning Process (36)*

The electrostatic forces during electrospinning can induce conformational changes in the polymer, promoting a straighter all-trans (TTTT) conformation through disentanglement and parallel packing. This is necessary for forming the  $\beta$ -phase crystalline structure in PVDF, thereby enhancing the piezoelectric properties of the resulting electrospun nanofibers (28,37). Electrospinning is a more efficient and cost-effective technique than electrical poling for producing piezoelectric polymers, as it charges the polymer solution during fabrication rather than post-fabrication, leading to a higher  $\beta$ -phase fraction and permanent piezoelectric properties while also potentially offering advantages in membrane morphology, such as increased porosity, compared to the conventional porous structure obtained through electrical poling (29,38).

### **2.3 Self-Bundling Electrospinning for Nanoyarn Formation**

Self-bundling electrospinning is a conventional method for producing continuous nanoyarn from electrospun nanofibers. It involves using a grounded needle tip to induce the self-bundling behavior of nanofibers ejected from a high-voltage charged needle tip. The self-bundled nanofibers are then pulled back and wound onto a rotating drum to form a continuous nanoyarn (39,40).

The key factor for successful self-bundling electrospinning is the conductivity of the spinning solution. Organic salts like benzyl triethylammonium chloride (BTEAC) are added to the polymer solution to improve its conductivity. This technique has been used to produce nanoyarns from various synthetic polymers such as polyacrylonitrile (PAN), poly(L-lactic acid) (PLLA), poly(3-hydroxybutyrate-co-3-hydroxy valerate) (PHBV), and poly(m-phenylene isophthalamide) (PMIA), demonstrating its versatility (40).

The self-bundling of nanofibers during electrospinning in Figure 4 is attributed to the electrostatic interactions between the charged nanofiber jets. As the nanofibers are ejected from the charged needle, they carry the same charge and experience repulsive forces. However, the presence of the grounded needle tip creates an electric field that induces the nanofibers to align and bundle together (39). The proposed mechanism suggests that the nanofibers initially undergo a whipping instability, causing them to stretch and thin down. As they approach the grounded needle tip, the electric field aligns the nanofibers parallel to each other, and the electrostatic interactions between the like-charged nanofibers cause them to bundle together (39,40).

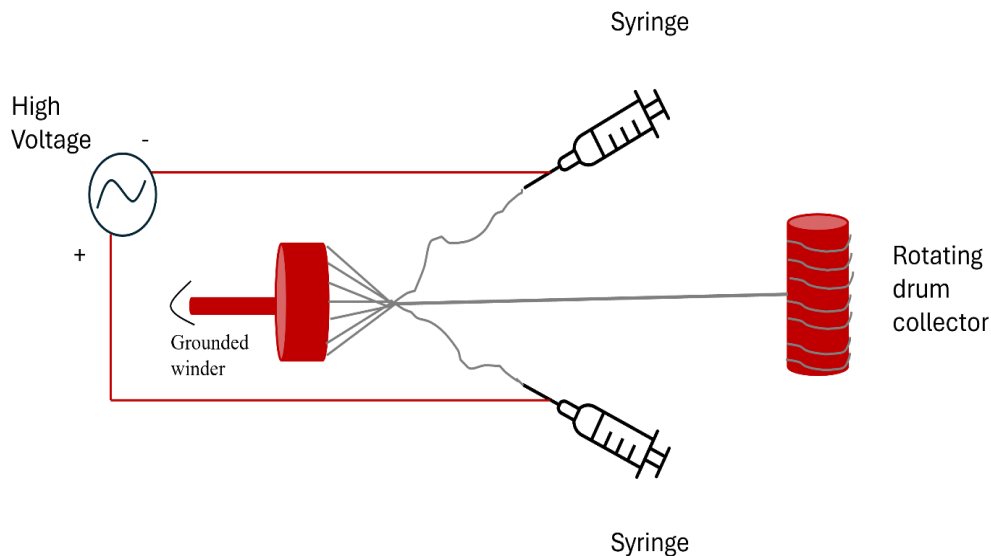


*Figure 4. Self-bundling electrospinning system*

The self-bundling electrospinning system offers several advantages, including simplicity, energy efficiency, and the ability to produce continuous nanoyarns from various polymers. However, it also has limitations, such as the difficulty in precisely controlling the self-bundling behavior during the nanoyarn formation process, resulting in low-quality nanoyarns, the inability to be post-drawn for better mechanical properties, and a high yarn breakage rate. Attempts have been made to commercialize this system to make continuous yarns, but they have all failed. To address these limitations, this research study will utilize a different electrospinning setup consisting of an automated parallel track system, an adjustable roll-to-roll collector, and a conjugated yarn spinning device to improve nanofibers' bundling or twisting and alignment. Additionally, it is hypothesized that this electrospinning system will increase the nanoyarn production rate and make it commercially scalable.

## 2.4 Ferroelectricity

Some materials possess a unique characteristic called ferroelectricity, which involves a naturally occurring electric alignment that can be flipped by introducing an external electric force. The ferroelectric effect can be described mathematically using the following equation (41).

$$P = P_s + \chi_e * E \quad (2)$$

Where: P is the electric polarization (C/m<sup>2</sup>), P<sub>s</sub> is the spontaneous polarization (C/m<sup>2</sup>),  $\chi_e$  is the electric susceptibility of the material, E is the applied electric field (V/m)

The spontaneous polarization, P<sub>s</sub>, is a key characteristic of ferroelectric materials. It arises from the asymmetric arrangement of atoms within the crystal structure, which results in a net electric dipole moment even in the absence of an external electric field. When an external electric field is applied to a ferroelectric material, the spontaneous polarization can be reversed, leading to a hysteresis loop in the relationship between the polarization and the applied field (42).

Dielectric materials are insulators that an electric field can polarize. Ferroelectrics are a subset of dielectrics that exhibit spontaneous and reversible electric polarization. Figure 5 shows the relationship between ferroelectric, pyroelectric, piezoelectric, and dielectric materials. Piezoelectric materials, which belong to the dielectric group, can generate a net separation of positive and negative charges when subjected to mechanical stress due to their non-centrosymmetric crystal structure. Ferroelectrics are a specialized subset of pyroelectric materials, where all ferroelectrics are also pyroelectric and piezoelectric, but not all pyroelectric or piezoelectric materials are ferroelectric. Their

crystal symmetry governs the categorization of these materials, as all crystalline substances belong to one of the 32 crystallographic point groups, with 20 being piezoelectric and ten being ferroelectric (41).

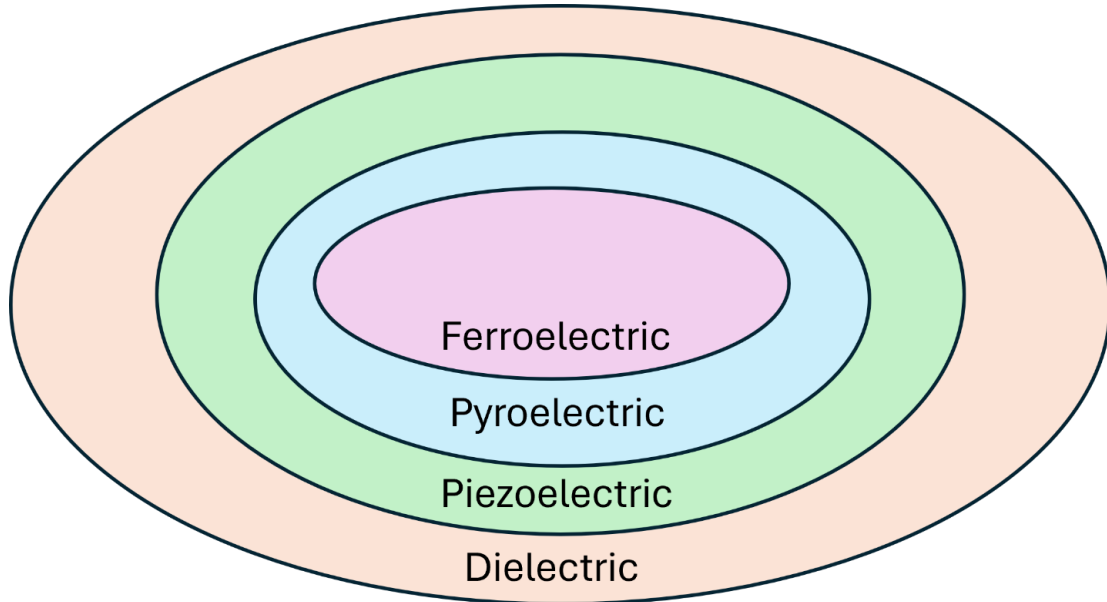


*Figure 5.* Relationship between Ferroelectric, Pyroelectric, Piezoelectric, and Dielectric materials (43)

#### ***2.4.1 Mechanism of Piezoelectricity***

Piezoelectricity is an electromechanical interaction that occurs in certain non-centrosymmetric crystalline materials. Before applying an external force, the net dipole moment in the material's structural unit is zero, as the positive and negative charge centers are balanced, resulting in an electrically neutral arrangement. The piezoelectric effect involves the generation of an electric dipole moment within a material in response to an applied mechanical stress. A typical illustration is shown in Figure 6. The basic structural configuration deforms, causing a separation of the positive and negative charge centers. This disruption in the charge balance leads to the emergence of fixed electric charges on

opposing material surfaces. The piezoelectric effect is reversible, as applying an electric field can also induce mechanical deformation in the material (44–47).

The brothers Pierre and Jacques Curie made a groundbreaking discovery in 1880 when they identified the direct piezoelectric effect. They observed this phenomenon in various single-crystal materials, including quartz ( $\text{SiO}_2$ ), Rochelle salt, tourmaline, topaz, and even sugar cane (47). This effect results in the production of an electric charge that correlates directly with the amount of mechanical force applied. In the years following this discovery, quartz emerged as a prominent and extensively utilized piezoelectric substance. It wasn't until several decades later those researchers identified polycrystalline piezoelectric ceramics, which are oxide-based materials. The pioneering example of these was  $\text{BaTiO}_3$ , first discovered during the Second World War and initially employed as a dielectric in solid-state capacitors. The unique property of these piezoelectric materials to transform mechanical energy into electrical energy, and the reverse, has led to their adoption in numerous applications, driving significant technological progress (48).

Piezoelectric ceramics like  $\text{BaTiO}_3$  and PZT have been extensively researched but have limited flexibility and high processing temperatures. In contrast, piezoelectric polymers such as PVDF, PVDF-HFP, and PVDF-TrFE offer advantages that make them attractive alternatives. These polymers can be quickly processed at low temperatures into complex shapes due to their flexibility, a key advantage over rigid ceramics. Additionally, piezoelectric polymers have other unique benefits, including easy processing, low manufacturing costs, and high compatibility with biological applications, making them well-suited for various uses where the flexibility and versatility of polymers are desirable (49).

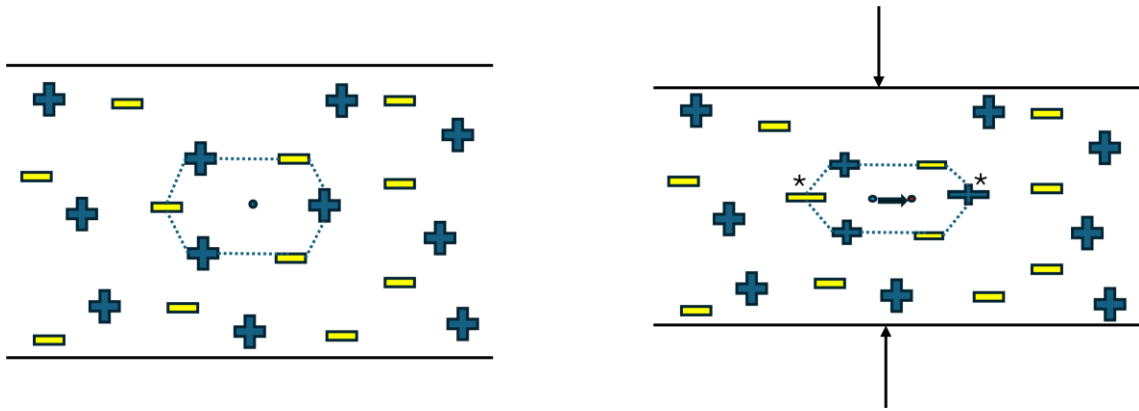


*Figure 6.* The illustration shows a two-dimensional grid model of a piezoelectric substance. A unit cell is outlined by dotted lines. The left portion displays the material in its relaxed state, where the center points of positive and negative charges align, indicated by a black dot. The right section presents the material under compression. This compression causes the material to expand horizontally, leading to a separation of positive and negative charges, marked by asterisks (\*). This charge separation results in the formation of an electric dipole. Blue and yellow dots represent the center points of the positive and negative charges, respectively, in this compressed state (47).

#### ***2.4.2 Piezoelectric Effect***

Piezoelectricity is a characteristic of specific non-conducting substances that allows them to produce an electric charge on their exterior when exposed to mechanical force. These materials also exhibit the reverse property: they can physically deform or strain when exposed to an electric field. As illustrated in Figure 7, piezoelectric materials demonstrate both direct and inverse piezoelectric effects. The direct effect occurs when mechanical stress induces electric polarization, while the inverse effect involves dimensional alterations in response to an applied electric field. The unique capacity of these materials to transform electrical energy into mechanical energy and vice versa makes them invaluable components in a wide array of electromechanical systems and devices (50).

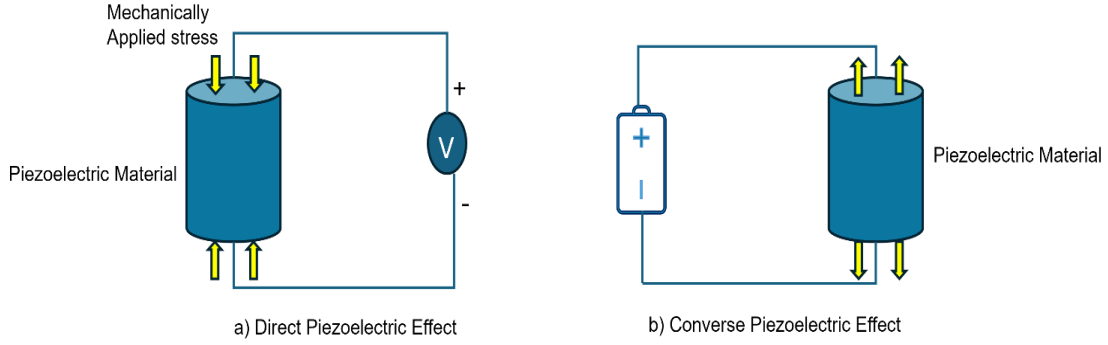


*Figure 7.* The illustration depicts two key aspects of piezoelectricity: the direct effect, where mechanical stress produces an electric charge, and the converse effect, where an applied electric field results in physical deformation or strain. This schematic visualization demonstrates the bidirectional nature of the piezoelectric phenomenon (47)

The linear relationship between these phenomena is quantified by the piezoelectric coefficient, a third-rank tensor that links a first-rank tensor or vector (representing either electric displacement or field) with a second-rank tensor (denoting stress or strain). Consequently, the mathematical expressions describing piezoelectric behavior can be formulated as follows (where  $i$ ,  $j$ , and  $k$  each represent 1, 2, or 3)

$$D_k = d_{kij} \times T_{ij} \quad (3)$$

$$S_{ij} = d_{kij}^* \times E_k \quad (4)$$

The electric displacement  $D_k$  ( $C/m^2$ ) is related to the electric field  $E_i$  ( $V/m$ ) and the strain  $S_{ij}$  or stress  $T_{ij}$  ( $N/m^2$ ) through piezoelectric constants. The piezoelectric charge or strain constant  $d$  (in  $pC/N$  or  $pm/V$ ) connects the electric field/displacement and the mechanical strain or stress. The subscripts of  $d$  denote the directions of the electric and mechanical quantities.  $k$  represents the electric field/displacement direction, and  $m$  represents the mechanical stress/strain direction. It is important to note that the

piezoelectric constants  $d_{kij}$  or  $d_{kij}^*$  are equal ( $i, j, k = 1, 2, 3$ ), representing the coupling between the electrical and mechanical domains.

In addition to the piezoelectric charge/strain constant  $d$ , three other piezoelectric constants are used in specialized design cases: the piezoelectric voltage constant  $g$ , the electromechanical coupling factor  $k$ , and the elastic compliances. These constants are partial derivatives under different boundary conditions, such as constant stress, electric field, displacement, or strain. The different forms of piezoelectric constants allow the relationships between the electrical and mechanical quantities to be expressed in various ways depending on the design requirements and boundary conditions (46,51–53).

The piezoelectric coefficient ( $d_{xy}$ ) quantifies the strength of the connection between electrical and mechanical properties in piezoelectric materials. The directionality of this coefficient is crucial for understanding and utilizing these materials effectively as shown in Figure 8. The performance of piezoelectric devices is highly dependent on the orientation of both the applied stress and the electric field. For example, the  $d_{33}$  mode coefficient of lead zirconate titanate (PZT), a widely used piezoelectric material, is approximately twice as large as the  $d_{31}$  coefficient, with values of 225 pC/N and 110 pC/N, respectively. This means that the voltage output generated in the  $d_{33}$  mode is anticipated to be significantly higher than that in the  $d_{31}$  mode (54,55).

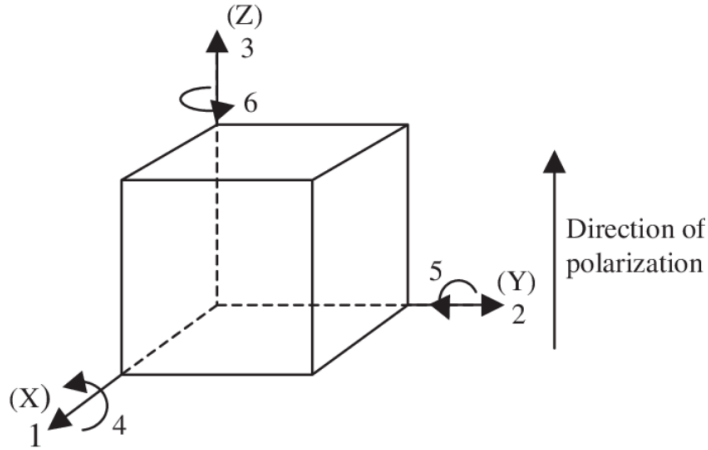


Figure 8. Notation of crystal axes with the polarization of light passing through the crystal (56)

The piezoelectric coefficient ( $d_{xy}$ ) represents the charge generated per unit of applied force or the deflection per unit of electrical voltage. The piezoelectric coefficient has an intrinsic vectorial nature, meaning it is directional. It is usually written as  $d_{xy}$ , where  $x$  indicates the direction of the electric field, and  $y$  indicates the direction of the stress or strain. The two most common operation modes for piezoelectric materials are 31 and 33. Longitudinal piezoelectric coefficient ( $d_{33}$ ): the coefficient relating to the polarization in the direction of the applied field. Transverse piezoelectric coefficient ( $d_{31}$ ): the coefficient relating the polarization perpendicular to the applied field. Tangential piezoelectric coefficient ( $d_{15}$ ): the coefficient relating the polarization to a shear stress (57–59).

## 2.5 Triboelectricity

Static electricity, also known as triboelectricity, is a phenomenon that occurs when two different materials come into contact or rub against each other. This causes electrons (negatively charged particles) to move from one material to another. The triboelectric series ranks materials based on how easily they can gain or lose electrons during contact. Some materials are more likely to gain electrons, while others are more likely to lose them (60,61). The transfer of electrons, ions (charged atoms or molecules), or material fragments from one surface to another causes static electricity.

For solid materials rubbing against each other, the transfer of electrons is the main mechanism. Electrons move from the material with more electrons (higher electron density) to those with fewer electrons (lower electron density). This is driven by the tendency of electrons to fill the lowest available energy levels (surface states) on the material surfaces (60). The transfer of charged ions or particles is responsible for static electricity for solids and liquids or two liquids in contact. The triboelectric series can predict whether a material will gain or lose electrons (become positively or negatively charged) when in contact with another material (62).

PVDF (polyvinylidene fluoride) is a polymer material that exhibits a high surface charge density when it comes into contact with other materials, making it an attractive choice for triboelectric applications. PVDF's position in the triboelectric series allows it to readily gain or lose electrons when paired with suitable materials (63,64). Researchers have explored various forms of PVDF, such as thin films, nanofibers, and composites, to enhance its triboelectric performance. Triboelectric nanogenerators (TENGs) are a promising technology that harvests energy from mechanical motions and vibrations using

the triboelectric effect. PVDF has been extensively used as a friction layer in TENGs due to its high triboelectric charge density and mechanical flexibility (63–65). One notable example is the development of flexible and wearable PVDF-based TENGs for harvesting energy from human body movements (kinetic energy harvesting). To further improve the triboelectric performance of PVDF, researchers have incorporated various nanofillers (nanoparticle additives) and developed nanostructured PVDF materials (65–67).

Adding nanoparticles like BaTiO<sub>3</sub> (barium titanate), ZnO (zinc oxide), and carbon nanotubes to PVDF has improved the triboelectric charge density and output power of PVDF-based TENGs (68). Fabricating PVDF nanofibers and nanostructured surfaces increases the effective surface area and enhances triboelectric charge generation (charge transfer efficiency) (69–71). These nanostructured PVDF materials have demonstrated improved triboelectric performance and potential applications in energy harvesting, self-powered sensors (sensors that generate their power), and other triboelectric devices (69–72). PVDF has also been combined with other triboelectric materials to create hybrid and composite TENGs, taking advantage of the synergistic effects of different materials (68,70). For example, PVDF has been integrated with materials like PDMS (polydimethylsiloxane), PTFE (polytetrafluoroethylene), and graphene to form composite structures with enhanced triboelectric properties (improved charge generation and output power) (68). These hybrid TENGs have shown promising results in terms of output power, stability, and versatility for various applications like wearable electronics and self-powered systems (70,72).

In summary, PVDF materials have been extensively studied in triboelectricity research due to their excellent triboelectric properties and potential for energy harvesting

and self-powered systems (68–72). Electrospun PVDF nanofibers work effectively in TENG applications due to their triboelectric properties, high surface roughness, flexibility, stretchability, ability to form composites and hybrid devices, and the underlying triboelectric principle of charge transfer upon contact and separation (69,70,72). These unique characteristics make PVDF nanofibers a promising material for developing high-performance TENGs for energy harvesting, self-powered systems, and various sensing applications.

## 2.6 Piezoelectric Materials

Piezoelectric materials can be classified into Inorganic Piezoelectric Ceramics, Piezoelectric Polymers, Bio-Piezoelectric, and Composite Piezoelectric materials as shown in Figure 9 (73).

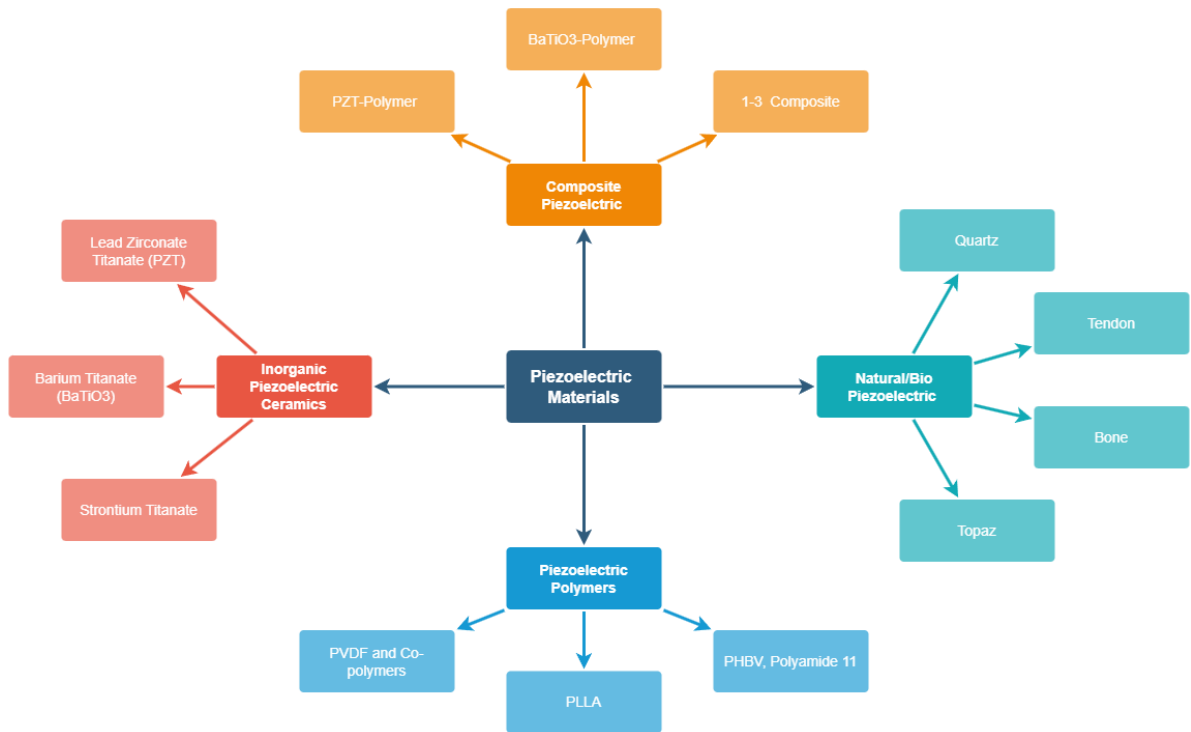


*Figure 9.* Overview of the major classes of Piezoelectric materials with some representative examples within each category.

### 2.6.1 Natural/Bio Piezoelectric

Natural piezoelectric materials, such as quartz, bone, and specific proteins, exhibit a non-centrosymmetric crystal structure, as shown in Figure 10 which implies that the arrangement of atoms is not symmetric about a central point (74,75). This asymmetric arrangement of atoms within the unit cell is a crucial requirement for the piezoelectric effect to occur. When an external electric field is applied to the natural piezoelectric material, the following happens at the unit cell level: the asymmetric arrangement of atoms in the unit cell causes a separation of positive and negative charges, forming an electric dipole. The applied electric field causes the unit cell to deform, either by expanding or contracting along specific axes, depending on the direction of the electric field. The deformation of the unit cell leads to a change in the net polarization of the material, which can be detected as an electric charge or voltage (47,76).

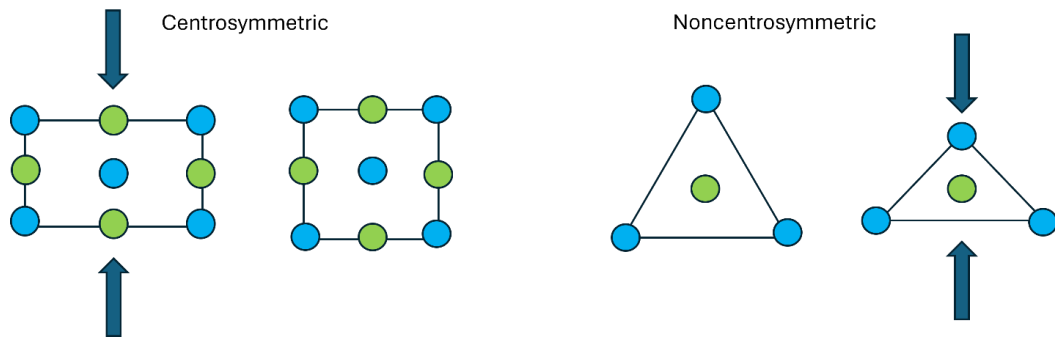


Figure 10. Centrosymmetric and Non-centrosymmetric Crystal Structure (77)

Natural and bio-based piezoelectric materials have gained significant attention recently due to their potential applications in various fields, including biomedical devices, energy harvesting, and sustainable building structures. Bone is one of the most well-known

natural piezoelectric materials, exhibiting this behavior due to collagen fibrils and hydroxyapatite crystals. Other natural piezoelectric materials include silk, cellulose, and chitin. Silk has been used to develop flexible and biodegradable sensors, energy harvesters, and smart materials, with a piezoelectric coefficient ( $d_{33}$ ) of around 38 pC/N. To enhance their piezoelectric properties, cellulose and chitin can be processed into various forms, such as nanofibers, films, and composites (78,79).

In addition to natural piezoelectric materials, researchers have also explored bio-based piezoelectric materials, such as gelatin, poly(L-lactic acid) (PLLA), and poly( $\gamma$ -benzyl L-glutamate) (PBLG). Gelatin has a piezoelectric coefficient ( $d_{33}$ ) of around -20 pC/N and has been used for pressure sensor applications. Aligned PLLA nanofibers have a piezoelectric coefficient ( $d_{14}$ ) of around 19 pC/N and have been used for pressure sensors and electrical stimulators. Aligned PBLG nanofibers embedded in a PDMS matrix have a piezoelectric coefficient ( $d_{33}$ ) of around 54 pC/N (13). While generally lower than traditional inorganic piezoelectric materials, these materials' piezoelectric coefficients offer advantages in biocompatibility, flexibility, and environmental friendliness.

### ***2.6.2 Inorganic Piezoelectric Ceramics***

Inorganic piezoelectric ceramics exhibit the piezoelectric effect, which is the ability to generate an electrical charge in response to mechanical stress. These ceramics are widely used in various applications, including sensors, actuators, and energy-harvesting devices. One of the most commonly used inorganic piezoelectric ceramics is lead zirconate titanate (PZT) (73,80). PZT is a composite material formed by combining two distinct compounds: the antiferroelectric lead zirconate ( $\text{PbZrO}_3$ ) and the ferroelectric lead titanate ( $\text{PbTiO}_3$ ).

This blend results in a material with remarkable characteristics, including a high dielectric constant, strong electromechanical coupling, and superior piezoelectric performance. These exceptional properties have made PZT a widely favored option across numerous applications (80).

Barium titanate ( $\text{BaTiO}_3$ ) stands out as another significant inorganic piezoelectric ceramic. It was among the first piezoelectric ceramics to find practical use in transducer applications, notably in SONAR technology.  $\text{BaTiO}_3$  boasts impressive characteristics, including a high dielectric constant and a substantial electromechanical coupling coefficient. However, it has a limitation: its Curie point - the temperature at which the material transitions from a non-centrosymmetric ferroelectric state to a centrosymmetric paraelectric state - is comparatively low, occurring at approximately  $120^\circ\text{C}$  (80).

In addition to PZT and  $\text{BaTiO}_3$ , other inorganic piezoelectric ceramics, such as sodium bismuth titanate (BNT) and potassium sodium niobate (KNN), have also been extensively studied and developed. These materials have shown promising properties and are being explored as lead-free alternatives to PZT (73,80). Research studies have also investigated the use of porous piezoelectric ceramics to control internal stress and improve the overall performance of these materials, particularly PZT and  $\text{BaTiO}_3$ , which have been widely used in various applications due to their excellent piezoelectric properties. Ongoing research is focused on developing new lead-free piezoelectric ceramics and exploring the use of porous structures to enhance the performance of these materials further.

### 2.6.3 Piezoelectric Polymers

Piezoelectric polymers exhibit the piezoelectric effect, which is the ability to generate an electric charge in response to mechanical stress or strain. These polymers have gained significant attention due to their unique properties, which make them suitable for various applications, including sensors, energy harvesters, and actuators (13,81,82). One of the most widely studied piezoelectric polymers is poly(vinylidene fluoride) (PVDF), and its copolymers, such as polyvinylidene hexafluoropropylene (PVDF-HFP), poly(vinylidene fluoride-co-trifluoro ethylene) (P(VDF-TrFE)). PVDF is a semi-crystalline polymer that can exhibit different crystalline phases, with the  $\beta$ -phase being the most desirable for piezoelectric applications due to its high polarization. Also, polylactic acid (PLA) and poly(L-lactide) (PLLA) have been investigated for their piezoelectric properties and potential use in tissue engineering and implantable devices (73,83).

**2.6.3.1 Polyvinylidene Fluoride (PVDF).** Polyvinylidene fluoride (PVDF) is a widely studied piezoelectric polymer due to its unique properties, flexibility, lightweight, and ease of processing. It is generally acknowledged that PVDF ( $d_{31} \approx 20\text{-}25$  pC/N and  $d_{33} \approx 20\text{-}35$  pC/N), as a semi-crystalline polymer, whose piezoelectricity mainly depends on its crystalline phase which has five polymorphs:  $\alpha$ ,  $\beta$ ,  $\gamma$ ,  $\delta$  and  $\epsilon$  (84,85). Figure 11 depicts a chain conformation for PVDF's  $\alpha$ ,  $\beta$ , and  $\gamma$  crystalline phases. The  $\alpha$ -phase (crystal form II) has a trans-gauche-trans-gauche (TGTG') conformation. It is the most common and stable phase under normal conditions. The  $\beta$ -phase (crystal form I) has an all-trans (TTTT) planar zigzag conformation. The  $\beta$ -phase is the most desirable for piezoelectric applications due to its high polarization. The  $\gamma$ -phase (crystal form III) has a TTTGTTTG'

conformation,  $\delta$ -phase has a TGTG' conformation, and  $\varepsilon$ -phase is the least studied, and its structure is not well-established (86–88).

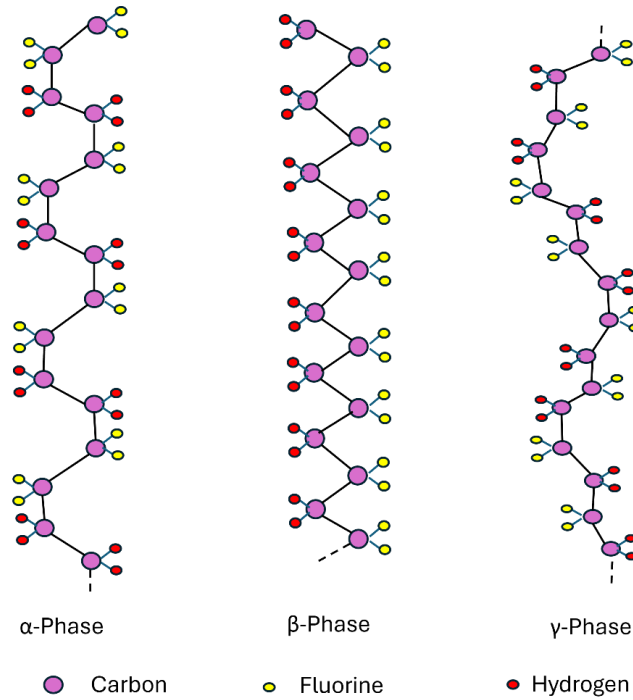


Figure 11. A chain conformation for PVDF's  $\alpha$ ,  $\beta$ , and  $\gamma$  crystalline phases (89).

Various techniques to enhance the piezoelectric properties of PVDF have been researched, such as stretching (90), polarization under a high electrical field (91), thermal annealing (92), nanoconfinement-induced crystal orientation (93), and nanocomposites with conductive fillers. Adding conductive fillers (84) like silver nanowires (AgNWs) can act as nucleating agents, promoting the formation of the  $\beta$ -phase and improving the piezoelectric properties of PVDF-based composites. However, excessive fillers can lead to crystal defects and lower the degree of crystallinity, resulting in worse piezoelectric performance (94).

The piezoelectric coefficients of PVDF depend on factors such as stretch ratio, temperature, crystallinity, and poling conditions. The two principal modes of operation for energy harvesters using PVDF are the d31 and d33 coefficients, which describe the electric polarization created perpendicular to and in the same direction as the applied stress, respectively (85). Studies have shown that PVDF films exhibit good repeatability and linearity in their piezoelectric response under quasi-static compression. Additionally, PVDF films can effectively capture the propagation of stress waves under high loading rates, with the material exhibiting higher failure strength at higher strain rates. Measurements of the piezoelectric coefficients of PVDF films have shown that the difference in the coefficients under extremely low ( $10^{-2} \text{ s}^{-1}$ ) and high ( $10^5 \text{ s}^{-1}$ ) strain rates is only around 10%, indicating the stability of the piezoelectric properties of PVDF over a wide range of loading conditions (93). Figure 12 shows the structural formula for PVDF. Piezoelectric PVDF nanofibers fabricated through electrospinning and various material design strategies, including filler incorporation and fiber alignment, have shown great potential for a wide range of applications, such as sensors, energy harvesters, and actuators (95–98).

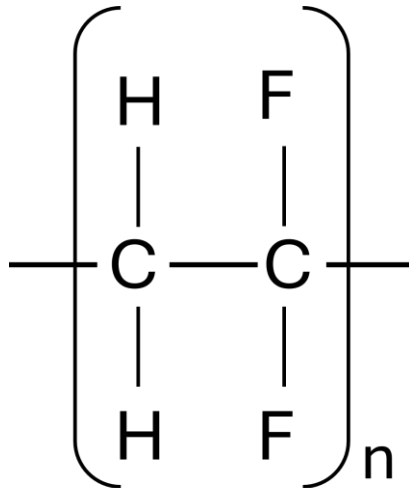


Figure 12. The structural formula of polyvinylidene fluoride PVDF (99)

**2.6.3.2 Poly(vinylidene fluoride-co-hexafluoropropylene) (PVDF-HFP).** While PVDF and PVDF-HFP share similarities in their piezoelectric and ferroelectric properties, the copolymer PVDF-HFP structural formula as shown in Figure 13 exhibits some distinct advantages, such as improved flexibility and processability, due to the addition of the HFP comonomer in PVDF-HFP and the potential for further enhancement through the addition of functional fillers. PVDF-HFP is a promising piezoelectric copolymer that can be further optimized by incorporating fillers and applying specific processing techniques, such as stretching and poling (100–104).

Electrospinning is an effective technique for fabricating PVDF-HFP nanofibers with enhanced piezoelectric performance. The electrospinning process and parameters can be optimized to promote the formation of the desired polar  $\beta$ -phase in the PVDF-HFP structure, which is crucial for achieving high piezoelectricity (97,98,105). Also, incorporating  $\text{CoFe}_2\text{O}_4$  nanoparticles into PVDF-HFP has been reported to improve the

material's piezoelectricity. Additionally, the preparation of PVDF-HFP/Ni composite films through solution casting, uniaxial stretching, and high electric field poling has increased the calibrated open-circuit voltage by up to 23% compared to pure PVDF-HFP films (103,104).

The piezoelectric performance of electrospun PVDF-HFP nanofibers is greatly affected by their shape and internal arrangement. Scientists have investigated various structural configurations, including highly aligned nanofibers, core-shell architectures, and multi-layered composite designs, aiming to boost the piezoelectric output of these materials. To examine the development of crystalline structures and phase compositions in these electrospun PVDF-HFP nanofibers, researchers have utilized advanced analytical methods such as x-ray diffraction (XRD), Fourier transform infrared spectroscopy (FTIR), and differential scanning calorimetry (DSC). These studies have shed light on the underlying processes that lead to enhanced piezoelectric properties in the nanofibers. Achieving optimal shape and structure in electrospun PVDF-HFP nanofibers is essential for realizing their full piezoelectric potential (97,98,105).

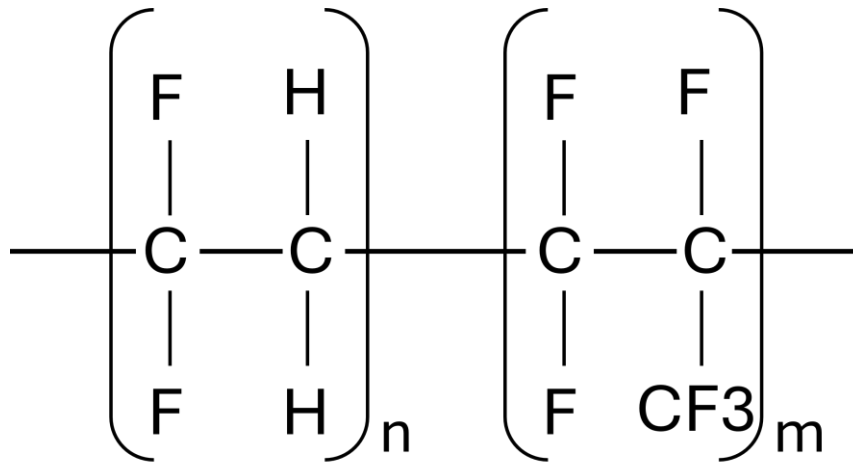


*Figure 13.* The structural formula for poly(vinylidene fluoride-co-hexafluoropropylene) PVDF-HFP (99)

**2.6.3.3 Poly(vinylidene fluoride-co-trifluoro ethylene) (PVDF-TrFE).** PVDF-TrFE is a copolymer of vinylidene fluoride (VDF) and trifluoro ethylene (TrFE), and it exhibits a non-centrosymmetric crystal structure essential for piezoelectricity. Poly(vinylidene fluoride-co-trifluoro ethylene) (PVDF-TrFE) structural formula as shown in Figure 14 is a widely studied piezoelectric polymer that has attracted significant research interest due to its excellent piezoelectric properties and potential applications (106,107). The  $\beta$ -phase in PVDF-TrFE exhibits a non-centrosymmetric crystal structure, a prerequisite for piezoelectricity (83).

Research studies have investigated various approaches to improve the piezoelectric performance of PVDF-TrFE, with a focus on manipulating crystal orientation and creating nanostructures. One notable study described the creation of PVDF-TrFE nanotube arrays aligned vertically, where the nanotubes' crystallographic polar axes were oriented along their length. This specific crystal arrangement led to significant improvements in

piezoelectric strain and voltage coefficients, achieving values up to 1.97 and 3.40 times greater than those observed in traditional spin-coated films. Additionally, researchers have explored the integration of inorganic materials, such as ceramic particles or carbon nanotubes, into PVDF-TrFE matrices. This strategy aims to enhance both the piezoelectric properties and mechanical characteristics of the resulting composite materials (73,106,108).

The mechanical properties of the electrospun PVDF-TrFE nanofibers also play a crucial role in their performance and stability as piezoelectric devices. Researchers have explored ways to improve mechanical strength by combining PVDF-TrFE with polymers or reinforcing the nanofibers with nanomaterials. Electrospun PVDF-TrFE nanofibers have demonstrated great potential for piezoelectric applications, such as sensors, energy harvesters, and flexible electronics. Ongoing research focuses on developing advanced materials and structures to further enhance the piezoelectric properties and expand the practical applications of these nanofibers (98,109).

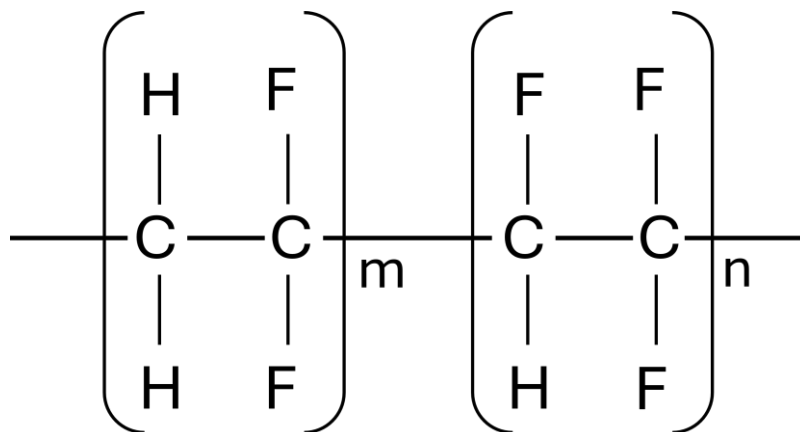


Figure 14. The structural Formula for Poly(vinylidene fluoride-co-trifluoro ethylene) (PVDF-TrFE) (110)

**Table 1**

*Comparing Significant Mechanical and Piezoelectric Properties of PVDF, PVDF-HFP, and PVDF-TrFE (27,85,111–113)*

Properties	Units	PVDF	PVDF-HFP	PVDF-TrFE
Density	g/cm <sup>3</sup>	1.78	1.77	1.89
Curie Temperature	°C	160-180	110-135	100-120
Piezo-stress constant (g <sub>33</sub> )	mV.m/N	330-400	200-300	40-60
Piezo-strain constant (d <sub>33</sub> )	pC/N	20-30	10-15	30-40
Dielectric constant	-	8-12	6-7	10-13
Biocompatibility	-	Good	Good	Good
Piezoelectricity	-	High	Moderate	Very High
Flexibility	-	Good	Excellent	Good

#### ***2.6.4 Composite Piezoelectric***

Composite piezoelectric materials are a class of functional materials that combine piezoelectric active materials, such as ceramics or single crystals, with non-piezoelectric passive polymers. These composites are designed to leverage the advantages of both the active and passive phases, resulting in enhanced properties compared to their components (114). One common example of a composite piezoelectric material is the PZT-polymer composite. PZT (lead zirconate titanate) is a widely used piezoelectric ceramic known for its high electromechanical coupling and piezoelectric coefficients. Combining PZT with a polymer matrix, such as epoxy or polyurethane, the resulting composite can exhibit improved flexibility, lower acoustic impedance, and higher coupling coefficients than monolithic PZT ceramics (115).

Another example is the BaTiO<sub>3</sub>-polymer composite. Barium titanate (BaTiO<sub>3</sub>) is a ferroelectric ceramic with piezoelectric properties. Incorporating BaTiO<sub>3</sub> particles into a polymer matrix can produce composites with enhanced piezoelectric and dielectric properties, making them suitable for energy harvesting and sensing applications. A specific type of composite piezoelectric material is the 1-3 composite, where the piezoelectric ceramic phase is continuous in one direction. In contrast, the polymer phase is constant in the other two directions. This connectivity pattern can provide lower acoustic impedance, higher coupling coefficients, and other benefits compared to other composite configurations. The versatility of composite piezoelectric materials allows for their use across diverse sectors. These include medical fields such as ultrasound imaging and treatments, marine technologies like underwater acoustic detection, infrastructure maintenance through structural health monitoring, and sustainable energy solutions via

energy harvesting. The adaptability of these composites stems from the ability to fine-tune their characteristics by modifying their composition, structural connectivity, and manufacturing techniques. This flexibility makes them highly suitable for a broad spectrum of practical applications (116–118).

**Table 2**

*Comparing Significant Mechanical and Piezoelectric Parameters for PVDF, PZT, and BaTiO<sub>3</sub> (85,112,119)*

Properties	Units	PVDF	PZT	BaTiO <sub>3</sub>
Density	g/cm <sup>3</sup>	1.78	7.5-8	5.7
Curie Temperature	°C	160-180	200-350	120
Piezo-stress constant (g <sub>33</sub> )	mV.m/N	330-400	10-30	10-20
Piezo-strain constant (d <sub>33</sub> )	pC/N	20-30	200-600	190
Dielectric constant	-	8-12	300-3500	1700-4000
Biocompatibility	-	Good	Poor	Good
Piezoelectricity	-	Moderate	Excellent	Good
Flexibility	-	Excellent	Poor	Good

## 2.7 Energy Harvesting and Applications

Energy harvesters, also referred to as power harvesters, are mechanisms designed to capture and convert ambient energy from the environment into usable electrical power.

These devices can supply electricity to small electronic gadgets or recharge batteries, reducing reliance on battery replacements and conventional power sources. They are particularly valuable in remote or inaccessible locations where regular battery maintenance is challenging. The scale and complexity of energy harvesters vary widely, ranging from miniature devices powering individual sensors to larger systems capable of generating substantial electrical output. Their effectiveness is determined by the nature of the energy source and the specific technology utilized. Scientists and engineers are continually advancing energy harvesting technologies to enhance their efficiency, dependability, and applicability across diverse sectors. These include the Internet of Things (IoT), wireless communication, remote sensing, and biomedical applications. In the medical field, wearable energy harvesting sensors facilitate ongoing, non-invasive, real-time monitoring of human health and physiological performance. The ongoing development of these technologies aims to make them more practical and widely applicable, addressing the growing need for sustainable and autonomous power sources in various industries and applications (120).

For close to two decades, scientists have been investigating energy harvesting technologies as a potential replacement for traditional power sources like batteries in compact, low-power electronic devices. The primary motivation has been to address the persistent challenge of limited battery life and the need for frequent recharging or replacement, particularly in portable, remote, and implantable devices. Environmental energy is typically available in the forms of solar, thermal, and vibrational energy. Among these, vibration is particularly ubiquitous, present in both natural environments and human-made structures. Various materials and conversion mechanisms can transform this

vibrational energy into usable electrical power. As illustrated in Figure 15, these include piezoelectric, electromagnetic, and electrostatic generators. Piezoelectric transducers have garnered significant attention for harvesting power from vibration sources. This interest stems from their intrinsic electromechanical coupling properties and superior power density compared to their electromagnetic and electrostatic counterparts (121).

The capacity of piezoelectric materials to transform mechanical energy into electrical energy has been the subject of extensive research, establishing them as crucial elements in energy harvesting systems. These materials exhibit a distinctive characteristic: they produce an electric charge when exposed to mechanical stress or strain, a phenomenon referred to as the piezoelectric effect. A critical component of energy harvesting is the temporary storage of the collected energy for later use. This storage capability enables the utilization of harvested energy on demand, rather than necessitating immediate consumption. The effective use of captured energy heavily relies on incorporating energy storage solutions, such as capacitors or rechargeable batteries, into energy harvesting systems (122).



*Figure 15.* Various Applications of piezoelectric electrospun PVDF film (5)

Also, researchers have explored the use of piezoelectric materials to power wearable sensors and electronics. It becomes possible to capture the mechanical energy generated during everyday activities, such as walking, running, or simple gestures. The stretchable and conformable nature of electrospun PVDF-HFP nanofibers enables their use in flexible energy harvesting devices. These nanofibers can be integrated into wearable or implantable systems to scavenge mechanical energy from body movements, vibrations, or impacts. The nanofiber mats' flexibility and high surface area are advantageous for conformal integration with curved surfaces (105). Similarly, piezoelectric energy harvesting with wearable devices holds significant promise in addressing battery life challenges and sustainability. As piezoelectric energy harvesting continues to evolve, researchers are exploring innovative ways to integrate this technology into various applications, from medical implants to wearable devices. The potential to harness the

energy generated by human movements and environmental vibrations opens up new possibilities for developing self-powered, sustainable, and long-lasting electronic systems (122).

## Chapter 3

### Characterization and Experimental Methods

#### 3.1 Introduction

Poly(vinylidene fluoride-co-hexafluoropropylene), commonly known as PVDF-HFP, is a copolymer that has several desirable characteristics, including high hydrophobicity, robust mechanical properties, and ease of processing. To dissolve PVDF-HFP, researchers frequently employ N, N-dimethylformamide (DMF), and acetone as solvents. For this particular study, a commercially available PVDF-HFP was utilized. DMF, classified as a polar aprotic solvent, has the capacity to dissolve a broad spectrum of both polar and nonpolar substances. Acetone, on the other hand, is a polar solvent that readily mixes with water and numerous organic solvents. The combination of DMF and acetone in different ratios can control the viscosity and spinnability of PVDF-HFP solutions. The automated track system, roll-to-roll collector, and yarn spinning process are used to fabricate PVDF-HFP nanofibers and yarns. These methods allow for the production of continuous and uniform nanofibers and yarns with controlled morphology and properties. Mechanical testing, scanning electron microscopy (SEM), brightfield microscopy, and Fourier transform infrared spectroscopy (FTIR) are commonly used characterization techniques for PVDF-HFP nanofibers and yarns. These techniques provide information about the materials' mechanical properties, morphology, chemical composition, and crystalline structure. The mechanical-electrical system setup is used to study the piezoelectric and pyroelectric properties of PVDF-HFP nanofibers and yarns. This setup allows for applying stretch and flick deformations to the materials while measuring the generated electrical signals, providing insights into their energy harvesting.

## 3.2 Materials and Solvents

### 3.2.1 Polyvinylidene fluoride-co-hexafluoropropylene (PVDF-HFP) Polymer

PVDF-HFP (polyvinylidene fluoride-co-hexafluoropropylene) is a copolymer that dissolves in polar solvents like DMF (dimethylformamide) and acetone due to their close Hansen solubility parameters, indicating good mutual solubility. As the acetone content in the solvent mixture increases, the viscosity of the polymer solution decreases, but the solution behavior deteriorates at higher polymer concentrations, making viscosity measurement challenging. Researchers used the Teas diagram and Hansen space to visualize the locations of PVDF-HFP and the solvent mixtures, revealing that as the acetone content increased, the solvent mixture moved further away from the PVDF-HFP location in the Hansen space as shown in Figure 16. This suggests that pure DMF is the best solvent for PVDF-HFP among the mixtures studied, as it has the closest Hansen solubility parameters to the copolymer (46,123–125).

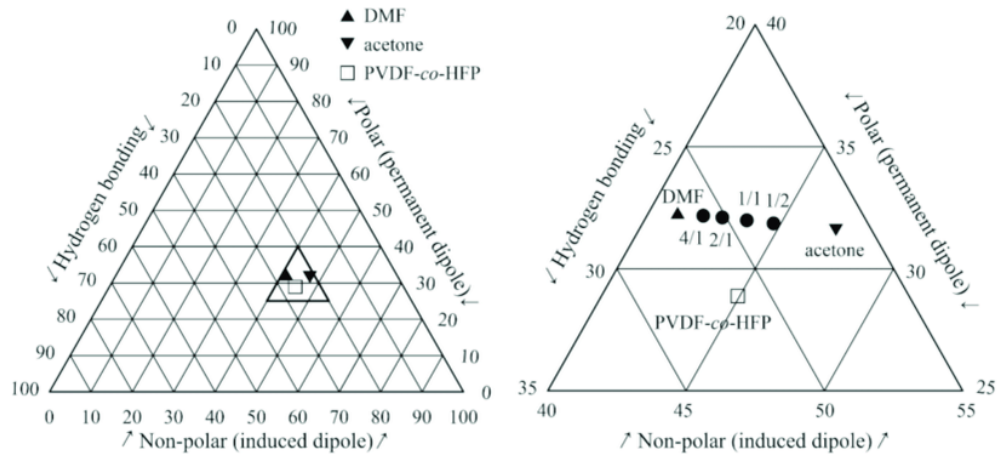


Figure 16. Visualizing the solubility of PVDF-HFP in DMF and acetone mixtures using teas diagrams. (125).

The process of electrospinning PVDF-HFP solutions using various DMF/acetone ratios resulted in nanofibers with diverse morphological characteristics. As the proportion of DMF increased, the fibers became more uniform and exhibited fewer beads. A correlation was observed between higher DMF concentrations and decreased average fiber diameter. Both the polymer concentration and the composition of the solvent were found to have significant effects on the solution's viscosity and the resulting morphology of the electrospun nanofibers. This research involved a methodical examination to elucidate how solvent composition and polymer concentration influenced the morphology and diameter of PVDF-HFP nanofibers produced through electrospinning (125).

### ***3.2.2 N, N-dimethylformamide (DMF)***

DMF (N, N-dimethylformamide) is an organic or dipolar aprotic solvent that effectively dissolves PVDF-HFP (polyvinylidene fluoride-co-hexafluoropropylene) polymer. A typical procedure is to add PVDF-HFP to DMF at a ratio of around 1 g of polymer per 10 mL of solvent, resulting in a ten wt.% solution. However, adding a small amount of acetone to the DMF solvent can enhance the formation of the electroactive  $\beta$ -phase in PVDF-HFP. From research, a DMF/acetone solvent ratio in the range of 4/6 to 7/3 was found to be suitable for creating uniform PVDF-HFP fibers with a high content of the  $\beta$ -phase, which is desirable for piezoelectric applications. The choice of solvent system and its ratio affects the thermodynamic properties of the PVDF-HFP solution, the processing techniques that can be used, and the final physicochemical characteristics of the processed material. Common solvents for PVDF and its copolymers include DMF, DMA (N, N-

dimethyl acetamide), NMP (N-methyl-2-pyrrolidone), MEK (methyl ethyl ketone), THF (tetrahydrofuran), and DMSO (dimethyl sulfoxide) (5,126–128).

### ***3.2.3 Acetone***

Acetone is a colorless, volatile, flammable liquid with a characteristic pungent odor. Acetone alone cannot dissolve PVDF-HFP polymer, but it can be combined with other solvents like DMF to dissolve PVDF-HFP. The addition of acetone to DMF affects the morphology and crystal structure of the resulting PVDF-HFP fibers. The presence of acetone in the solvent system enhances the formation of the  $\beta$ -phase in PVDF-HFP. However, an excess amount of acetone can decrease the fraction of the  $\beta$ -phase because the solution is subjected to less elongation during processing. In summary, while acetone alone cannot dissolve PVDF-HFP, it can be combined with DMF as a binary solvent system to dissolve the polymer and influence its crystal structure. The optimal ratio of DMF to acetone ranges from 4/6 to 7/3 to obtain uniform PVDF-HFP fibers with a high  $\beta$ -phase content (5,128).

### ***3.2.4 Electric Paint***

Electric paint is a conductive coating that can enhance the sensitivity of piezoelectric testing. It is composed of tiny piezoelectric particles dispersed in a thin polymer matrix. Electric paint can be used as an amplifier for piezoelectric testing by coating it on the surface of a piezoelectric material. The electric paint, a conductive coating, helps distribute the electric field more uniformly across the piezoelectric material,

enhancing the sensitivity of the testing. When a piezoelectric material is subjected to mechanical stress, it generates an electric charge. Coating the surface with electric paint allows the generated charge to be more effectively collected and measured, allowing for more accurate piezoelectric testing. The use of electric paint as an amplifier for piezoelectric testing is particularly useful when dealing with small or thin piezoelectric samples, where the generated charge may be too weak to be detected without amplification (129,130).

### **3.3 Sample Preparation Method**

PVDF-HFP copolymer pellets with a molecular weight of 400,000 and the organic solvents N, N-dimethylformamide (DMF), and acetone were purchased from (Sigma-Aldrich and Fisher Scientific), respectively. As shown in Figure 17, to prepare a 30% w/v PVDF-HFP solution, 5.4 g of PVDF-HFP pellets were dissolved in a 2:1 ratio of DMF and acetone. This mixture was placed on a heated shaker at 65°C for 24 hours to ensure complete dissolution of the pellets. After 24 hours, a viscous, homogeneous solution was obtained at room temperature. Proper dissolution of the PVDF-HFP copolymer in the solvent mixture is crucial for obtaining a uniform solution suitable for electrospinning nanofibers.

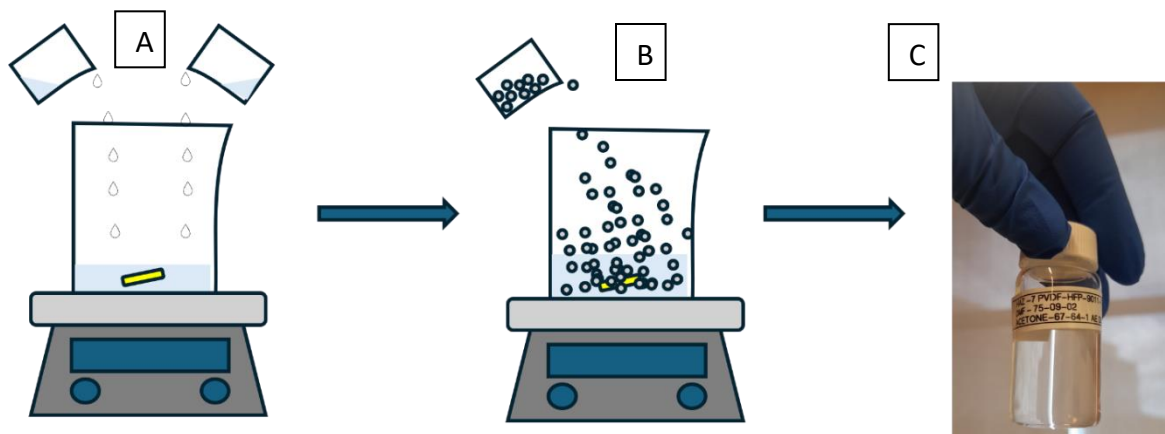


*Figure 17.* Schematics Flowchart Process of **(A)** DMF and Acetone solvents are poured into a beaker containing a yellow magnetic stirrer on a hot plate at 65°C. **(B)** measured PVDF-HFP pellets are poured into the solvent mixture, stirring at 250 rpm for 24 hrs. **(C)** Homogenous PVDF-HFP solution.

### ***3.3.1 Electrospinning of PVDF-HFP Nanofibers***

Electrospinning uses polymer solutions and an electric field to produce nanofibers. For this research study, electrospinning was carried out with a 9KV applied voltage via a power supply ES40P-10W (Gamma High Voltage Research Inc) to a 21-gauge blunt capillary needle at a 10cm height distance above the top of an automated track system. A syringe pump (New Era Pump systems) expelled the solution at a constant rate of 1ml/hr. The electrospinning process was done in a controlled acrylic fume hood container. Samples were collected within an observed temperature and humidity range of 70°F to 75°F and 50-60%, respectively.

### 3.3.2 Principle of the Post-Drawing Process

The principle of the post-drawing process from Figure 18 with an electrospun polymer nanofiber like PVDF-HFP involves applying a tensile force to elongate or stretch the nanofibers after they are initially electrospun. This post-drawing step induces molecular orientation and crystallinity changes that significantly improve the mechanical properties of the nanofibers. During electrospinning, the polymer chains within the nanofibers are initially frozen in a kinked and disordered state due to the rapid solvent evaporation. The post-drawing process applies a tensile force to elongate these as-spun nanofibers, causing the polymer chains to straighten out and align along the fiber axis. This molecular orientation disrupts the initial crystalline structures formed during electrospinning and leads to the formation of new, highly oriented crystalline domains along the fiber direction.

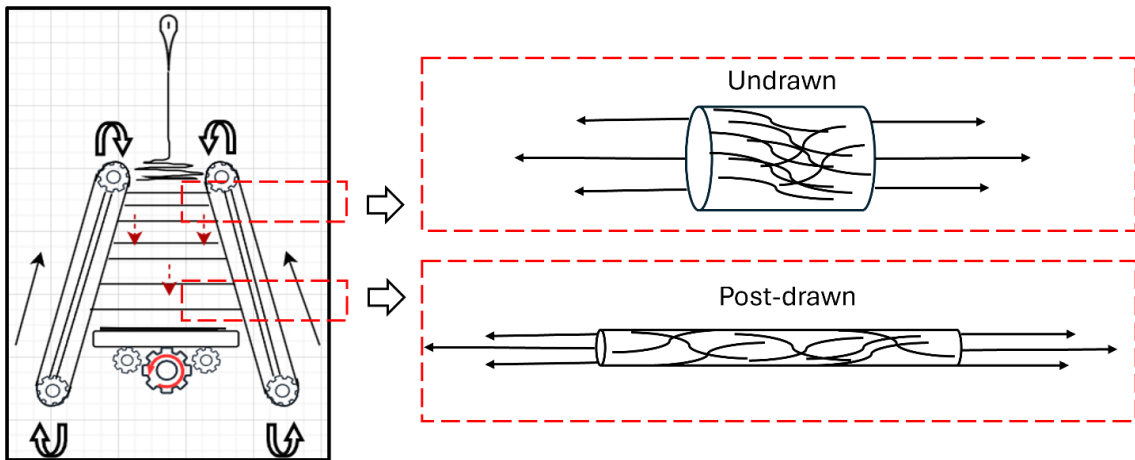


*Figure 18.* illustrates the automated-track system for facilitating the continuous collection of polyvinylidene fluoride-co-hexafluoropropylene (PVDF-HFP) nanofibers. The top gap represents the undrawn nanofibers, while the bottom gap shows the post-drawn nanofibers. As the nanofibers are lengthened during the drawing process, their diameter decreases due to the alignment and extension of the polymer chains. This process is expected to result in a higher prevalence of organized polymer chains, leading to stronger and more aligned nanofibers.

Post-drawing of electrospun nanofibers is achieved using automated track systems as it applies a controlled tensile force to elongate the fibers immediately after electrospinning. This allows the post-drawing process to be integrated with electrospinning in a continuous manufacturing approach. Achieving high draw ratios is crucial for maximizing the mechanical performance benefits from post-drawing. The ability to post-draw electrospun nanofibers is particularly important as it enables producing polymer nanofibers with mechanical properties that match or even exceed those obtained through conventional fiber spinning methods. This makes post-drawn electrospun nanofibers attractive for this research work in obtaining high mechanical performance combined with the high surface area and other unique advantages offered by the nanoscale fibrous structure (131–133).

### ***3.3.3 Automated Parallel Track System***

An automated parallel track system as shown in Figure 19 and Figure 20 was built in-house to achieve the stretching and post-drawing process for the electrospun PVDF-HFP nanofibers. It is an adjustable system that can be angled to enable the function of stretching fibers as the solvent fully evaporates and nanofibers fully solidify; they travel down parallel aluminum conveyor belts powered by a 12V stepper motor and deposit on a roll-to-roll collector for yarn manufacturing. Also, fiber controls were collected using a static rack. This assembly system was angled at different length gap ratios by varying the top and bottom of the tracks to give a draw ratio of 1:1, 1:2, and 1:3, which have dimensions of 12 cm-12 cm, 6 cm-12 cm, and 4 cm-12 cm, respectively. The (DR= Bottom fiber length/Top fiber length). Five samples (n=5) were collected for DR1 (Undrawn), DR2, and DR3.

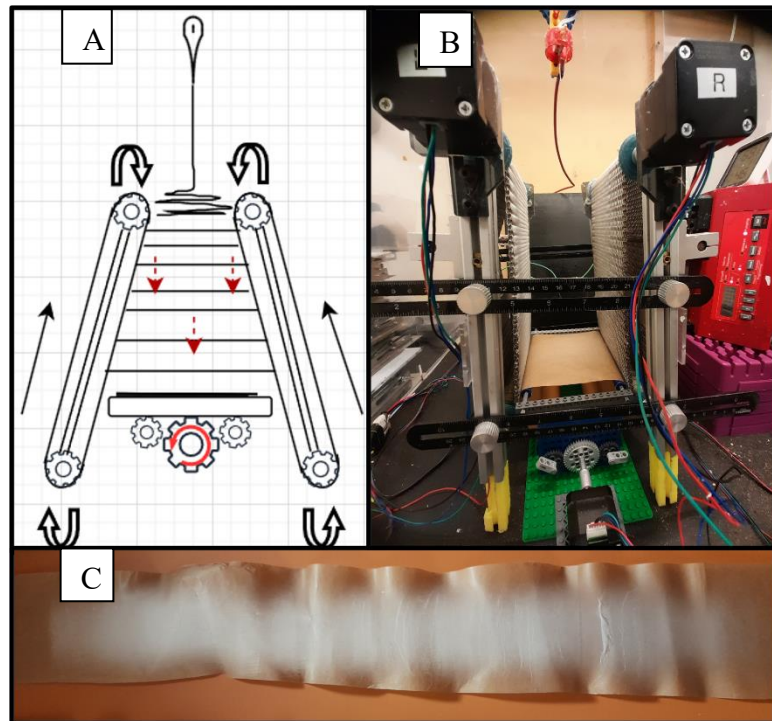


*Figure 19. (A) Schematics of the variable draw ratio electrospinning system modified to collect controls of each sample (B) Electrospinning system setup with the roll-to-roll collector (C) Parchment paper containing a sample of electrospun PVDF-HFP nanofibers.*

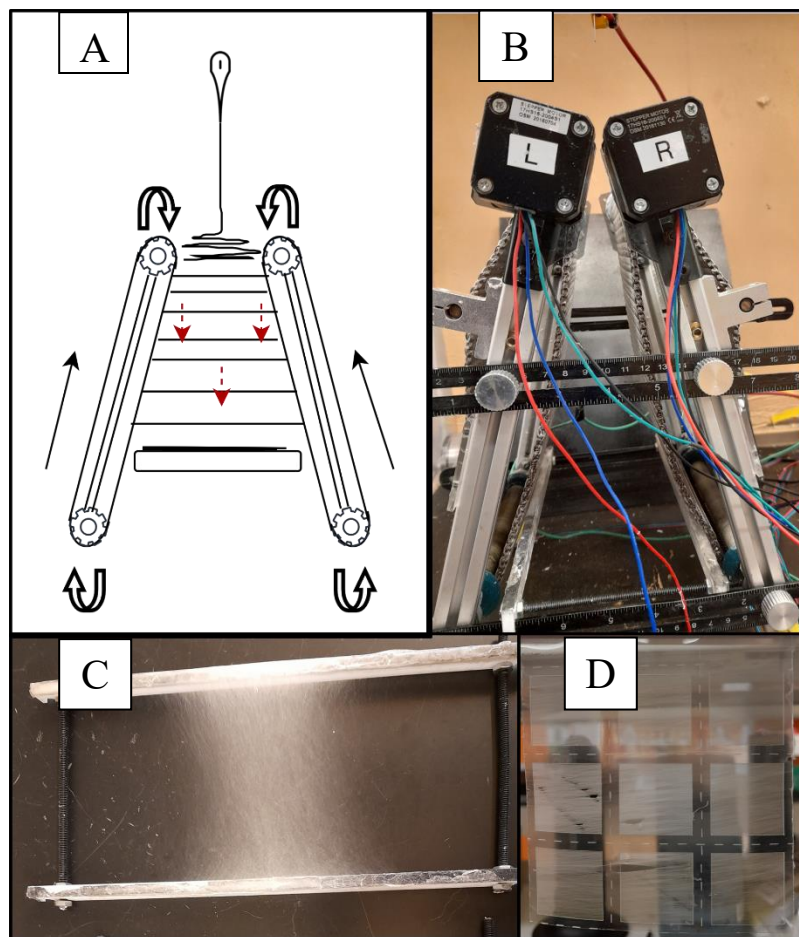


*Figure 20. (A) Schematics of the variable draw ratio electrospinning system modified to collect controls of each sample (B) Electrospinning system setup (C) Tray Collector containing electrospun PVDF-HFP nanofibers (D) 10mm by 10mm plastic window frame containing an electrospun PVDF-HFP sample.*

### **3.3.4 Roll to Roll Collector**

The roll-to-roll collector in Figure 21 is an adjustable continuous collector that works with the automated parallel track system during electrospinning. The electrospun PVDF-HFP nanofibers are deposited on the parchment paper rolled onto this collector. The step motor rotates the center gear, rotating the bottom rollers at the same speed to allow for a continuous collection of electrospun fibers. This collector can be extended up to a width of 19cm.

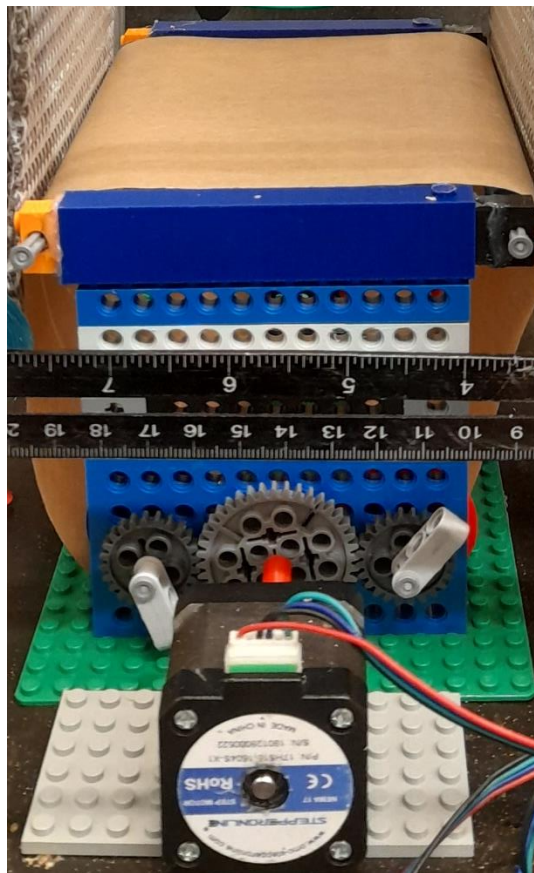


*Figure 21.* Modifiable roll-to-roll collector allowing collection of electrospun nanofibers as they travel down the automated tracks.

### ***3.3.5 Yarn Spinning Process***

The novelty and impact of this research study lie in the innovative twist-and-roll process used for manufacturing nanofiber yarns from electrospun nanofiber webs. This process represents a significant advancement in nanofiber yarn production, offering precise control and optimization of the yarn properties. From Figure 22, the twist-and-roll process begins by securing the edges of the nanofiber web in a fiber grip connected to a moving motor. The nanofibers are pulled from the web and aligned under the resulting tension as

the motor moves. This alignment step is crucial for ensuring the uniformity and strength of the final nanofiber yarn. The aligned nanofibers are twisted into a nanofiber yarn, with the twist per inch (TPI) being a critical parameter. In this study, the twisting speed was fixed at 30 rpm (1 twist/s), and the TPI was inversely proportional to the translational speed, allowing for precise control over the yarn properties. During the manufacturing process, a unique geometric configuration is formed. A triangle is created between the web and the yarn, with the base being the width of the nanofiber web and the vertex being the point where the nanofiber yarn is formed. As the spinning device moves in a circular and rotational direction simultaneously, the nanofibers are pulled out from the base, and the nanofiber yarn is spun at the vertex with a constant triangle height. This geometric configuration plays a crucial role in determining the yarn's characteristics, such as strength, uniformity, and alignment (134).

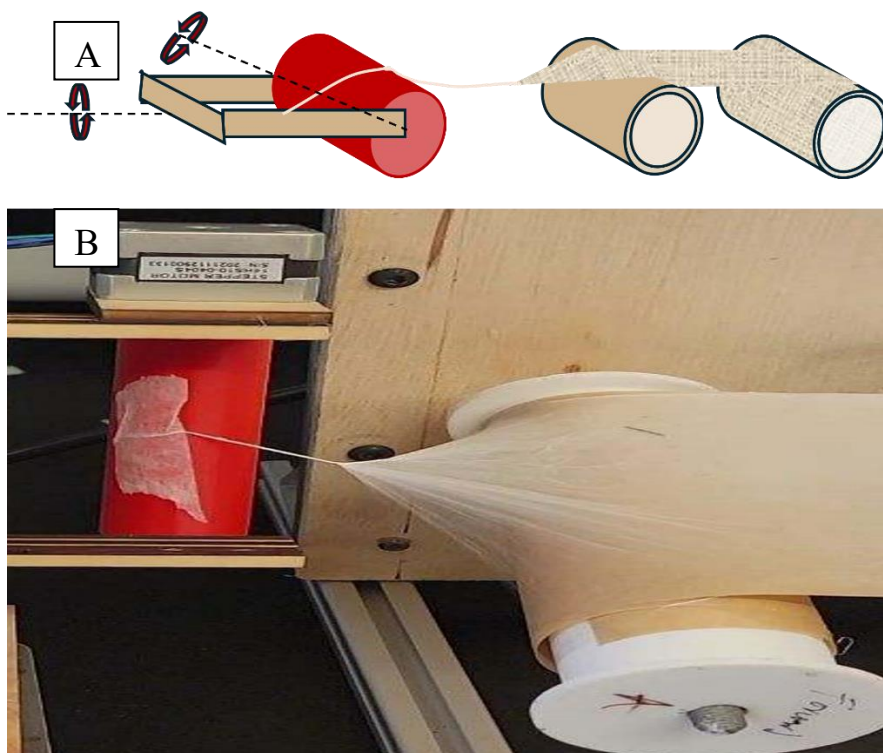


*Figure 22. (A) Schematics diagram of the yarn spinning method. (B) Pictorial representation of the yarn-spinning method.*

### **3.4 Mechanical Testing**

The mechanical properties of nanofiber yarns were investigated using a single-strand method. The testing was conducted on a universal testing machine with grips that had frictionless loops to hold the fixed yarns. A 100N load cell was utilized for the tensile tests, performed at a strain rate of 10 mm/min and a gauge length of 10 mm. All test conditions adhered to the standards set by ASTM D2256 (134). The single-strand yarn tensile test determines the breaking force, elongation, and toughness properties of a yarn material. This information is crucial for evaluating and comparing different yarn materials' strength and performance characteristics.

Tensile testing was conducted on fiber samples collected on plastic window frames to determine their ultimate tensile strength and Young's modulus. A 2 Newton load cell was used, and the tests were performed at a 4.5 mm/min rate until the samples failed. The plastic frames were loaded into the tensile test clamps, and the sides of the frames were cut to ensure that the load was solely concentrated on the fibers and not the frame, allowing the calculation of Young's modulus from the initial linear region of the stress-strain curve (133).

The average cross-sectional area of each sample was calculated by multiplying the total number of fibers by the average individual fiber cross-sectional area, which was determined using a formula involving the average fiber diameter. The stress and strain values were calculated by dividing the force and displacement values by the total cross-sectional area and initial window frame length. The yield stress was identified as the point where the stress-strain curve transitioned from the linear to the nonlinear or plastic region (133). Figure 23 indicates the key points in a stress-strain curve.

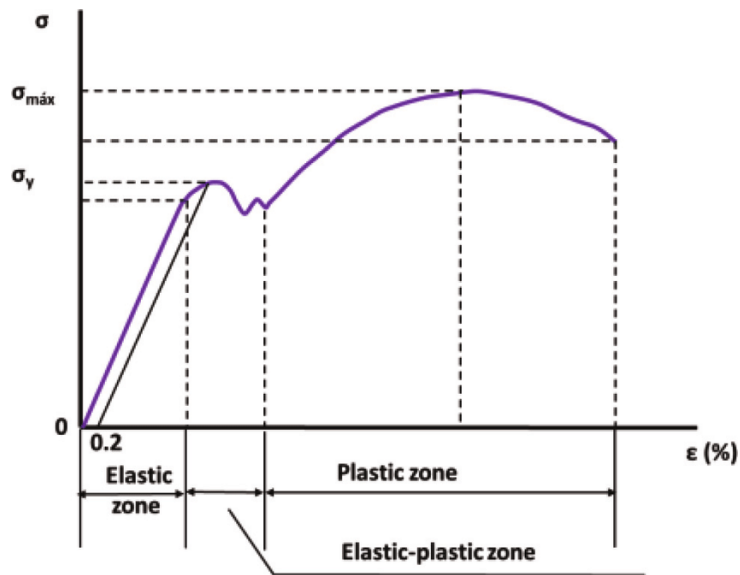


Figure 23. A typical stress-strain curve (135)

The yield stress is the point on the stress-strain curve where the material transitions from elastic to plastic deformation. It is the stress at which the material starts to deform permanently. This can be seen as where the stress-strain curve deviates from linearity. The ultimate tensile strength is the maximum stress the material can withstand before fracturing. It is the highest point on the stress-strain curve. The ultimate tensile strength is the maximum stress the material can withstand before fracturing. It is the highest point on the stress-strain curve. The elongation at break is the strain (change in length divided by the original length) at which the material fractures. It is the maximum strain value on the stress-strain curve. Specific strength is the ultimate tensile strength divided by the yarn's linear density. This gives a measure of the material's strength-to-weight ratio.

The single-strand yarn tensile test with an example shown in Figure 24, is a critical quality control and material development tool that provides essential mechanical property data to support the manufacturing of reliable, high-quality textile products. The test results enable

informed material selection and design decisions. Adhering to these established standards ensures consistent, reproducible results that can be compared.



*Figure 24.* Tensile test of an electrospun PVDF-HFP nanofiber yarn using the universal testing System

### **3.5 Scanning Electron Microscopy (SEM)**

Scanning Electron Microscopy (SEM) is a crucial imaging technique used extensively in research across various fields. SEM imaging analysis involves carefully preparing samples, selecting appropriate imaging modes (such as secondary electron, backscattered electron, or energy-dispersive X-ray spectroscopy), and optimizing instrument settings to capture high-resolution, informative images (136). Researchers then apply image processing techniques to enhance the clarity and interpretability of the SEM data, which can be used for both qualitative and quantitative analysis. This includes measuring dimensional features, identifying material phases, and estimating properties like

porosity and surface area. This study examined the PVDF-HFP nanofiber yarn samples using the SEM (Phenom Pure). The samples were prepared carefully and placed on aluminum stubs covered with carbon black tape. All samples were sputter-coated before imaging. Three images were taken at different magnifications to determine the fiber density, fiber diameter, and yarn diameter (136–138).

### **3.6 Brightfield Microscope**

A brightfield microscope is a common and widely used type of light microscope in biology, cellular biology, and microbiology. It uses a simple and reliable method to illuminate a sample and create an image. In a brightfield microscope, the sample is placed on a glass slide and illuminated by a light source. The light passes through the sample, and an objective lens magnifies the image and projects it onto an eyepiece or camera. The sample appears dark against a bright background, hence the name "brightfield." The key components of a brightfield microscope include the eyepiece, objective lenses, focus knobs, stage, condenser lens, and light source. This study utilized this in taking images of the nanofibers for fiber count. Nanofibers were collected on a 10 mm × 10mm plastic window frame width. Using a measuring tool known as ImageJ, fibers can be counted within an orthogonal distance of 100  $\mu\text{m}$ . The estimated value obtained is multiplied by the width of the frame, which is 100.

### 3.7 Fourier Transform Infrared Spectroscopy (FTIR)

Fourier Transform Infrared Spectroscopy (FTIR) is a powerful analytical technique used to identify and analyze the chemical composition of various materials, including organic compounds, polymers, and inorganic substances. FTIR works by passing infrared radiation through a sample, which causes the chemical bonds in the sample to vibrate at specific frequencies. These vibrations are characteristic of the sample's molecular structure and functional groups, creating a unique spectrum. FTIR uses an interferometer to encode all the infrared frequencies into a single signal, decoded using a Fourier transform algorithm.

Polarized Fourier Transform Infrared Spectroscopy (FTIR) differs from nonpolarized FTIR in how it accesses molecular alignment in materials. Polarized FTIR involves analyzing absorbances with light (infrared light) in specific directions, allowing for evaluating molecular order in the sample. In contrast, nonpolarized FTIR does not consider the direction or alignment of molecules and provides somewhat of a more general analysis of the chemical absorbances of chemical absorbances in a material.

The Thermo Nicolet Nexus 670 FTIR spectrometer was used to obtain information about the chemical absorbances of the samples. This enabled the calculation of the  $\beta$ -phase (non-polarized FTIR) and polymer chain alignment (polarized FTIR) characteristics of the materials. The spectra were acquired using polarized light, with measurements taken in both the parallel and perpendicular directions relative to the direction in which the fibers were post-drawn. The OMNIC Software tool established the baseline for the wavelength and absorbance at an observed spectra region between 400 and 4000  $\text{cm}^{-1}$ . Characteristic peaks associated with the  $\alpha$ -phase of PVDF were examined at 613  $\text{cm}^{-1}$ , 761  $\text{cm}^{-1}$ , and

1189  $\text{cm}^{-1}$ , while characteristic absorption peaks for the  $\beta$ -phase were examined at 841  $\text{cm}^{-1}$ , 881  $\text{cm}^{-1}$ , 1072  $\text{cm}^{-1}$ , 1280  $\text{cm}^{-1}$ , and 1400  $\text{cm}^{-1}$  (133).

$$F(\beta) = \frac{X\beta}{X\alpha + X\beta} = \frac{A\beta}{\left(\frac{K\alpha}{K\beta}\right)A\alpha + X\beta} = \frac{A\beta}{1.26A\alpha + A\beta} \quad (3)$$

Where  $X\alpha$  is the crystal mass fraction of the  $\alpha$  phase, and  $X\beta$  is the crystal mass fraction of the  $\beta$  phase.  $A\alpha$  and  $A\beta$  are the absorbance band intensity, and  $K$  is the absorption coefficient of each phase. The equation above is also known as the Lambert-Beer law equation, which can be used to calculate the associated piezoelectric  $\beta$ -phase content.

The Dichroic Ratio is used to assess the polymer chain alignment based on the absorbances in the parallel and perpendicular directions of the polarized FTIR Spectra.

$$DR = \frac{A_{\perp} - A_{\parallel}}{A_{\perp} + A_{\parallel}} \quad (4)$$

Where  $DR$  is the Dichroic ratio and  $A_{\perp}$  and  $A_{\parallel}$  are absorbances measured in the perpendicular and parallel direction, respectively (134).

### 3.8 Mechanical-Electrical Experimental System Setup

As shown in Figure 25, manufactured PVDF-HFP yarns are amplified using electric paint and jumper wires to help distribute the electric field more uniformly across the yarn sample, enhancing the testing sensitivity. It can be subjected to mechanical stress, generating an electric charge. A length of at least 10 cm was measured for each sample used.

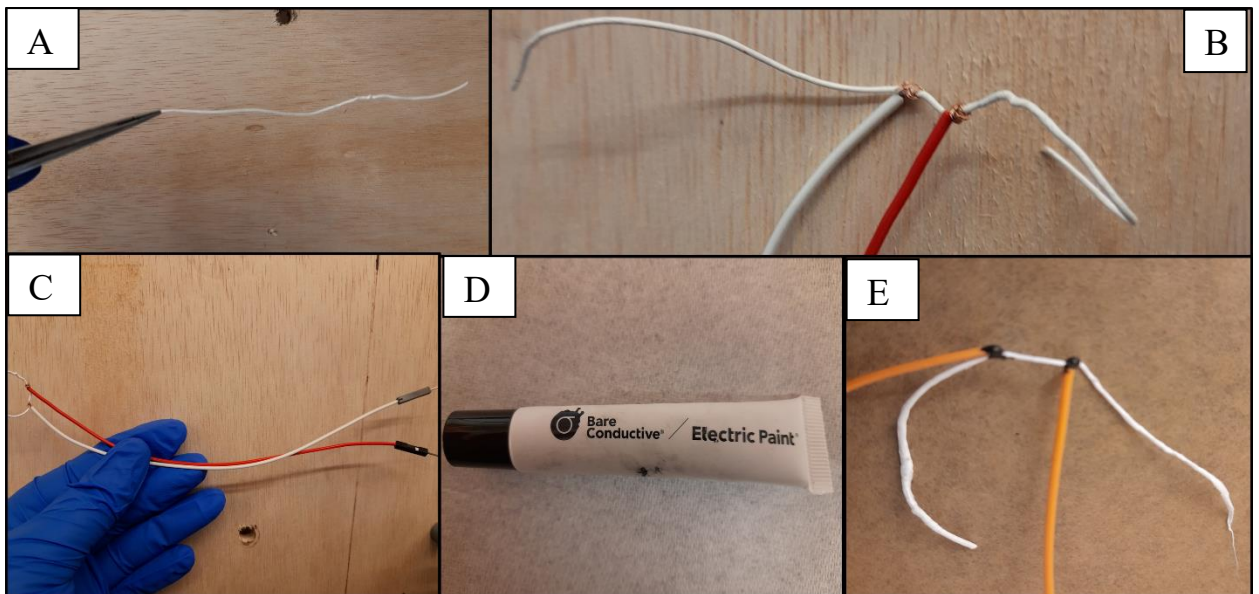


*Figure 25.* (A) 10 cm measured PVDF-HFP yarn sample (B) A pair of jumper wires ends attached to a yarn sample (C) Complete view of a pair of jumper wires attached to a yarn sample at two points with a distance of 1 cm (D) Electric Paint (Bare Conductive) (E) Prepared PVDF-HFP yarn sample for electrical testing.

The NI USB-6000, shown in Figure 26, is a low-cost, multifunction data acquisition (DAQ) device that offers a versatile and portable solution for various measurement and automation applications. This USB-based device provides analog input and output channels, digital I/O lines, and counter/timer functionality, making it suitable for a wide

range of applications such as data logging, sensor monitoring, and control systems. The NI-DAQmx is a software interface that seamlessly integrates with the NI USB-6000, enabling the configure, acquire, and analyze data with ease. This software provides a comprehensive set of programming tools and libraries, supporting multiple programming languages and environments, including LabVIEW, C/C++, and .NET. With its plug-and-play connectivity, the NI USB-6000, combined with the NI-DAQmx software, offers a cost-effective and flexible solution for this research work.



*Figure 26.* National Instrument (NI) USB-6000 multifunction data acquisition (DAQ) device

### ***3.8.1 Stretch Deformation***

A stretching deformation was implemented to obtain the piezoelectric response of the PVDF-HFP yarn shown in Figure 27. The yarn was subjected to a rotational vibration generated by a programmable motion controller ( Class 6 D-style SmartMotor™) at 93 rpm. The mechanical stimulation frequency range is (7 – 11) Hz. An electric paint (Bare Conductive) was applied to the yarn to amplify the electrical signal, and it was tightly coiled up with jump wires. The yarn was fixed at one end, and the other end was attached perpendicular to the rotating motor shaft and secured with zip ties to ensure a stable grip. During the testing, the rotational vibration from the programmable motion controller stretched the PVDF-HFP yarn at the specified rotational speed and angular displacement of 36°. Also, it can be inferred that a higher rpm would correspond to a higher frequency of the applied mechanical stress. Therefore, based on the information provided, one can hypothesize that the voltage output from a piezoelectric polymer nanomaterial would increase with increasing the applied mechanical stress or vibration RPM. This study research shows that for PVDF/BNNT nanocomposite, the voltage output increased from 49.24 mV at 20 Hz to 62.68 mV at 50 Hz when subjected to longitudinal forces. Another study mentions that as the shaking frequency increases from 19 Hz to 26 Hz, the device with optimized ZnO nanorod length produces an increasing output voltage (139,140).

This test was carried out for each draw ratio ( $n = 5$ ) and fiber density ( $n = 5$ ), with each test lasting 30 seconds. I hypothesize that higher draw ratios and densities in electrospun nanofiber yarns will increase the voltage generation capability for this flick deformation test. A data acquisition (DAQ) system, specifically the NI (National Instruments) system, was used to capture and collect the generated electrical signals. A

visual measurement program (LabView) developed in DAQ Express was utilized to acquire and analyze the output electrical signals from the device, which were displayed on a computer interface. The collected data provided insights into the yarn's piezoelectric performance, particularly the peak-to-peak voltage.

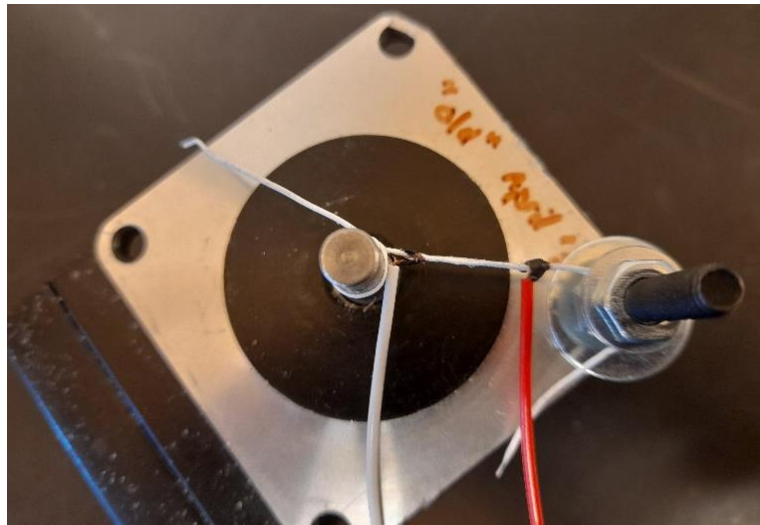


*Figure 27.* Stretch deformation test on an electrospun PVDF-HFP nano yarn sample using a programmable motion controller

### ***3.8.2 Flick Deformation***

This experiment used a 6-blade flexi-plastic rotating wheel attached to a DC motor to create a flick deformation effect shown in Figure 28. The wheel rotated at a speed of 93 rpm for all samples to ensure consistency in the data obtained. The mechanical stimulation frequency range is 7 - 11 Hz. An electric paint was applied to the yarn to maximize the electrical signal, and the yarn was tightly coiled up with jump wires. The yarn was locked at both ends with a glued plastic piece within a distance of 2cm to ensure a stable grip. The

rotating wheel was positioned during the testing, so the blades hit the yarn right in the middle between the probed nodes.

This test was carried out for each draw ratio ( $n = 5$ ) and fiber density ( $n = 5$ ), with each test lasting 30 seconds. A Data Acquisition (DAQ) system, specifically the NI (National Instruments) system, was used to capture and collect the generated electrical signals. A visual measurement program (LabView) developed in DAQ Express was utilized to acquire and analyze the output electrical signals from the device, which were displayed on a computer interface. The collected data provided insights into the piezoelectric performance of the yarn via this deformation method to obtain the peak-to-peak voltage.

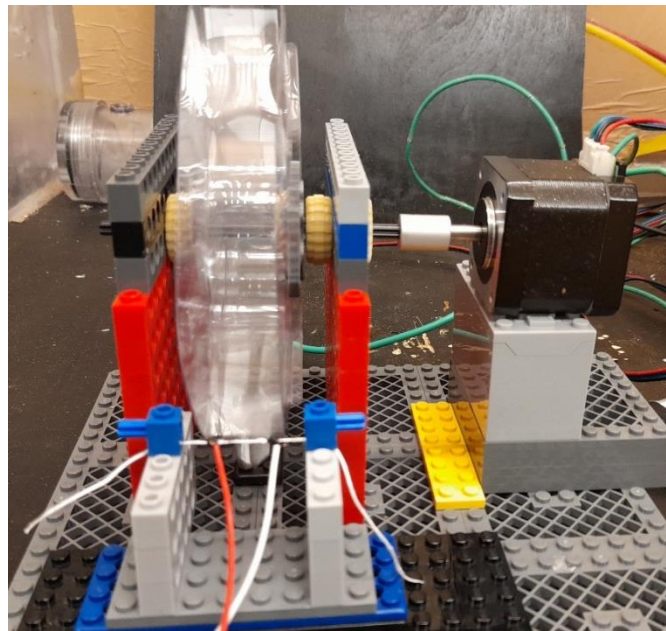


*Figure 28.* Flick deformation test on an electrospun PVDF-HFP nanoyarn sample using a rotating wheel powered by a 12 V DC motor.

Piezoelectric materials like PVDF-HFP nanoyarns exhibit a coupling effect between their mechanical and electrical behaviors. When subjected to mechanical stress or vibrations, they generate an electrical voltage output proportional to the applied force. Likewise, in the stretch deformation test, it can be inferred that a higher rpm would correspond to a higher frequency of the applied mechanical stress cycles. Consequently, a similar trend is expected in the flick deformation test, where higher flick frequencies would result in higher voltage outputs from the nanoyarn piezoelectric material. This frequency-dependent behavior highlights the potential of PVDF-HFP nanoyarns for applications in smart textiles and energy harvesting devices.

## **Chapter 4**

### **Result and Discussion**

#### **4.1 Introduction**

Tensile analysis, morphology analysis, FTIR spectroscopy, and mechanical-electrical testing are complementary techniques to characterize materials' physical and functional properties. Tensile testing provides critical data on a material's strength and flexibility, while morphology analysis examines its surface features and microstructure using advanced microscopy. FTIR spectroscopy identifies the crystalline phases of poly(vinylidene fluoride) (PVDF) based on the characteristic absorption peaks, providing a unique "fingerprint" spectrum. Mechanical-electrical testing combines mechanical loading with electrical measurements to characterize the electromechanical properties of smart materials and devices.

#### **4.2 Tensile Analysis**

The specific strength of PVDF-HFP nanoyarn, as illustrated in Figure 29 and Figure 30, shows a notable increase with higher draw ratios (DR). Specifically, the specific strength values are 34,900 Nm/kg for LDR1, 39,700 Nm/kg for LDR2 (a 13.8% increase from LDR1), and 48,500 Nm/kg for LDR3 (a 22.1% increase from LDR2 and 39.0% from LDR1). This significant enhancement in specific strength is promising for materials science and nanotechnology applications. Additionally, increasing the fiber density of the yarns, also increased their specific strength with a low density at 48,500 Nm/kg, a medium density at 54,500 Nm/kg (a 12.4% increase from a low density), and a high density at 86,000 Nm/kg (a 57.8% increase from medium density and 77.3% from low density).

These results obtained using an automated track electrospinning setup with an adjustable roll-to-roll collector, demonstrate better improved mechanical properties of the manufactured yarns.

The specific strength of the component PVDF-HFP nanofiber makes up the nanoyarns as shown in Figure 31. Their specific strength increased dramatically with increasing draw ratio, with LDR1 at 37600 Nm/kg, LDR2 at 87200 Nm/kg (a 132% increase compared to LDR1), and LDR3 at 106000 Nm/kg (a 21.4% increase compared to LDR2 and 181% compared to LDR1), indicating that the specific strength of the PVDF-HFP nanofiber yarn and control samples increased significantly with increasing draw ratio and fiber density, with the nanofiber control samples showing the most dramatic increases, with the LDR3 samples nearly 2.8 times stronger than the LDR1 samples.

The mechanical behavior of component nanofibers in Figure 32 shows an increasing trend for ultimate tensile stress, Young's modulus, and yield stress from LDR1 to LDR3. Ultimate tensile Stress increases from 85.9 MPa for LDR1 to 165 MPa for LDR2 (92% increase) and 203 MPa for LDR3 (23% increase from LDR2). Young's modulus rises from 253 MPa for LDR1 to 656 MPa for LDR2 (159% increase) and 911 MPa for LDR3 (39% increase from LDR2). Yield stress increases from 36.9 MPa for LDR1 to 104 MPa for LDR2 (182% increase) and 131 MPa for LDR3 (26% increase from LDR2). Also, this result does compare relatively to this research study's findings on electrospun PVDF- HFP nanofiber, where a 30% increase in ultimate tensile strength, from 250.6 MPa at DR1 to 325.1 MPa at DR3. A 53% increase in Young's modulus, from 0.96 GPa at DR1 to 1.47 GPa at DR3. A 141% increase in yield stress, from 78.4 MPa at DR1 to 189.1 MPa at DR3 (133). By comparing both studies, the ultimate tensile stress from LDR1 to DR1 (192%) is

significantly higher than the change from LDR3 to DR3 (60%). For Young's modulus, a 61% increase from LDR3 to DR3 is still a substantial increase but lower than the percentage increase observed from LDR1 to DR1. These results could be attributed to the fiber counts obtained from the different experimental or processing conditions.

The mechanical behavior of nanoyarns from this research manufacturing approach reveals in Figure 33 significant variations in the mechanical properties of the three samples, LDR1, LDR2, and LDR3. LDR1 had an ultimate tensile stress of 61.8 MPa, while LDR2 showed a 13.6% increase with a value of 70.2 MPa, and LDR3 exhibited a further 22.3% increase of 85.9 MPa. LDR1 had the lowest Young's modulus of 83.4 MPa, while LDR2 exhibited an 84.2% increase with a value of 154 MPa, and LDR3 showed a further 45.2% increase with 224 MPa. LDR1 had a yield stress of 11.0 MPa, while LDR2 showed a 12.7% increase with a value of 12.4 MPa, and LDR3 exhibited a further 8.8% increase with a value of 13.5 MPa. Yarn strength did not increase as much as their component fiber strength with draw ratio. I hypothesize that this is because the nanoyarns could fail by unraveling as opposed to tensile failure of the component fibers. Comparatively, this research study used a self-bundling electrospinning approach for producing PVDF-HFP nanoyarns, with obtained maximum average ultimate strength results at 60.4 MPa (141). This is a 2.32%, 16.23%, and 42.24% increase in ultimate tensile stress for LDR1, LDR2, and LDR3 respectively.

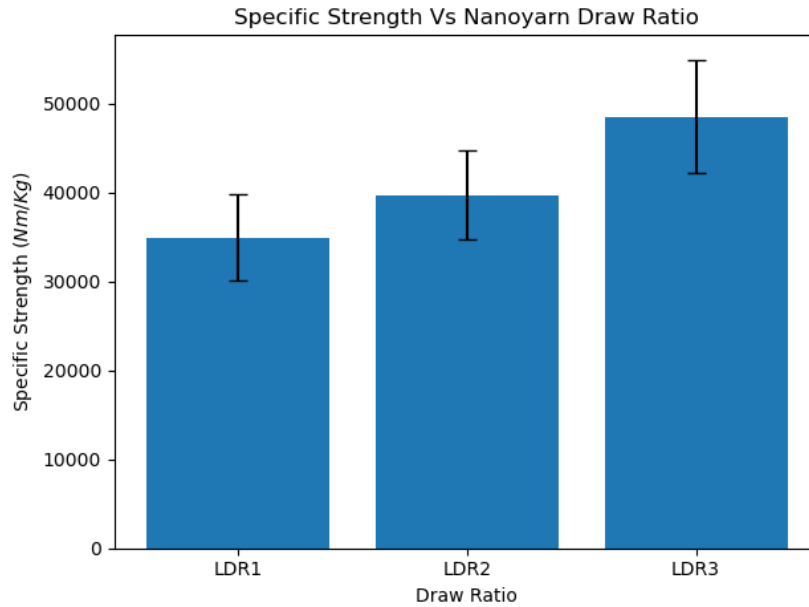


Figure 29. Specific strength of low density (LD) nanoyarn vs. component fiber draw ratio ( $n = 5$ ), ANOVA p-value  $< 0.01$ , all group-to-group comparisons student t-test give a p-value  $< 0.01$  for LDR1 vs LDR3 only.

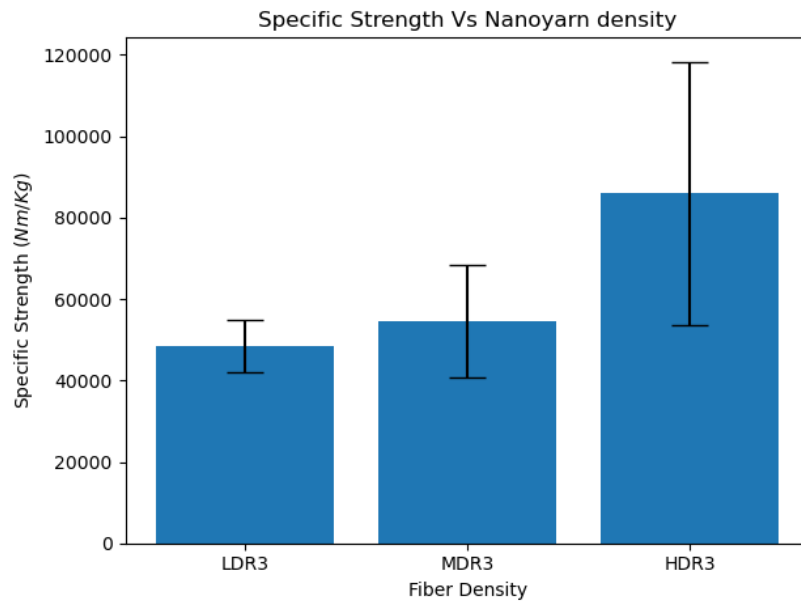
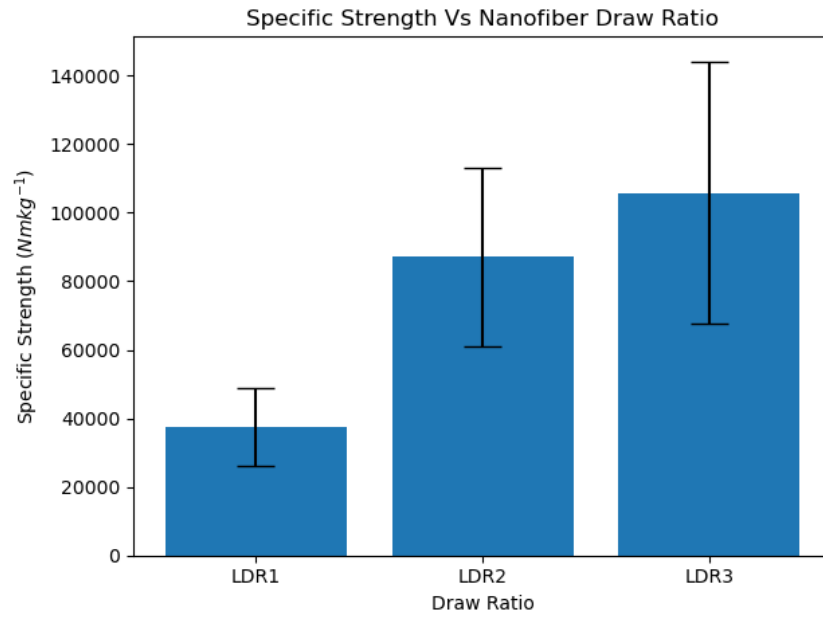
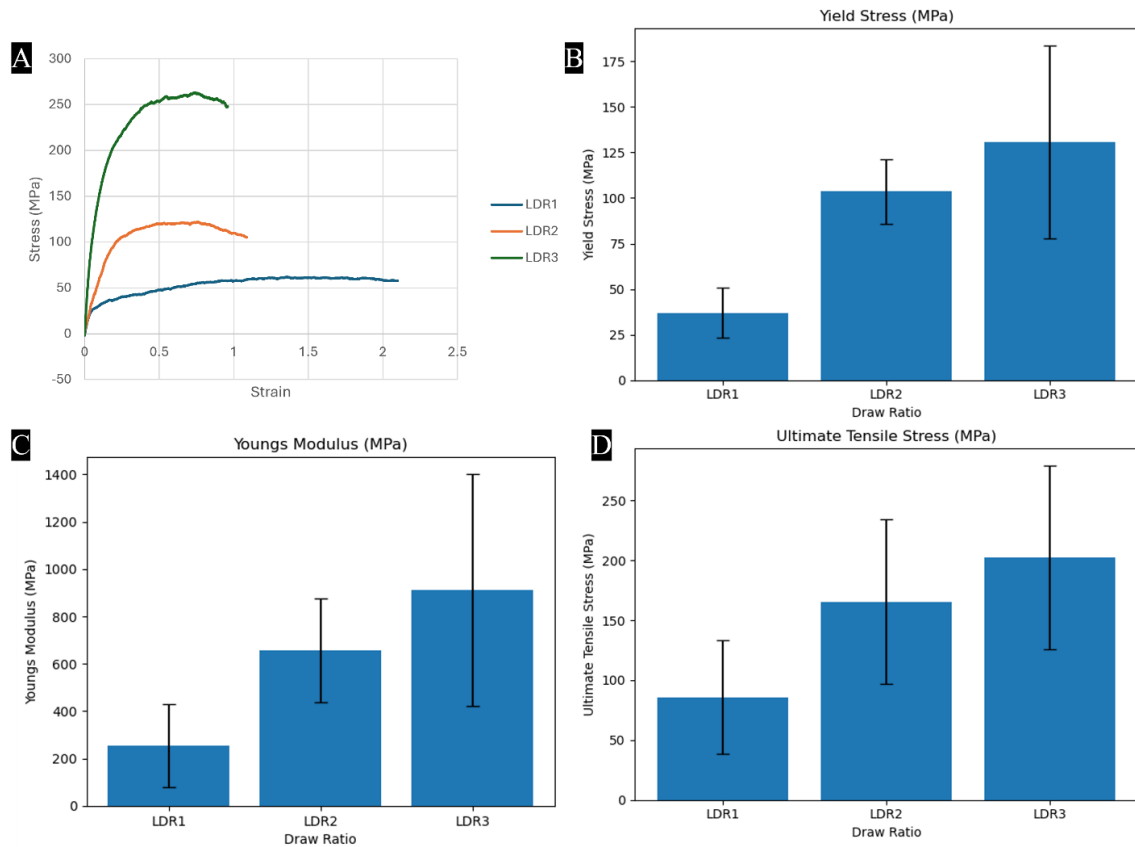


Figure 30. Specific strength of nanoyarns vs low (LD), medium (MD), and high (HD) density yarns, ANOVA p-value  $> 0.01$ , All were comprised of component fibers drawn to a draw ratio of three (DR3) ( $n = 5$ ), and all group-to-group comparisons with student t-test give a p-value  $> 0.01$ .



*Figure 31.* Specific strength of nanofibers vs draw ratio (n=5), ANOVA p-value = 0.01, group-to-group comparisons with student t-test have a p-value < 0.01, except for groups LDR2 vs LDR3.



**Figure 32.** Mechanical behavior of component nanofibers **(A)** presents stress-strain curves from one nanofiber sample for LDR1, LDR2, and LDR3. The curves are truncated after the ultimate tensile strength peak for better presentation. **(B)** Notably, there is a clear upward trend in the nanofiber yield stress from the LDR1 to LDR3, indicating a significant increase in strength, ANOVA p-value < 0.01, all group-to-group comparisons with student t-tests give a p-value < 0.01, except for groups DR2 vs DR3. **(C)** The Young's Moduli shows a continuous increase from LDR1 to LDR3, ANOVA p-value > 0.01, all group-to-group comparisons with student t-tests give a p-value > 0.01. **(D)** Ultimate tensile strength also shows a continuous increase from LDR1 to LDR3, ANOVA p-value > 0.01, and all group-to-group comparisons with student t-tests give a p-value > 0.01.

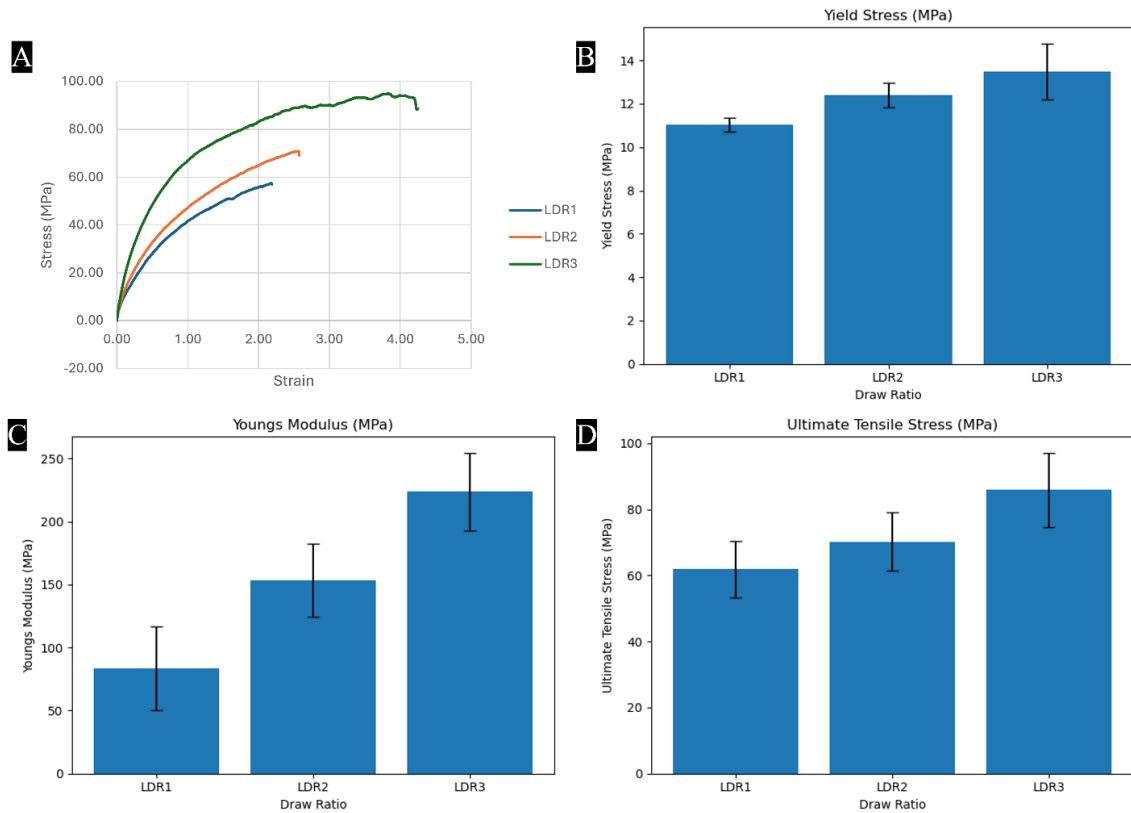


**Figure 33.** Mechanical behavior of nanoyarns **(A)** presents stress-strain curves from one nanoyarn sample for LDR1, LDR2, and LDR3. The curves are truncated after the ultimate tensile strength peak for better presentation. **(B)** There is a noticeable upward trend in the yield stress of the nanoyarns from LDR1 to LDR3, indicating an increase in strength, ANOVA p-value < 0.01, all group-to-group comparisons with student t-tests give a p-value < 0.01, except for groups LDR2 vs LDR3. **(C)** The Young's Modulus, a measure of stiffness, exhibits a continuous increase from LDR1 to LDR3, ANOVA p-value < 0.01, all group-to-group comparisons with student t-test give a p-value < 0.01, except for groups LDR1 vs LDR3. **(D)** Similarly, the ultimate tensile strength, which represents the maximum stress the material can withstand, also shows an increase from LDR1 to LDR3 (n = 5) for figures (B-D), ANOVA p-value < 0.01, all group-to-group comparisons with student t-test have a p-value < 0.01 for LDR1 vs LDR3 only.

The findings from this research study reveal a notable disparity in specific strength between the nanofiber control samples and the PVDF-HFP nano yarn. Also, the strength ratios for DR 1, 2, and 3 nanofibers to nanoyarns are 95.9, 45.5, and 45.8 respectively. The nanofiber control samples exhibited significantly higher specific strength. This difference

became increasingly pronounced as the draw ratios increased, suggesting that the nanofiber control samples maintain their strength advantage even under higher tensile forces. One plausible explanation for the observed strength discrepancy lies in the inherent structure of the nano yarns. Unlike the nanofiber control samples, which consist of individual nanofibers, the nano yarns are composed of multiple twisted nanofibers. This twisted configuration may introduce structural defects or cause the unraveling of the yarns, affecting their overall strength compared to individually drawn nanofibers.

### **4.3 Morphology Analysis**

The scanning electron microscope (SEM) imaging of nanofibers and yarns collected using an automated track device (DR1, DR2, DR3) clearly shows that the fibers have an aligned orientation. The SEM results from (Tables 3 & 4) reveal interesting trends in nanofiber and nanoyarn diameters across different samples and processing conditions. A pictorial representation of these results is shown in Figure 34 and Figure 35. For the nanofiber diameters, a decreasing trend is observed from DR1 ( $1.120 \pm 0.150 \mu\text{m}$ ) to DR2 ( $1.081 \pm 0.112 \mu\text{m}$ ) and DR3 ( $1.067 \pm 0.121 \mu\text{m}$ ), suggesting that the post-drawing process causes a reduction in nanofiber diameter. A clear trend emerges based on the density and draw ratio groups regarding the nano yarn diameters. The high-density group (HDR3) exhibited the largest average diameter of  $505 \pm 34.5 \mu\text{m}$ , followed by the medium-density group (MDR3) with  $449 \pm 11.2 \mu\text{m}$ , and the low-density groups (LDR1, LDR2, LDR3) have decreasing average diameters ranging from  $429 \pm 11.2 \mu\text{m}$  to  $352 \pm 27.5 \mu\text{m}$ . Therefore, these results show that the nano yarn diameter increases with increasing density and decreases with draw ratio.

**Table 3***Average Nanofiber Diameters and Standard Deviation for Each Group (n = 5)*

Sample Name	Initial Length (mm)	Final Length (mm)	Average Nanofiber Diameter ( $\mu\text{m}$ )	Average No of Fiber/sample
DR1	120	120	$1.120 \pm 0.150$	$960 \pm 120$
DR2	60	120	$1.081 \pm 0.112$	$940 \pm 90$
DR3	40	120	$1.067 \pm 0.121$	$850 \pm 90$

**Table 4***Average Nanoyarn Diameters and Standard Deviation for Each Group (n = 5)*

Sample Name	Average Nanoyarn Diameter ( $\mu\text{m}$ )
Low density (LDR1)	$429 \pm 11.2$
Low density (LDR2)	$374 \pm 21.3$
Low density (LDR3)	$352 \pm 27.5$
Medium density (MDR3)	$449 \pm 11.2$
High density (HDR3)	$505 \pm 34.5$

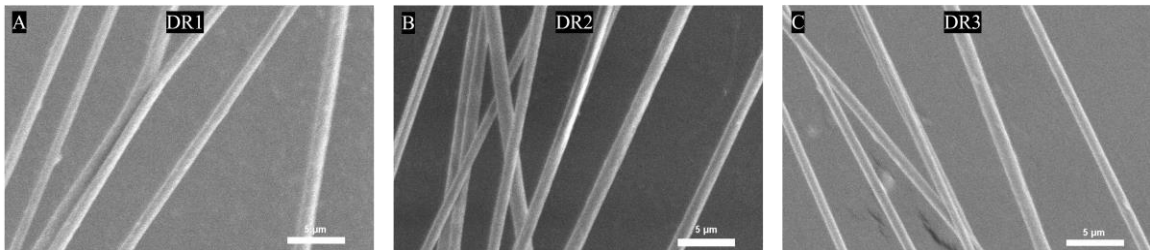
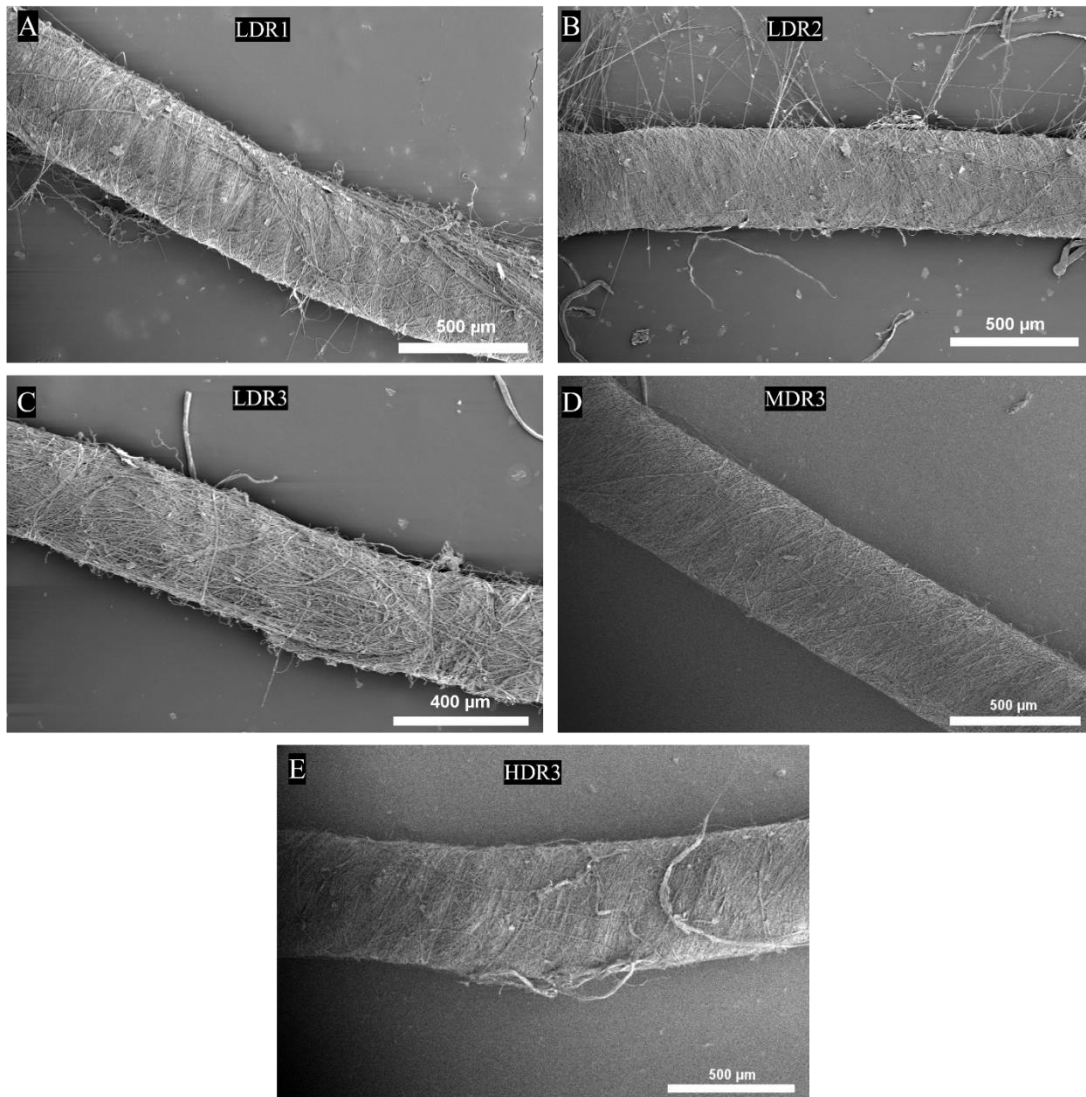


Figure 34. (A-C) shows representative SEM images of PVDF-HFP nanofiber with low linear density (fixed) and component fiber draw ratio varied from DR1-DR3. All scale bars = 5  $\mu\text{m}$



*Figure 35.* (A-E) shows representative SEM images of PVDF-HFP nanoyarns with low linear density (fixed), medium linear density, high linear density, and component fiber draw ratio varied from DR1-DR3 for LDR1, LDR2, LDR3, MDR3, and HDR3, respectively. Scale bars are 400 and 500  $\mu\text{m}$ .

#### 4.4 Fourier Transform Infrared Spectroscopy (FTIR) Analysis

The  $\beta$ -phase content, a key indicator of piezoelectric efficiency, showed a substantial rise from 0.532 in the film to 0.924 in the DR1 nanofibers (Table 5). However, the nanofibers'  $\beta$ -phase content showed no substantial increase as the draw ratio increased from DR1 to DR2 to DR3 (0.924, 0.939, 0.857, respectively). These  $\beta$ -phase values, calculated using Beer-Lambert's law with the  $\beta$ -phase peak at  $840\text{ cm}^{-1}$  and the  $\alpha$ -phase peak at  $761\text{ cm}^{-1}$ , provide key insights into the piezoelectric properties.

A similar trend was observed for nanoyarns. The  $\beta$ -phase content increased from 0.532 in the film to 0.971 in the DR3 nanoyarns. However, there was no significant increase in  $\beta$ -phase content as the draw ratio increased from DR1 to DR2 to DR3 (0.966, 0.973, 0.971, respectively). It is worth noting that the  $\beta$ -phase content does not drop for nanoyarns as it does in fibers. Although there is no statistical difference in  $\beta$ -phase percentage between fibers and nanofibers, the yarns exhibited higher  $\beta$ -phase content, which could be due to the stretching that occurs during yarn spinning.

This polarized Fourier Transform Infrared (FTIR) spectroscopy method involves analyzing the relative intensities of specific vibrational bands in the infrared spectra obtained with the infrared beam oriented parallel and perpendicular to the nanofiber axis. The dichroic ratio, calculated from the parallel and perpendicular absorbances, provides a quantitative measure of the molecular order in the nanofibers. A dichroic ratio of zero indicates a disordered polymer chain, while values closer to -1 and 1 represent the parallel and perpendicular alignment of bonds or functional groups relative to the fiber axis, respectively (133).

The dichroic ratio data from (Table 7) provides insights into the molecular orientation and order within the PVDF-HFP nanofibers at different draw ratios. The wavenumbers  $1400\text{ cm}^{-1}$ ,  $1180\text{ cm}^{-1}$ ,  $1070\text{ cm}^{-1}$ , and  $474\text{ cm}^{-1}$  exhibit increasingly negative dichroic ratios with higher draw ratios, indicating a progressive alignment of the corresponding chemical bonds or functional groups parallel to the fiber axis. This trend suggests an enhancement in molecular order and orientation along the fiber direction as the draw ratio increases. Although the  $474\text{ cm}^{-1}$  peak, linked to the  $\beta$ -phase is less frequently mentioned in literature, it is observed in electrospun PVDF and is thought to be a result of the electrospinning process (133,142–145). Previous research studies have connected peaks in the  $473\text{-}475\text{ cm}^{-1}$  range with the  $\beta$ -phase of PVDF. Additionally, the  $474\text{ cm}^{-1}$  peak was noted in a study where a supercritical PVDF solution was rapidly expanded through a heated capillary nozzle, a process that shares a high strain rate with electrospinning, which may explain its occurrence in this study (133,146). On the other hand, the wavenumbers  $1278\text{ cm}^{-1}$ ,  $881\text{ cm}^{-1}$ , and  $840\text{ cm}^{-1}$  display a contrasting behavior. The dichroic ratio for  $1278\text{ cm}^{-1}$  transitions from a slightly negative value at DR1 to a positive value of 0.636 at DR3, implying a reorientation of these bonds from a parallel to a perpendicular alignment relative to the fiber axis with an increasing draw ratio. The wavenumbers  $881\text{ cm}^{-1}$  and  $840\text{ cm}^{-1}$  exhibit small positive dichroic ratios around 0.1 to 0.2, suggesting a slight perpendicular orientation relative to the fiber axis, which remains relatively unchanged across the different draw ratios

The most notable observation is the substantial increase in the dichroic ratio at  $1278\text{ cm}^{-1}$  for the DR1 nanofiber sample. This significant increase in the dichroic ratio indicates an enhancement in the parallel alignment of these bonds along the fiber axis, suggesting an

improvement in molecular order and orientation within the nanofibers as the draw ratio increases. It is hypothesized that the high dichroic ratio of the DR1 nanofiber, even without post-drawing, can be attributed to the electrospinning process itself. During electrospinning, the polymer solution is subjected to a strong electric field, which causes the polymer chains to align along the direction of the applied field. The stretching of the polymer jet further enhances this alignment as it travels towards the collector. Additionally, the use of a parallel track collector contributes to the high dichroic ratio observed in the DR1 nanofiber sample (133,147,148).

Also, the molecular orientation and alignment of various bonds and functional groups within the PVDF-HFP nano yarn samples were of different draw ratios. The dichroic ratio, which quantifies the degree of alignment relative to the fiber axis, is a powerful tool for understanding the structural changes induced by the drawing process. The positive dichroic ratios at wavenumbers 1400  $\text{cm}^{-1}$  and 1070  $\text{cm}^{-1}$  indicate that the corresponding bonds or functional groups tend to align parallel to the fiber axis. This parallel alignment becomes more pronounced with increasing draw ratios, as evidenced by the increasing dichroic ratio values. Conversely, the negative dichroic ratios observed at wavenumbers 1278  $\text{cm}^{-1}$ , 1180  $\text{cm}^{-1}$ , 881  $\text{cm}^{-1}$ , and 840  $\text{cm}^{-1}$  suggest a perpendicular alignment of the associated bonds or functional groups relative to the fiber axis.

Notably, the absolute values of these negative dichroic ratios increase with higher draw ratios, signifying an enhanced perpendicular alignment and molecular order. The observed trends in the dichroic ratios can be attributed to the specific bond angles and conformations within the PVDF-HFP polymer chains. The peak at 1178  $\text{cm}^{-1}$  is attributed to the  $\alpha$ -phase of the polymer, representing symmetric  $\text{CF}_2$  stretching and  $\text{CH}_2$  twisting

vibrations (133,144,149). The  $1400\text{ cm}^{-1}$  peak corresponds to the  $\beta$ -phase, involving  $\text{CH}_2$  wagging and CC antisymmetric stretching, with a dipole moment change parallel to the polymer backbone. The  $1278\text{ cm}^{-1}$  peak, also associated with the  $\beta$ -phase, relates to symmetric stretching of  $\text{CF}_2$  and CC, as well as CCC bending, exhibiting a dipole moment change orthogonal to the backbone. For instance, the bonds contributing to the  $1400\text{ cm}^{-1}$  peak are known to align parallel to the PVDF backbone, while those for the  $1278\text{ cm}^{-1}$  peak tend to orient perpendicular to the backbone. This behavior is influenced by the inherent molecular structure and the rearrangement of polymer chains during the drawing process (133,150).

**Table 5**

*Average  $\beta$ -phase Content for Nanofiber at Different Draw Ratios*

<b>Average Beta Phase Content (Nanofiber)</b>			
Film	DR1	DR2	DR3
0.532	0.924	0.939	0.857

**Table 6**

*Average  $\beta$ -phase Content for Nanofiber Yarn or Nano Yarns at Different Draw Ratios*

<b>Average Beta Phase Content (Nanofiber Yarn)</b>			
Film	DR1	DR2	DR3
0.532	0.966	0.973	0.971

**Table 7**

*The Dichroic Ratio for Each Group Nanofiber (n = 1) for the Wavenumbers 1400 cm<sup>-1</sup>, 1278 cm<sup>-1</sup>, 1180 cm<sup>-1</sup>, 1070 cm<sup>-1</sup>, 881 cm<sup>-1</sup>, 840 cm<sup>-1</sup>, and 474 cm<sup>-1</sup>.*

<b>Dichroic Ratio (Nanofiber)</b>							
	1400 cm <sup>-1</sup>	1278 cm <sup>-1</sup>	1180cm <sup>-1</sup>	1070 cm <sup>-1</sup>	881 cm <sup>-1</sup>	840 cm <sup>-1</sup>	474 cm <sup>-1</sup>
DR1	-0.478	-0.161	-0.234	-0.644	-0.0105	0.103	-0.818
DR2	-0.531	0	-0.165	-0.696	0.0588	0.231	-0.587
DR3	-0.592	0.636	-0.123	-0.7	0.0256	0.231	-0.996

**Table 8**

The Dichroic Ratio for Each Group Nano Yarn ( $n = 1$ ) for the Wavenumbers  $1400\text{ cm}^{-1}$ ,  $1278\text{ cm}^{-1}$ ,  $1180\text{ cm}^{-1}$ ,  $1070\text{ cm}^{-1}$ ,  $881\text{ cm}^{-1}$ , and  $840\text{ cm}^{-1}$ .

<b>Dichroic Ratio (Nanoyarn)</b>						
	$1400\text{ cm}^{-1}$	$1278\text{ cm}^{-1}$	$1180\text{ cm}^{-1}$	$1070\text{ cm}^{-1}$	$881\text{ cm}^{-1}$	$840\text{ cm}^{-1}$
DR1	0.386	-0.154	-0.066	0.208	-0.096	-0.118
DR2	-0.007	-0.364	-0.248	0.205	-0.270	-0.364
DR3	0.068	-0.500	-0.277	0.325	-0.333	-0.418

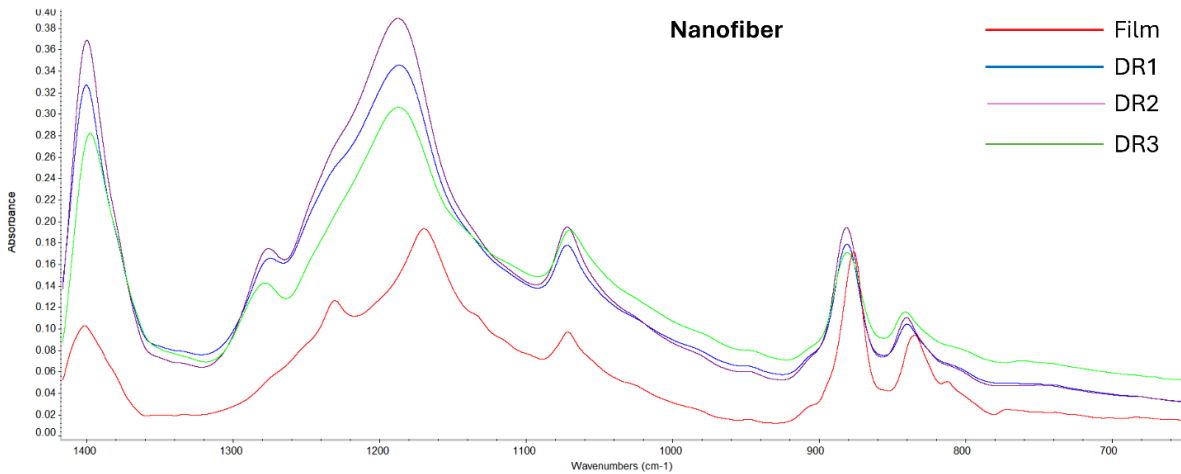


Figure 36. Non-polarized FTIR representative spectra for the film and nanofiber at DR1, DR2, and DR3.

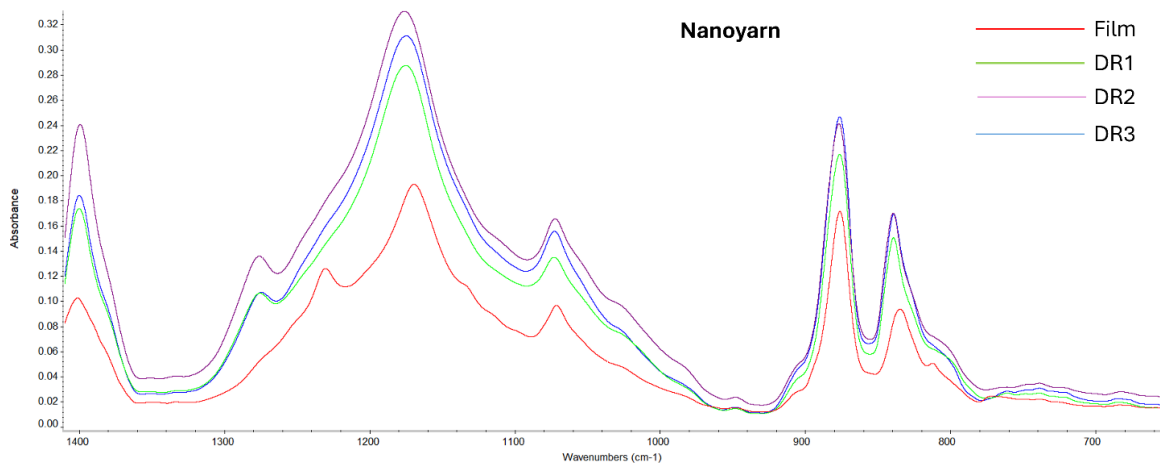


Figure 37. Non-polarized FTIR representative spectra for film and nano yarn at DR1, DR2, and DR3.

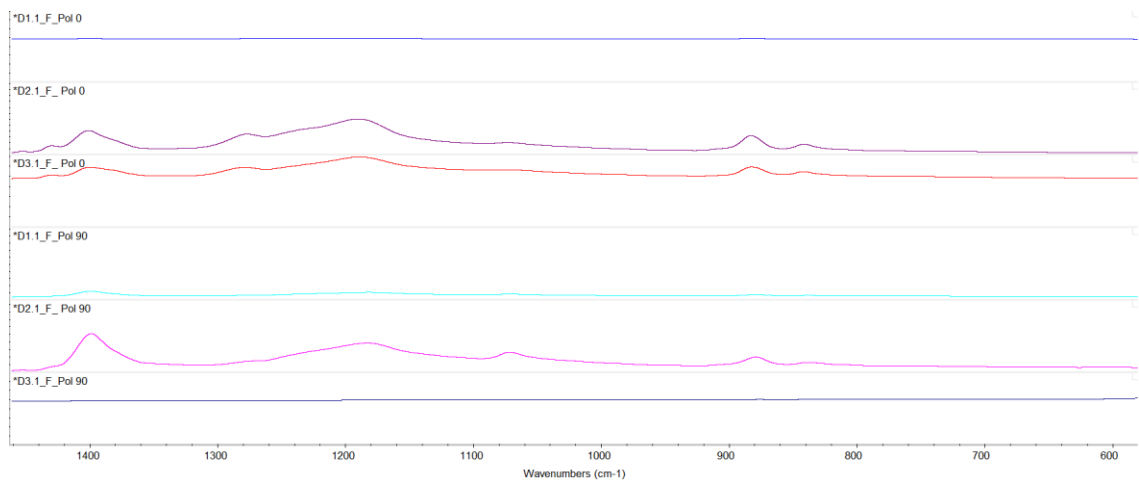


Figure 38. Polarized 0° and 90° FTIR representative spectra for DR1, DR2, and DR3 nanofiber.

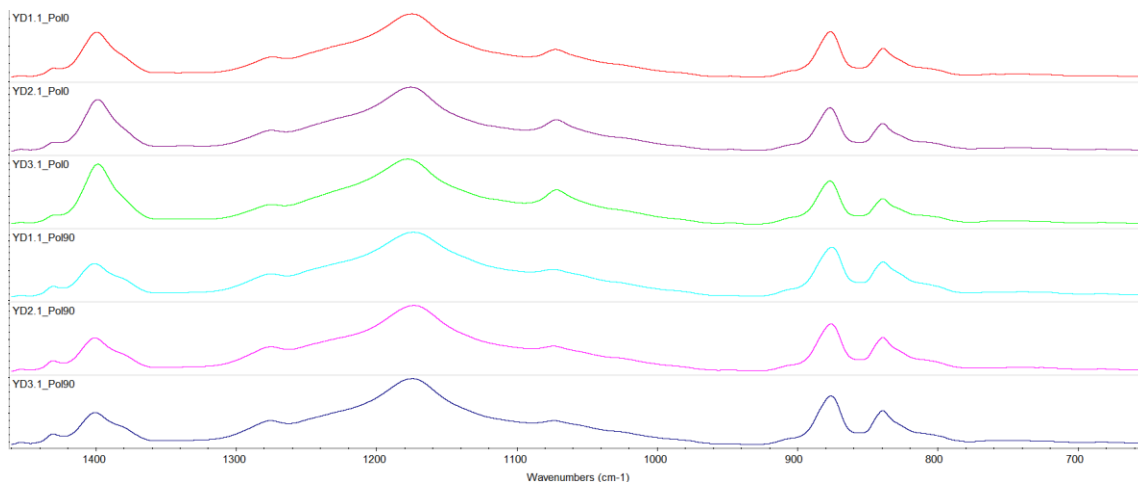
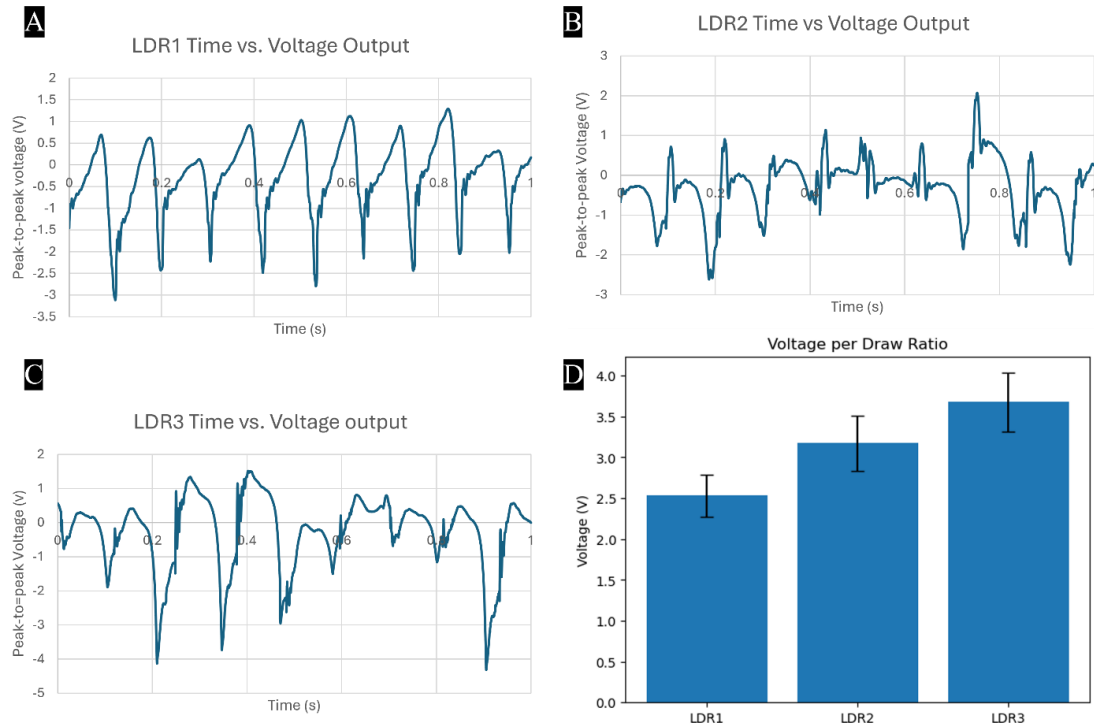


Figure 39. Polarized 0° and 90° FTIR representative spectra for DR1, DR2, and DR3 nanoyarn.

## 4.5 Mechanical-Electrical Testing Analysis

### 4.5.1 Flick Deformation Analysis

The average peak-to-peak voltage from Figure 40 and Figure 41 shows a clear increasing trend with a draw ratio. The average voltage for LDR1 is 2.53 V, followed by 3.17 V for LDR2 and 3.67 V for LDR3. This suggests that higher draw ratios increase voltage generation in the yarns. The voltage per draw ratio also positively correlates with fiber density. For the DR3 group, the voltage per density gradually increases from low to medium density (3.67 V to 4.06 V) and significantly from low to high density (3.67 V to 4.28 V). This indicates that higher fiber densities contribute to enhanced voltage generation, particularly in the DR3 group.



*Figure 40.* Flick deformation test **(A-C)** Peak-to-peak voltage outputs for LDR1, LDR2, and LDR3, respectively. **(D)** Voltage per draw ratio (V), ANOVA p-value < 0.01, all group-to-group comparisons with student t-test give a p-value < 0.01 for group LDR1 vs LDR3 only.

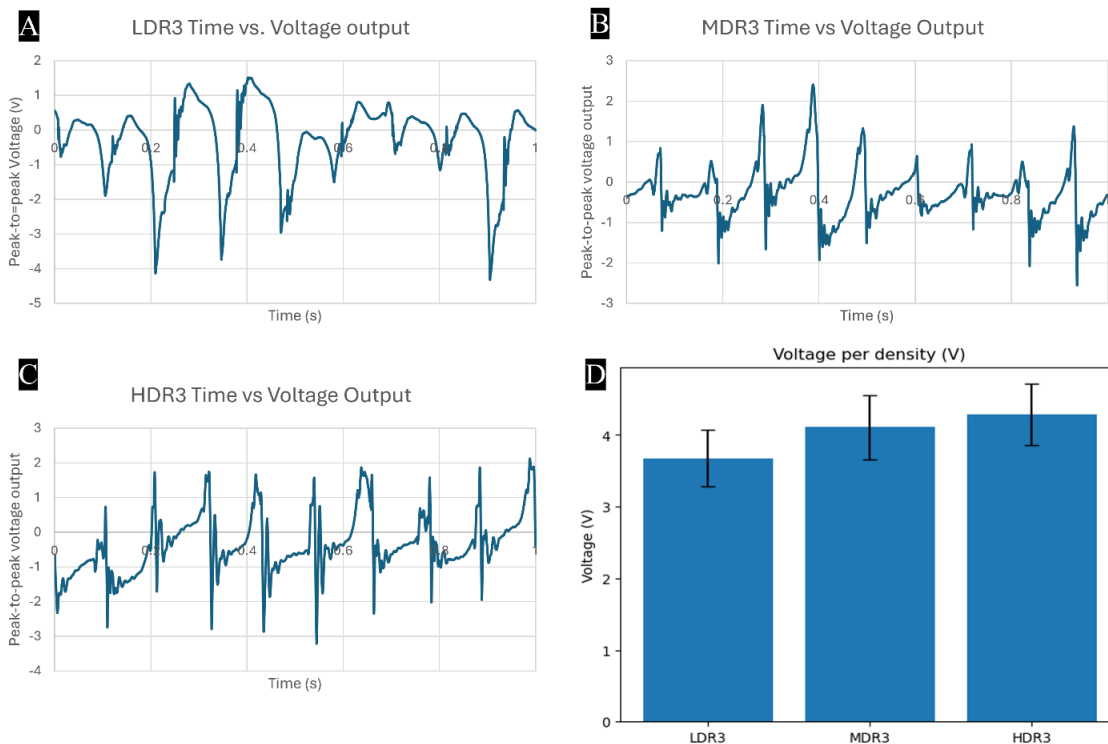


**Figure 41.** Flick deformation test **(A-C)** Peak-to-peak voltage outputs for LDR3, MDR3, and HDR3, respectively. **(D)** Voltage per density (V), ANOVA p-value > 0.01, and all group-to-group comparisons with student t-tests give a p-value > 0.01.

#### 4.5.2 Stretch Deformation Analysis

These results from Figure 42 and Figure 43 indicate a strong positive correlation between the fiber density of the material and voltage generation. The voltage generation significantly increased as the fiber density increased from low to medium and high levels. The average peak-to-peak voltage for the low-density (LD) fiber density group was 2.44 V. This suggests that even at low fiber densities, the material could generate a measurable voltage, indicating the potential for energy harvesting applications. The average peak-to-peak voltage for the medium-density (MD) fiber density group was 4.23 V. This represents a significant increase compared to the low-density group, demonstrating the impact of

higher fiber densities on voltage generation. The average peak-to-peak voltage for the high-density (HD) fiber density group was 4.60 V.

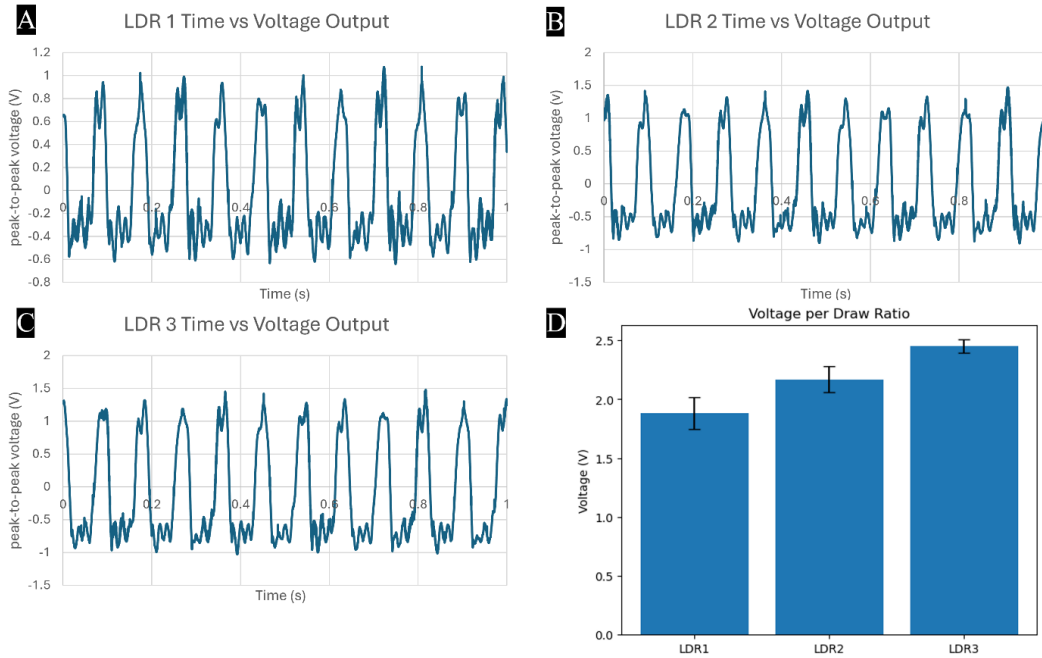


*Figure 42.* Stretch deformation test **(A-C)** Peak-to-peak voltage outputs for LDR1, LDR2, and LDR3, respectively. **(D)** Voltage per draw ratio (V), ANOVA p-value < 0.01, and all group-to-group comparisons with student t-test give a p-value < 0.01.

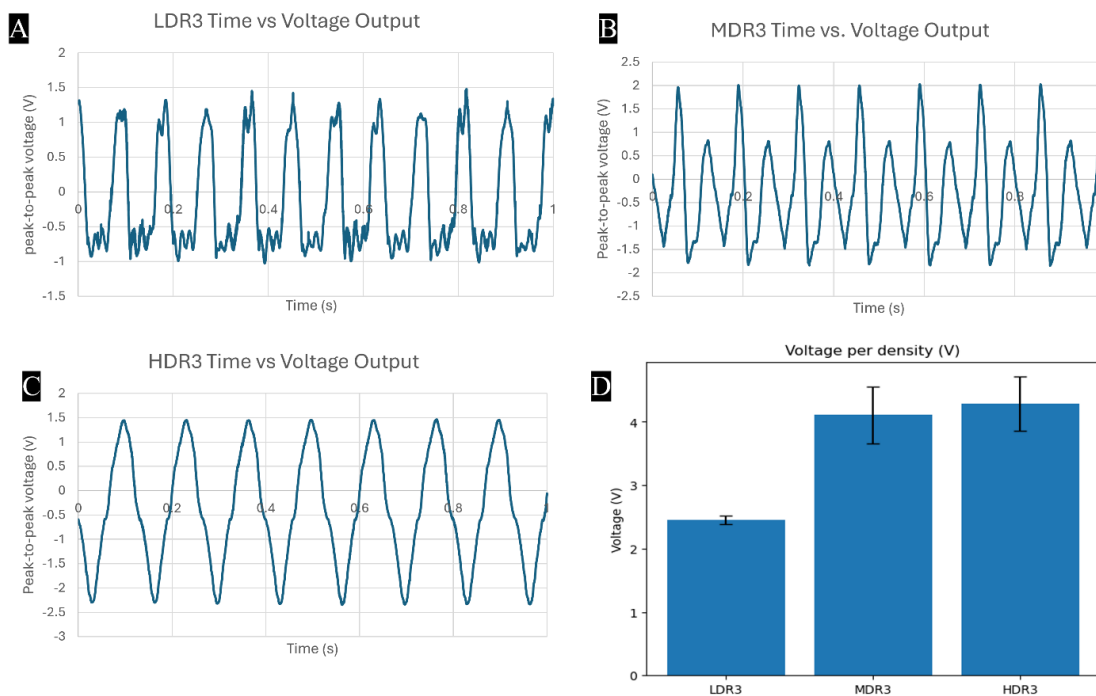


**Figure 43.** Stretch deformation test **(A-C)** peak-to-peak voltage outputs for LDR3, MDR3, and HDR3, respectively. **(D)** Voltage per density (V), ANOVA p-value < 0.01, and all group-to-group comparisons with student t-test give a p-value < 0.01 except for groups MDR3 vs HDR3.

The combination of increasing draw ratio and fiber density appears to have a synergistic effect on voltage generation. As both draw ratio and density increase, the voltage output increases more than the individual effects of each factor. This is evident in the significant jump in voltage from medium to high density in the DR3 group. The observed trends and correlations can be attributed to several factors, such as changes in fiber alignment, cross-sectional area, and surface properties due to the draw ratio and density variations. Higher draw ratios can lead to better fiber alignment and increased surface area, while higher densities may result in more efficient charge transfer and storage within the yarn structure.

The voltage output from electrospun PVDF-HFP twisted nanofiber yarns or filaments in energy harvesting devices exhibits a wide range. The highest reported voltage was 2.8 V for PVDF-HFP/Co-ZnO nanocomposite nanofibers in a flexible nanogenerator (151). Nanofibers made of PVDF were electrospun and coated onto nylon microfibers that had silver deposited on them, resulting in a nanogenerator based on an electrospun nanofiber coverspun yarn. This fabricated piezoelectric yarn nanogenerator demonstrated an average peak voltage of 0.52 V when subjected to cyclic compression. The combination of nanofibers and microfibers with deposited silver enabled this nanogenerator to generate a voltage from applied compression. (40,152).

The overall electrical output of piezoelectric devices is influenced not only by the piezoelectric material itself but also by the device design and mechano-electrical configuration. Notably, this study observed systematic increases in energy conversion as the draw ratios and fiber densities of the nanofiber yarns increased, irrespective of the voltage magnitude. The PVDF-HFP yarns tested in this work demonstrated voltages nearly an order of magnitude higher when subjected to flicking (bending deformation) and stretching (axial deformation). These findings indicate that both draw ratio and fiber density significantly impact voltage generation in the yarns. The synergistic effect of these factors suggests that optimizing both draw ratio and density could lead to enhanced voltage output, which may have important implications for developing high-performance energy-harvesting textiles (40,133).

#### 4.6. Statistical Analysis

This research study employed a comprehensive statistical analysis strategy to thoroughly understand the relationships and trends within the collected data. This approach encompassed group-level analyses across all measured parameters, including diameters, mechanical properties, and electrical characteristics. The averages and standard deviations of a population were calculated for each group using Microsoft Excel. Group-to-group comparisons were conducted to identify significant differences and patterns among the various experimental conditions or sample groups. The data processing and visualization tasks were streamlined using Python libraries, namely NumPy, Pandas, and Matplotlib. NumPy facilitated efficient numerical computations, while Pandas provided robust data manipulation and analysis capabilities. Matplotlib enabled the creation of informative and visually appealing plots and graphs, aiding in the interpretation and communication of the findings.

Industry-standard techniques were employed to ensure the statistical validity of the analyses. Analysis of Variance (ANOVA) tests assessed statistically significant differences among multiple groups or conditions. Additionally, t-tests were conducted to evaluate the significance of differences between pairs of groups or conditions. The SciPy library, a comprehensive collection of mathematical algorithms and statistical tools for Python, facilitated these analyses. Through this comprehensive approach, encompassing group-level analyses, data processing, visualization, and rigorous statistical testing, a thorough understanding of the underlying patterns and relationships within the data was achieved, enabling informed decision-making and the derivation of meaningful conclusions.

## Chapter 5

### Conclusion and Future Work

#### 5.1 Conclusion

The study investigated the influence of processing conditions, specifically draw ratio and fiber density, on the properties and performance of PVDF-HFP nanofibers and nano yarns. The results revealed significant correlations between these factors and the materials' specific strength, fiber morphology, crystalline structure, molecular orientation, and voltage generation capabilities. The specific strength of the nano yarns increased substantially with increasing draw ratio and fiber density, with the high-density DR3 sample exhibiting the highest specific strength. Interestingly, the nanofiber control samples demonstrated even higher specific strength than the nano yarns. This suggests that the twisting process involved in nano yarn production may have introduced structural defects or misalignments. More importantly, the yarns can fail when individual fibers slip past one another, overcoming the friction forces between fibers, and fail even if the fibers themselves do not fail, reducing the overall strength. SEM imaging confirmed the aligned orientation of nanofibers and nano yarn across all draw ratios while revealing a decrease in nanofiber diameters and an increase in nano yarn diameters with increasing draw ratio and fiber density, respectively.

The processing conditions also influenced the materials' crystalline structure and molecular orientation. The  $\beta$ -phase content increased significantly from the film to the DR1 nanofibers but remained relatively constant with further increases in draw ratio. Polarized FTIR analysis showed molecular order in the PVDF-HFP nanofibers, with certain bonds exhibiting preferential alignment parallel or perpendicular to the fiber axis. Increasing the

draw ratio led to increased molecular order, as evidenced by the increasing absolute value of spectral differences in parallel versus perpendicular infrared absorbances.

Notably, the average peak-to-peak voltage generated by the nano yarns increased with increasing draw ratio and fiber density, indicating the synergistic effect of these factors on voltage output. The high-density DR3 sample exhibited the highest voltage generation, suggesting the potential for developing high-performance energy-harvesting textiles by optimizing processing conditions. The material could generate a measurable voltage even at low fiber densities, demonstrating its potential for energy-harvesting applications. The improved electrical performance of these yarns with increasing draw ratio and fiber density may be attributed to superior macromolecular and crystalline alignment experienced during post-drawn conditions, despite the total  $\beta$ -phase content not appearing to increase significantly. The post-drawing process led to better organization and alignment of the existing piezoelectric  $\beta$ -phase regions within the polymer material. This enhanced molecular and crystalline alignment coincided with amplification in the overall piezoelectricity of the post-drawn samples. While the  $\beta$ -phase content did not change much across draw ratios, the drawing enabled optimal orientation of those piezoelectric regions, maximizing the piezoelectric response.

## **5.2 Future Work**

Future research should investigate the relationship between draw ratio, fiber density, and their synergistic effects to determine the optimal combination for maximizing voltage generation. A comprehensive investigation into the long-term stability and

durability of voltage generation under various environmental conditions and mechanical stresses is crucial. Additionally, exploring different deformation modes, such as torsion or compression, could provide valuable insights into the piezoelectric behavior of the PVDF-HFP nanoyarns.

To facilitate commercial use in industries like smart textiles, future work should focus on increasing the manufacturing efficiency, yield, and uniformity of the piezoelectric nanoyarns. Developing scalable manufacturing processes to produce large quantities of optimized nanofiber yarns with consistent voltage generation and mechanical properties across large-scale production batches is essential. A key objective is achieving commercial-length (>100 m) and high-quality piezoelectric nanoyarns.

Investigating alternative piezoelectric polymer materials, such as PVDF copolymers or blends, could lead to improved voltage generation or enhanced mechanical properties. Furthermore, a comprehensive study on the influence of different rotational speeds (rpm) during electrospinning could ascertain the various frequency ranges at which the PVDF-HFP nanoyarn material can operate effectively.

The potential applications of these piezoelectric nanoyarns in wearable energy harvesting devices and smart textiles should be further explored. Integrating these materials into functional prototypes and evaluating their performance in real-world scenarios could pave the way for innovative applications in the field of energy harvesting and smart textiles.

## References

1. Mokhtari F, Azimi B, Salehi M, Hashemikia S, Danti S. Recent advances of polymer-based piezoelectric composites for biomedical applications. Vol. 122, *Journal of the Mechanical Behavior of Biomedical Materials*. Elsevier Ltd; 2021.
2. Singh RK, Lye SW, Miao J. Holistic investigation of the electrospinning parameters for high percentage of  $\beta$ -phase in PVDF nanofibers. *Polymer (Guildf)*. 2021 Feb 1;214.
3. Mwiiri FK, Daniels R. Electrospun nanofibers for biomedical applications. In: *Delivery of Drugs: Volume 2: Expectations and Realities of Multifunctional Drug Delivery Systems*. Elsevier Inc.; 2020. p. 53–74.
4. Liu L, Xu W, Ding Y, Agarwal S, Greiner A, Duan G. A review of smart electrospun fibers toward textiles. *Composites Communications*. 2020 Dec 1;22.
5. Kalimuldina G, Turdakyn N, Abay I, Medeubayev A, Nurpeissova A, Adair D, et al. A review of piezoelectric pvdf film by electrospinning and its applications. Vol. 20, *Sensors (Switzerland)*. MDPI AG; 2020. p. 1–42.
6. Zaarour B, Zhu L, Huang C, Jin X. Fabrication of a polyvinylidene fluoride cactus-like nanofiber through one-step electrospinning. *RSC Adv*. 2018;8(74):42353–60.
7. Frenot A, Chronakis IS. Polymer nanofibers assembled by electrospinning. *Curr Opin Colloid Interface Sci [Internet]*. 2003 Mar [cited 2023 Aug 7];8(1):64–75. Available from: [https://libkey.io/libraries/600/articles/6905337/content-location?utm\\_source=api\\_132](https://libkey.io/libraries/600/articles/6905337/content-location?utm_source=api_132)
8. Reneker DH, Yarin AL. Electrospinning jets and polymer nanofibers. *Polymer (Guildf) [Internet]*. 2008 May [cited 2023 Aug 7];49(10):2387–425. Available from: [https://libkey.io/libraries/600/articles/6385957/content-location?utm\\_source=api\\_132](https://libkey.io/libraries/600/articles/6385957/content-location?utm_source=api_132)
9. Xue J, Wu T, Dai Y, Xia Y. Electrospinning and electrospun nanofibers: Methods, materials, and applications. Vol. 119, *Chemical Reviews*. American Chemical Society; 2019. p. 5298–415.
10. Peng HK, Wu MM, Wang YT, Li TT, Sun F, Lou CW, et al. Enhancing piezoelectricity of poly(vinylidene fluoride) nano-wrapped yarns with an innovative yarn electrospinning technique. *Polym Int*. 2021 Jun 1;70(6):851–9.
11. Schwarz A, Van Langenhove L, Guermonprez P, Deguillemont D. A roadmap on smart textiles. *Textile Progress*. 2010 Jul 16;42(2):99–180.
12. The Business Research Company. Smart Textiles Global Market Opportunities and Strategies To 2031 [Internet]. 2023 [cited 2024 Apr 27]. Available from: <https://www.globenewswire.com/en/news-release/2023/04/04/2640431/28124/en/Global-Smart-Textiles-Market-Opportunities-and-Strategies-to-2031-North-America-was-the-Largest-Region-in-2021.html>

13. Persano L, Ghosh SK, Pisignano D. Enhancement and Function of the Piezoelectric Effect in Polymer Nanofibers. *Acc Mater Res.* 2022 Sep 23;3(9):900–12.
14. Hiwrale A, Bharati S, Pingale P, Rajput A. Nanofibers: A current era in drug delivery system. *Heliyon.* 2023 Sep;9(9):e18917.
15. Khajavi R, Abbasipour M, Bahador A. Electrospun biodegradable nanofibers scaffolds for bone tissue engineering. *J Appl Polym Sci.* 2016 Jan 15;133(3).
16. Vasita R, Katti DS. Nanofibers and their applications in tissue engineering. *Int J Nanomedicine.* 2006;1(1):15–30.
17. Sivan M, Madheswaran D, Valtera J, Kostakova EK, Lukas D. Alternating current electrospinning: The impacts of various high-voltage signal shapes and frequencies on the spinnability and productivity of polycaprolactone nanofibers. *Mater Des.* 2022 Jan;213:110308.
18. He Z, Rault F, Vishwakarma A, Mohsenzadeh E, Salaün F. High-Aligned PVDF Nanofibers with a High Electroactive Phase Prepared by Systematically Optimizing the Solution Property and Process Parameters of Electrospinning. *Coatings.* 2022 Sep 7;12(9):1310.
19. Li D, Xia Y. Electrospinning of Nanofibers: Reinventing the Wheel? *Advanced Materials.* 2004 Jul 19;16(14):1151–70.
20. da Silva Parize DD, Foschini MM, de Oliveira JE, Klamczynski AP, Glenn GM, Marconcini JM, et al. Solution blow spinning: parameters optimization and effects on the properties of nanofibers from poly(lactic acid)/dimethyl carbonate solutions. *J Mater Sci.* 2016 May 3;51(9):4627–38.
21. Ho DH, Cheon S, Hong P, Park JH, Suk JW, Kim DH, et al. Multifunctional Smart Textronics with Blow-Spun Nonwoven Fabrics. *Adv Funct Mater.* 2019 Jun 14;29(24).
22. Lu Y, Li Y, Zhang S, Xu G, Fu K, Lee H, et al. Parameter study and characterization for polyacrylonitrile nanofibers fabricated via centrifugal spinning process. *Eur Polym J.* 2013 Dec;49(12):3834–45.
23. Gao H, Asheghali D, Yadavalli NS, Pham MT, Nguyen TD, Minko S, et al. Fabrication of core-sheath nanoyarn via touchspinning and its application in wearable piezoelectric nanogenerator. *The Journal of The Textile Institute.* 2020 Jun 2;111(6):906–15.
24. Padron S, Fuentes A, Caruntu D, Lozano K. Experimental study of nanofiber production through forcespinning. *J Appl Phys.* 2013 Jan 14;113(2).
25. Barhoum A, Rasouli R, Yousefzadeh M, Rahier H, Bechelany M. Nanofiber Technology: History and Developments. In: *Handbook of Nanofibers.* Cham: Springer International Publishing; 2018. p. 1–42.

26. Tucker N, Stanger JJ, Staiger MP, Razzaq H, Hofman K. The History of the Science and Technology of Electrospinning from 1600 to 1995. *J Eng Fiber Fabr.* 2012 Jun 1;7(2\_suppl):155892501200702.
27. Azimi B, Milazzo M, Lazzeri A, Berrettini S, Uddin MJ, Qin Z, et al. Electrospinning Piezoelectric Fibers for Biocompatible Devices. *Adv Healthc Mater.* 2020 Jan 8;9(1):1901287.
28. Xin Y, Zhu J, Sun H, Xu Y, Liu T, Qian C. A brief review on piezoelectric PVDF nanofibers prepared by electrospinning. *Ferroelectrics.* 2018 Apr 4;526(1):140–51.
29. Gee S, Johnson B, Smith AL. Optimizing electrospinning parameters for piezoelectric PVDF nanofiber membranes. *J Memb Sci.* 2018 Oct 1;563:804–12.
30. Deitzel JM, Kleinmeyer J, Harris D, Beck Tan NC. The effect of processing variables on the morphology of electrospun nanofibers and textiles. *Polymer (Guildf).* 2001 Jan;42(1):261–72.
31. Doshi J, Reneker DH. Electrospinning process and applications of electrospun fibers. *J Electrostat.* 1995 Aug;35(2–3):151–60.
32. Casper CL, Stephens JS, Tassi NG, Chase DB, Rabolt JF. Controlling Surface Morphology of Electrospun Polystyrene Fibers: Effect of Humidity and Molecular Weight in the Electrospinning Process. *Macromolecules.* 2004 Jan 1;37(2):573–8.
33. Jacobs V, Anandjiwala RD, Maaza M. The influence of electrospinning parameters on the structural morphology and diameter of electrospun nanofibers. *J Appl Polym Sci.* 2010 Mar 5;115(5):3130–6.
34. Haider A, Haider S, Kang IK. A comprehensive review summarizing the effect of electrospinning parameters and potential applications of nanofibers in biomedical and biotechnology. *Arabian Journal of Chemistry.* 2018 Dec;11(8):1165–88.
35. Beachley V, Wen X. Effect of electrospinning parameters on the nanofiber diameter and length. *Materials Science and Engineering: C.* 2009 Apr;29(3):663–8.
36. Yari A, Teimourian S, Amidi F, Bakhtiyari M, Heidari F, Sajedi N, et al. The role of biodegradable engineered random polycaprolactone nanofiber scaffolds seeded with nestin-positive hair follicle stem cells for tissue engineering. *Adv Biomed Res.* 2016;5(1):22.
37. Yee WA, Kotaki M, Liu Y, Lu X. Morphology, polymorphism behavior and molecular orientation of electrospun poly(vinylidene fluoride) fibers. *Polymer (Guildf).* 2007 Jan;48(2):512–21.
38. Wang Z, Crandall C, Sahadevan R, Menkhaus TJ, Fong H. Microfiltration performance of electrospun nanofiber membranes with varied fiber diameters and different membrane porosities and thicknesses. *Polymer (Guildf).* 2017 Apr;114:64–72.

39. Wang X, Zhang K, Zhu M, Yu H, Zhou Z, Chen Y, et al. Continuous polymer nanofiber yarns prepared by self-bundling electrospinning method. *Polymer (Guildf)*. 2008 May;49(11):2755–61.
40. Wu S, Dong T, Li Y, Sun M, Qi Y, Liu J, et al. State-of-the-art review of advanced electrospun nanofiber yarn-based textiles for biomedical applications. *Appl Mater Today*. 2022 Jun;27:101473.
41. Ketterson JB. Piezoelectricity, Pyroelectricity, and Ferroelectricity. In: *The Physics of Solids*. Oxford University PressOxford; 2016. p. 501–16.
42. Smidt TE, Mack SA, Reyes-Lillo SE, Jain A, Neaton JB. An automatically curated first-principles database of ferroelectrics. *Sci Data*. 2020 Mar 3;7(1):72.
43. Iqbal Khan M, Chandra Upadhyay T. General Introduction to Ferroelectrics. In: *Multifunctional Ferroelectric Materials*. IntechOpen; 2021.
44. Starr MB, Wang X. Coupling of piezoelectric effect with electrochemical processes. *Nano Energy*. 2015 May;14:296–311.
45. Park IW, Kim KW, Hong Y, Yoon HJ, Lee Y, Gwak D, et al. Recent Developments and Prospects of M13- Bacteriophage Based Piezoelectric Energy Harvesting Devices. *Nanomaterials*. 2020 Jan 2;10(1):93.
46. Covaci C, Gontean A. Piezoelectric Energy Harvesting Solutions: A Review. *Sensors*. 2020 Jun 21;20(12):3512.
47. Kamel NA. Bio-piezoelectricity: fundamentals and applications in tissue engineering and regenerative medicine. *Biophys Rev*. 2022 Jun;14(3):717–33.
48. Ballas RG. The Piezoelectric Effect – an Indispensable Solid State Effect for Contemporary Actuator and Sensor Technologies. *J Phys Conf Ser*. 2021 Jan 1;1775(1):012012.
49. Sappati K, Bhadra S. Piezoelectric Polymer and Paper Substrates: A Review. *Sensors*. 2018 Oct 24;18(11):3605.
50. Liu T, Wang Y, Hong M, Venezuela J, Shi W, Dargusch M. Advances in biodegradable piezoelectrics for medical implants. *Nano Today* [Internet]. 2023 Oct;52:101945. Available from: <https://linkinghub.elsevier.com/retrieve/pii/S1748013223001949>
51. Qian W, Yang W, Zhang Y, Bowen CR, Yang Y. Piezoelectric Materials for Controlling Electro-Chemical Processes. *Nanomicro Lett*. 2020 Dec 14;12(1):149.
52. Wakshume DG, Płaczek MŁ. Optimizing Piezoelectric Energy Harvesting from Mechanical Vibration for Electrical Efficiency: A Comprehensive Review. *Electronics (Basel)*. 2024 Mar 5;13(5):987.
53. Aabid A, Raheman MA, Ibrahim YE, Anjum A, Hrairi M, Parveez B, et al. A Systematic Review of Piezoelectric Materials and Energy Harvesters for Industrial Applications. *Sensors*. 2021 Jun 16;21(12):4145.

54. Kim SB, Park H, Kim SH, Wickle HC, Park JH, Kim DJ. Comparison of MEMS PZT Cantilevers Based on  $d_{31}$  and  $d_{33}$  Modes for Vibration Energy Harvesting. *Journal of Microelectromechanical Systems*. 2013 Feb;22(1):26–33.
55. Liu H, Zhong J, Lee C, Lee SW, Lin L. A comprehensive review on piezoelectric energy harvesting technology: Materials, mechanisms, and applications. *Appl Phys Rev*. 2018 Dec 1;5(4).
56. Torah RN, Beeby SP, White NM. Experimental investigation into the effect of substrate clamping on the piezoelectric behaviour of thick-film PZT elements. *J Phys D Appl Phys*. 2004 Apr 7;37(7):1074–8.
57. Cai X, Chen G, Li R, Pan Z, Jia Y. Novel valleytronic and piezoelectric properties coexisting in Janus  $\text{MoAZ}_3\text{H}$  ( $\text{A} = \text{Si, or Ge}$ ;  $\text{Z} = \text{N, P, or As}$ ) monolayers. *J Mater Chem C Mater*. 2024;12(13):4682–9.
58. Al Ahmad M, Allataifeh A. Electrical extraction of piezoelectric constants. *Heliyon*. 2018 Nov;4(11):e00910.
59. Jarkov V, Allan SJ, Bowen C, Khanbareh H. Piezoelectric materials and systems for tissue engineering and implantable energy harvesting devices for biomedical applications. *International Materials Reviews*. 2022 Oct 3;67(7):683–733.
60. Kikunaga K, Terasaki N. Demonstration of static electricity induced luminescence. *Sci Rep*. 2022 Jun 2;12(1):8524.
61. Petri AK, Schmiedchen K, Stunder D, Dechent D, Kraus T, Bailey WH, et al. Biological effects of exposure to static electric fields in humans and vertebrates: a systematic review. *Environmental Health*. 2017 Dec 17;16(1):41.
62. Yoo D, Jang S, Cho S, Choi D, Kim DS. A Liquid Triboelectric Series. *Advanced Materials*. 2023 Jun 25;35(26).
63. Lee J, Lee J, Baik J. The Progress of PVDF as a Functional Material for Triboelectric Nanogenerators and Self-Powered Sensors. *Micromachines (Basel)*. 2018 Oct 20;9(10):532.
64. Tofel P, Částková K, Říha D, Sobola D, Papež N, Kaštyl J, et al. Triboelectric Response of Electrospun Stratified PVDF and PA Structures. *Nanomaterials*. 2022 Jan 22;12(3):349.
65. Singh V, Rana S, Bokolia R, Panwar AK, Meena R, Singh B. Electrospun PVDF-MoSe<sub>2</sub> nanofibers based hybrid triboelectric nanogenerator for self-powered water splitting system. *J Alloys Compd*. 2024 Mar;978:173416.
66. Shee C, Banerjee S, Bairagi S, Baburaj A, Kumar S K N, Aliyana AK, et al. A critical review on polyvinylidene fluoride (PVDF)/zinc oxide (ZnO) based piezoelectric and triboelectric nanogenerators. *Journal of Physics: Energy*. 2024 Apr 18;
67. Yu Z, Chen M, Wang Y, Zheng J, Zhang Y, Zhou H, et al. Nanoporous PVDF Hollow Fiber Employed Piezo–Tribo Nanogenerator for Effective Acoustic Harvesting. *ACS Appl Mater Interfaces*. 2021 Jun 16;13(23):26981–8.

68. Kim DW, Lee JH, Kim JK, Jeong U. Material aspects of triboelectric energy generation and sensors. *NPG Asia Mater.* 2020 Dec 24;12(1):6.
69. Sabouni Tabari R, Chen Y, Thummavichai K, Zhang Y, Saadi Z, Neves AIS, et al. Piezoelectric Property of Electrospun PVDF Nanofibers as Linking Tips of Artificial-Hair-Cell Structures in Cochlea. *Nanomaterials (Basel).* 2022 Apr 26;12(9).
70. Li X, Yu W, Gao X, Liu H, Han N, Zhang X. PVDF microspheres@PLLA nanofibers-based hybrid tribo/piezoelectric nanogenerator with excellent electrical output properties. *Mater Adv.* 2021;2(18):6011–9.
71. Zhang J, Wang H, Blanloeuil P, Li G, Sha Z, Wang D, et al. Enhancing the triboelectricity of stretchable electrospun piezoelectric polyvinylidene fluoride/boron nitride nanosheets composite nanofibers. *Composites Communications.* 2020 Dec;22:100535.
72. Lin MF, Chang KW, Lee CH, Wu XX, Huang YC. Electrospun P3HT/PVDF-HFP semiconductive nanofibers for triboelectric nanogenerators. *Sci Rep.* 2022 Sep 1;12(1):14842.
73. Ju M, Dou Z, Li JW, Qiu X, Shen B, Zhang D, et al. Piezoelectric Materials and Sensors for Structural Health Monitoring: Fundamental Aspects, Current Status, and Future Perspectives. *Sensors.* 2023 Jan 3;23(1):543.
74. Zheng P, Wei W, Liang Z, Qin B, Tian J, Wang J, et al. Universal epitaxy of non-centrosymmetric two-dimensional single-crystal metal dichalcogenides. *Nat Commun.* 2023 Feb 3;14(1):592.
75. Marques CA, Neat MJ, Yim CM, Watson MD, Rhodes LC, Heil C, et al. Electronic structure and superconductivity of the non-centrosymmetric  $\text{Sn}_4\text{As}_3$ . *New J Phys.* 2020 Jun 1;22(6):063049.
76. Priya S, Song HC, Zhou Y, Varghese R, Chopra A, Kim SG, et al. A Review on Piezoelectric Energy Harvesting: Materials, Methods, and Circuits. *Energy Harvesting and Systems.* 2019 Aug 27;4(1):3–39.
77. Braun C, Mereacre L, Ehrenberg H.  $\text{PbCN}_2$  – an elucidation of its modifications and morphologies. *Zeitschrift für Naturforschung B.* 2021 Nov 25;76(10–12):857–68.
78. Chen J, Qiu Q, Han Y, Lau D. Piezoelectric materials for sustainable building structures: Fundamentals and applications. *Renewable and Sustainable Energy Reviews.* 2019 Mar;101:14–25.
79. Meng Y, Chen G, Huang M. Piezoelectric Materials: Properties, Advancements, and Design Strategies for High-Temperature Applications. *Nanomaterials (Basel).* 2022 Apr 1;12(7).
80. Zhou X, Zhou K, Zhang D, Bowen C, Wang Q, Zhong J, et al. Perspective on Porous Piezoelectric Ceramics to Control Internal Stress. *Nanoenergy Advances.* 2022 Sep 26;2(4):269–90.

81. Shaukat H, Ali A, Bibi S, Altabay WA, Noori M, Kouritem SA. A Review of the Recent Advances in Piezoelectric Materials, Energy Harvester Structures, and Their Applications in Analytical Chemistry. *Applied Sciences*. 2023 Jan 18;13(3):1300.
82. Mahapatra S Das, Mohapatra PC, Aria AI, Christie G, Mishra YK, Hofmann S, et al. Piezoelectric Materials for Energy Harvesting and Sensing Applications: Roadmap for Future Smart Materials. *Advanced Science*. 2021 Sep 13;8(17).
83. Wang Y, Hong M, Venezuela J, Liu T, Dargusch M. Expedient secondary functions of flexible piezoelectrics for biomedical energy harvesting. *Bioact Mater*. 2023 Apr;22:291–311.
84. Siddique A, Nawaz H, Razzaque S, Tabasum A, Gong H, Razzaq H, et al. PVDF-Based Piezo-Catalytic Membranes—A Net-Zero Emission Approach towards Textile Wastewater Purification. *Polymers (Basel)*. 2024 Mar 4;16(5):699.
85. Mohammadpourfazeli S, Arash S, Ansari A, Yang S, Mallick K, Bagherzadeh R. Future prospects and recent developments of polyvinylidene fluoride (PVDF) piezoelectric polymer; fabrication methods, structure, and electro-mechanical properties. *RSC Adv*. 2022 Dec 19;13(1):370–87.
86. Xie L, Wang G, Jiang C, Yu F, Zhao X. Properties and Applications of Flexible Poly(Vinylidene Fluoride)-Based Piezoelectric Materials. *Crystals (Basel)*. 2021 Jun 6;11(6):644.
87. Chan KY, Li CL, Wang DM, Lai JY. Formation of Porous Structures and Crystalline Phases in Poly(vinylidene fluoride) Membranes Prepared with Nonsolvent-Induced Phase Separation—Roles of Solvent Polarity. *Polymers (Basel)*. 2023 Mar 6;15(5):1314.
88. Jia N, He Q, Sun J, Xia G, Song R. Crystallization behavior and electroactive properties of PVDF, P(VDF-TrFE) and their blend films. *Polym Test*. 2017 Feb;57:302–6.
89. Tansel T. High beta-phase processing of polyvinylidene fluoride for pyroelectric applications. *Journal of Polymer Research*. 2020 Apr 23;27(4):95.
90. Salimi A, Yousefi AA. Analysis Method. *Polym Test*. 2003 Sep;22(6):699–704.
91. Liu ZH, Pan CT, Lin LW, Huang JC, Ou ZY. Direct-write PVDF nonwoven fiber fabric energy harvesters via the hollow cylindrical near-field electrospinning process. *Smart Mater Struct*. 2014 Feb 1;23(2):025003.
92. Pan H, Na B, Lv R, Li C, Zhu J, Yu Z. Polar phase formation in poly(vinylidene fluoride) induced by melt annealing. *J Polym Sci B Polym Phys*. 2012 Oct 15;50(20):1433–7.
93. Yu Y, Li J, Xie Z, Gong X, Gao G, Wang J, et al. Characterizing piezoelectric properties of PVDF film under extreme loadings. *Smart Mater Struct*. 2024 Jan 1;33(1):015026.

94. Wu L, Huang G, Hu N, Fu S, Qiu J, Wang Z, et al. Improvement of the piezoelectric properties of PVDF-HFP using AgNWs. *RSC Adv.* 2014;4(68):35896–903.
95. Shehata N, Nair R, Boualayan R, Kandas I, Masrani A, Elnabawy E, et al. Stretchable nanofibers of polyvinylidene fluoride (PVDF)/thermoplastic polyurethane (TPU) nanocomposite to support piezoelectric response via mechanical elasticity. *Sci Rep.* 2022 May 18;12(1):8335.
96. Ali N, Kenawy ER, Wadoud AA, Elhadary MI. Wearable Electrospun Piezoelectric Mats Based on a PVDF Nanofiber–ZnO@ZnS Core–Shell Nanoparticles Composite for Power Generation. *Nanomaterials.* 2023 Oct 26;13(21):2833.
97. He Z, Rault F, Lewandowski M, Mohsenzadeh E, Salaün F. Electrospun PVDF Nanofibers for Piezoelectric Applications: A Review of the Influence of Electrospinning Parameters on the  $\beta$  Phase and Crystallinity Enhancement. *Polymers (Basel).* 2021 Jan 6;13(2).
98. Zhang M, Liu C, Li B, Shen Y, Wang H, Ji K, et al. Electrospun PVDF-based piezoelectric nanofibers: materials, structures, and applications. *Nanoscale Adv.* 2023 Feb 14;5(4):1043–59.
99. Damdinov BB. Rheological Properties of PVDF Solutions. *Journal of Siberian Federal University Mathematics & Physics.* 2021 Jun;265–72.
100. Jones G, Assink R, Dargaville T, Chaplya P, Clough R, Elliott J, et al. Characterization, performance and optimization of PVDF as a piezoelectric film for advanced space mirror concepts. Albuquerque, NM, and Livermore, CA (United States); 2005 Nov.
101. Chakhchaoui N, Farhan R, Eddiai A, Meddad M, Cherkaoui O, Mazroui M, et al. Improvement of the electroactive  $\beta$  - phase nucleation and piezoelectric properties of PVDF-HFP thin films influenced by TiO<sub>2</sub> nanoparticles. *Mater Today Proc.* 2021;39:1148–52.
102. Oumghar K, Chakhchaoui N, Farhane R, Eddiai A, Meddad M, Cherkaoui O, et al. Enhanced piezoelectric properties of PVdF-HFP/PZT nanocomposite for energy harvesting application. *IOP Conf Ser Mater Sci Eng.* 2020 Apr 1;827(1):012034.
103. Lei D, Hu N, Wu L, Alamusi, Ning H, Wang Y, et al. Improvement of the piezoelectricity of PVDF-HFP by CoFe<sub>2</sub>O<sub>4</sub> nanoparticles. *Nano Materials Science.* 2023 Mar;
104. Lei D, Hu N, Wu L, Huang R, Lee A, Jin Z, et al. Preparation of efficient piezoelectric PVDF–HFP/Ni composite films by high electric field poling. *Nanotechnol Rev.* 2022 Jan 15;11(1):452–62.
105. Parangusan H, Ponnamma D, Al-Maadeed MAA. Stretchable Electrospun PVDF-HFP/Co-ZnO Nanofibers as Piezoelectric Nanogenerators. *Sci Rep.* 2018 Jan 15;8(1):754.

106. Liew WH, Mirshekarloo MS, Chen S, Yao K, Tay FEH. Nanoconfinement induced crystal orientation and large piezoelectric coefficient in vertically aligned P(VDF-TrFE) nanotube array. *Sci Rep*. 2015 May 12;5(1):09790.
107. Wang Z, Liu S, Yang Z, Dong S. Perspective on Development of Piezoelectric Micro-Power Generators. *Nanoenergy Advances*. 2023 Apr 4;3(2):73–100.
108. Liao Y, Yang H, Liao Q, Si W, Chu Y, Chu X, et al. A Review of Flexible Acceleration Sensors Based on Piezoelectric Materials: Performance Characterization, Parametric Analysis, Frontier Technologies, and Applications. *Coatings*. 2023 Jul 15;13(7):1252.
109. Turdakyn N, Bekezhankyzy Z, Araby S, Montazami R, Bakenov Z, Kalimuldina G. Investigation of electrospun piezoelectric P(VDF-TrFE) nanofiber-based nanogenerators for energy harvesting. *Energy Reports*. 2023 Nov;10:628–36.
110. Ou-Yang W, Weis M, Chen X, Manaka T, Iwamoto M. Study of phase transition of two-dimensional ferroelectric copolymer P(VDF-TrFE) Langmuir monolayer by Maxwell displacement current and Brewster angle microscopy. *J Chem Phys*. 2009 Sep 14;131(10).
111. P S LP, Swain B, Rajput S, Behera S, Parida S. Advances in P(VDF-TrFE) Composites: A Methodical Review on Enhanced Properties and Emerging Electronics Applications. *Condens Matter*. 2023 Dec 1;8(4):105.
112. Wu L, Jin Z, Liu Y, Ning H, Liu X, Alamusi, et al. Recent advances in the preparation of PVDF-based piezoelectric materials. *Nanotechnol Rev*. 2022 Mar 25;11(1):1386–407.
113. Najjar R, Luo Y, Jao D, Brennan D, Xue Y, Beachley V, et al. Biocompatible Silk/Polymer Energy Harvesters Using Stretched Poly (vinylidene fluoride-co-hexafluoropropylene) (PVDF-HFP) Nanofibers. *Polymers (Basel)*. 2017 Sep 30;9(12):479.
114. Kabakov P, Kim T, Cheng Z, Jiang X, Zhang S. The Versatility of Piezoelectric Composites. *Annu Rev Mater Res*. 2023 Jul 3;53(1):165–93.
115. Lee H, Zhang S, Bar-Cohen Y, Sherrit S. High Temperature, High Power Piezoelectric Composite Transducers. *Sensors*. 2014 Aug 8;14(8):14526–52.
116. Acosta M, Novak N, Rojas V, Patel S, Vaish R, Koruza J, et al. BaTiO<sub>3</sub>-based piezoelectrics: Fundamentals, current status, and perspectives. *Appl Phys Rev*. 2017 Dec 1;4(4).
117. Sundar U, Lao Z, Cook-Chennault K. Investigation of Piezoelectricity and Resistivity of Surface Modified Barium Titanate Nanocomposites. *Polymers (Basel)*. 2019 Dec 17;11(12):2123.
118. Mahboubizadeh S, Dilamani ST, Baghshahi S. Piezoelectricity performance and  $\beta$ -phase analysis of PVDF composite fibers with BaTiO<sub>3</sub> and PZT reinforcement. *Heliyon*. 2024 Feb 15;10(3):e25021.

119. Sobolev K, Kolesnikova V, Omelyanchik A, Alekhina Y, Antipova V, Makarova L, et al. Effect of Piezoelectric BaTiO<sub>3</sub> Filler on Mechanical and Magnetoelectric Properties of Zn<sub>0.25</sub>Co<sub>0.75</sub>Fe<sub>2</sub>O<sub>4</sub>/PVDF-TrFE Composites. *Polymers (Basel)*. 2022 Nov 8;14(22).
120. Brusa E, Carrera A, Delprete C. A Review of Piezoelectric Energy Harvesting: Materials, Design, and Readout Circuits. *Actuators*. 2023 Dec 8;12(12):457.
121. Safaei M, Sodano HA, Anton SR. A review of energy harvesting using piezoelectric materials: state-of-the-art a decade later (2008–2018). *Smart Mater Struct*. 2019 Nov 1;28(11):113001.
122. Li H, Tian C, Deng ZD. Energy harvesting from low frequency applications using piezoelectric materials. *Appl Phys Rev*. 2014 Dec;1(4):041301.
123. Zhou C, Bag S, Lv B, Thangadurai V. Understanding the Role of Solvents on the Morphological Structure and Li-Ion Conductivity of Poly(vinylidene fluoride)-Based Polymer Electrolytes. *J Electrochem Soc*. 2020 Jan 5;167(7):070552.
124. Terziyan T V., Safronov AP. Solubility and H-bonding of poly(vinylidene fluoride) copolymers in carbonyl liquids: Experiment and molecular simulation. *J Mol Liq*. 2019 Feb;275:378–83.
125. Filip P, Zelenkova J, Peer P. Electrospinning of a Copolymer PVDF-co-HFP Solved in DMF/Acetone: Explicit Relations among Viscosity, Polymer Concentration, DMF/Acetone Ratio and Mean Nanofiber Diameter. *Polymers (Basel)*. 2021 Oct 5;13(19):3418.
126. Chen F, Zhao Y, Zhou Y, Xu J, Yang Y, Yang W. Effect of solvent on the energy storage property of poly(vinylidene fluoride-hexafluoropropylene). *Mater Res Express*. 2020 Jan 1;7(1):015323.
127. Marshall JE, Zhenova A, Roberts S, Petchey T, Zhu P, Dancer CEJ, et al. On the Solubility and Stability of Polyvinylidene Fluoride. *Polymers (Basel)*. 2021 Apr 21;13(9):1354.
128. Costa CM, Cardoso VF, Martins P, Correia DM, Gonçalves R, Costa P, et al. Smart and Multifunctional Materials Based on Electroactive Poly(vinylidene fluoride): Recent Advances and Opportunities in Sensors, Actuators, Energy, Environmental, and Biomedical Applications. *Chem Rev*. 2023 Oct 11;123(19):11392–487.
129. Payo I, Hale JM. Dynamic characterization of piezoelectric paint sensors under biaxial strain. *Sens Actuators A Phys*. 2010 Sep;163(1):150–8.
130. Yang C, Fritzen CP. Piezoelectric paint: characterization for further applications. *Smart Mater Struct*. 2012 Apr 1;21(4):045017.
131. Brennan DA, Jao D, Siracusa MC, Wilkinson AR, Hu X, Beachley VZ. Concurrent collection and post-drawing of individual electrospun polymer nanofibers to enhance macromolecular alignment and mechanical properties. *Polymer (Guildf)*. 2016 Oct;103:243–50.

132. Abdulhussain R, Adebisi A, Conway BR, Asare-Addo K. Electrospun nanofibers: Exploring process parameters, polymer selection, and recent applications in pharmaceuticals and drug delivery. *J Drug Deliv Sci Technol.* 2023 Dec;90:105156.
133. Conte AA, Shirvani K, Hones H, Wildgoose A, Ye X, Najjar R, et al. Effects of post-draw processing on the structure and functional properties of electrospun PVDF-HFP nanofibers. *Polymer (Guildf).* 2019 May 8;171:192–200.
134. Park S, Kwon Y, Sung M, Lee BS, Bae J, Yu WR. Poling-free spinning process of manufacturing piezoelectric yarns for textile applications. *Mater Des.* 2019 Oct;179:107889.
135. Fernández-Diego C, Fernández I, Ortiz F, Carrascal I, Renedo C, Delgado F. Assessment of Dielectric Paper Degradation through Mechanical Characterisation. In: *Simulation and Modelling of Electrical Insulation Weaknesses in Electrical Equipment.* InTech; 2018.
136. Babashakoori S, Ezoji M. Average fiber diameter measurement in Scanning Electron Microscopy images based on Gabor filtering and Hough transform. *Measurement.* 2019 Jul;141:364–70.
137. Abdelkader M, Mazari A, Zafar S. Experimental Techniques to Obtain the Cross-Sectional Images of Textile Yarns. *Materials (Basel).* 2022 Jul 6;15(14).
138. Choi S, Kwon M, Park MJ, Kim J. Analysis of Microplastics Released from Plain Woven Classified by Yarn Types during Washing and Drying. *Polymers (Basel).* 2021 Sep 3;13(17):2988.
139. Su Y, Li W, Cheng X, Zhou Y, Yang S, Zhang X, et al. High-performance piezoelectric composites via  $\beta$  phase programming. *Nat Commun.* 2022 Aug 18;13(1):4867.
140. Srinivasaraghavan Govindarajan R, Ren Z, Melendez I, Boetcher SKS, Madiyar F, Kim D. Polymer Nanocomposite Sensors with Improved Piezoelectric Properties through Additive Manufacturing. *Sensors (Basel).* 2024 Apr 24;24(9).
141. Ali U, Zhou Y, Wang X, Lin T. Direct electrospinning of highly twisted, continuous nanofiber yarns. *Journal of the Textile Institute.* 2012 Jan;103(1):80–8.
142. Ma X, Liu J, Ni C, Martin DC, Chase DB, Rabolt JF. Molecular Orientation in Electrospun Poly(vinylidene fluoride) Fibers. *ACS Macro Lett.* 2012 Mar 20;1(3):428–31.
143. Lei T, Yu L, Zheng G, Wang L, Wu D, Sun D. Electrospinning-induced preferred dipole orientation in PVDF fibers. *J Mater Sci.* 2015 Jun 9;50(12):4342–7.
144. Kobayashi M, Tashiro K, Tadokoro H. Molecular Vibrations of Three Crystal Forms of Poly(vinylidene fluoride). *Macromolecules.* 1975 Mar 1;8(2):158–71.
145. Cai X, Lei T, Sun D, Lin L. A critical analysis of the  $\alpha$ ,  $\beta$  and  $\gamma$  phases in poly(vinylidene fluoride) using FTIR. *RSC Adv.* 2017;7(25):15382–9.

146. Wolff S, Jirasek F, Beuermann S, Türk M. Crystal phase transformation of  $\alpha$  into  $\beta$  phase poly(vinylidene fluoride) via particle formation caused by rapid expansion of supercritical solutions. *RSC Adv.* 2015;5(82):66644–9.
147. Brennan DA, Shirvani K, Rhoads CD, Lofland SE, Beachley VZ. Electrospinning and post-drawn processing effects on the molecular organization and mechanical properties of polyacrylonitrile (PAN) nanofibers. *MRS Commun.* 2019 Jun 20;9(2):764–72.
148. Azari A, Golchin A, Mahmoodinia Maymand M, Mansouri F, Ardeshirylajimi A. Electrospun Polycaprolactone Nanofibers: Current Research and Applications in Biomedical Application. *Adv Pharm Bull.* 2022 Aug;12(4):658–72.
149. Bachmann MA, Koenig JL. Vibrational analysis of phase III of poly (vinylidene fluoride). *J Chem Phys.* 1981 May 15;74(10):5896–910.
150. Ma X, Liu J, Ni C, Martin DC, Bruce Chase D, Rabolt JF. The effect of collector gap width on the extent of molecular orientation in polymer nanofibers. *J Polym Sci B Polym Phys.* 2016 Mar 15;54(6):617–23.
151. Zhi C, Shi S, Si Y, Fei B, Huang H, Hu J. Recent Progress of Wearable Piezoelectric Pressure Sensors Based on Nanofibers, Yarns, and Their Fabrics via Electrospinning. *Adv Mater Technol.* 2023 Mar 30;8(5).
152. He J, Zhou Y, Qi K, Wang L, Li P, Cui S. Continuous twisted nanofiber yarns fabricated by double conjugate electrospinning. *Fibers and Polymers.* 2013 Nov 6;14(11):1857–63.

## **Appendix**

### **List of Abbreviations**

LD – low density

MD – medium density

HD – high density

DR – draw ratio

LDR - low-density draw ratio

MDR - medium-density draw ratio

HDR – high-density draw ratio